

ELASTIC STRATIGRAPHIC INVERSION, AN INTEGRATED APPROACH

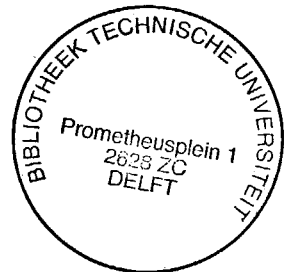
PROEFSCHRIFT

ter verkrijging van de graad van doctor
aan de Technische Universiteit Delft,
op gezag van de Rector Magnificus,
prof. drs. P.A. Schenck,
in het openbaar te verdedigen
ten overstaan van een commissie,
aangewezen door het College van Dekanen
op dinsdag 18 februari 1992 te 16.00 uur door

JOHAN CORNELIS DE HAAS

geboren te Leeuwarden

natuurkundig ingenieur



Gebotekst Zoetermeer / 1992

Dit proefschrift is goedgekeurd door de promotor:

prof. dr. ir. A.J. Berkhout

Copyright ©1992, by Delft University of Technology, Delft, The Netherlands.

All rights reserved. No part of this publication may be reproduced, stored in a retrieval system or transmitted in any forms or by any means, electronic, mechanical, photocopying, recording or otherwise, without the prior written permission of the author J.C. de Haas, Delft University of Technology, Faculty of Applied Physics, P.O. Box 5046, 2600 GA Delft, The Netherlands.

CIP-DATA KONINKLIJKE BIBLIOTHEEK, DEN HAAG

Haas, Johan Cornelis de

Elastic stratigraphic inversion, an integrated approach /

Johan Cornelis de Haas. – [S.l. : s.n.]. – Ill.

Proefschrift Technische Universiteit Delft. – Met lit. opg.

ISBN 90-9004416-7

Trefw.: seismologie

Printed in The Netherlands by: N.K.B. Offset bv, Bleiswijk

To Marisela

Preface

Within the Laboratory of Seismics and Acoustics, the PRINCEPS consortium project for detailed poststack inversion was successfully completed at the end of 1985. I joined prof. Berkhout's group in the beginning of 1986 as one of the members of the PRINCEPS II continuation project, which focussed on elastic prestack inversion and lithologic inversion. After the integration with the structural TRITON project, the work was continued within the newly formed DELPHI project. From that moment, my research activities have benefitted from the well defined DELPHI research plan as well as the greater interaction with the DELPHI colleagues.

Within the PRINCEPS II project, I enjoyed many fruitful and not-so-fruitful discussions with colleagues Alex Geerling and Gerd-Jan Lörtzer. The many post-midnight report gluing sessions proved that working late can be fun and will not easily be forgotten.

For my work within the DELPHI project, I relied many times on three of my colleagues: Greg Haimé was always there when I needed finite difference data. The help of Eric Verschuur—master of the already infamous EV utilities—with many processing tasks was greatly appreciated. Finally, the p - τ tandem with Cees de Bruin provided me with the required input data for my inversion scheme. The examples that are discussed in this thesis could not have been realized without their cooperation.

Besides them I will kindly remember the other DELPHI colleagues Philippe Herrmann, Henk Cox, Berend Scheffers and Walter Rietveld, who always reminded me to stay "on top of the target".

As it turned out, computing became one of my greater passions and I came up with more plans and ideas than ten wise programmers could implement. Only thanks to the aid of the B-team, Jan-Willem de Bruijn, Edo Bergsma, Leen Buitelaar and Henry den Bok, many of the projects were indeed successfully completed.

Special thanks are due to Kees Wapenaar who was simply always there to provide answers to urgent theoretical questions. I would also like to thank Jacob Fokkema who introduced me to the topic of elastic modeling in the p - τ domain. Besides that, both gentlemen never failed to show me that also post-convention geophysics can be a lot of fun.

Many thanks go to my *promotor* prof. Berkhout for being such an excellent supervisor. His ideas and enthusiasm were always a source of inspiration and only sometimes a little extra work.

Finally, sincere thanks are due to my girl friend Marisela whose threats have indeed resulted in the completion of this thesis before our wedding.

Table of Contents

| | |
|--|-----------|
| 1 Introduction | 1 |
| 1.1 Seismic amplitudes | 1 |
| 1.2 Seismic inversion | 2 |
| 1.2.1 Inversion by data fitting | 3 |
| 1.2.2 Direct inversion | 4 |
| 1.2.3 Parametrization | 4 |
| 1.3 AVO feature extraction | 5 |
| 1.4 Nonlinear prestack inversion | 8 |
| 1.4.1 Gridded inversion with the adjoint-state technique | 8 |
| 1.4.2 Acoustic gridded inversion | 9 |
| 1.4.3 Elastic gridded inversion | 9 |
| 2 Target oriented inversion: the DELPHI approach | 11 |
| 2.1 The DELPHI scheme for elastic processing and inversion | 11 |
| 2.2 Concept of a locally 1D target | 14 |
| 3 Scattering of plane waves at a horizontal boundary | 17 |
| 3.1 P- and S-waves | 17 |
| 3.2 The wavenumber-frequency and plane-wave domains | 18 |
| 3.3 Elastic wave equations | 20 |
| 3.3.1 Definition of the Lamé potentials for P- and S-waves | 20 |
| 3.3.2 Downgoing and upgoing P- and S-waves | 22 |
| 3.3.3 Propagating and evanescent plane waves | 23 |
| 3.4 Definition of the scattering matrix | 25 |
| 3.5 Derivation of the scattering matrix | 26 |
| 3.5.1 Composition and decomposition matrices for elastic wave fields | 27 |
| 3.5.2 Boundary conditions | 29 |
| 3.6 Some properties of the scattering coefficients | 30 |

| | |
|---|-----------|
| 3.6.1 Dependence on the elastic parameters..... | 30 |
| 3.6.2 Approximation formulas | 31 |
| 3.6.3 Examples..... | 34 |
| 4 Forward modeling in the horizontal slowness - frequency domain | 39 |
| 4.1 Introduction..... | 39 |
| 4.2 The reflectivity method..... | 39 |
| 4.2.1 Introduction | 39 |
| 4.2.2 The propagator method | 41 |
| 4.3 Recursive reflectivity algorithm | 43 |
| 4.3.1 Theory..... | 43 |
| 4.3.2 An interpretation in terms of rays | 45 |
| 4.3.3 Implementation aspects..... | 46 |
| 4.4 Behavior at a horizontal slowness equal to the slowness of a layer | 47 |
| 4.5 Example | 49 |
| 5 Bayesian Inversion..... | 53 |
| 5.1 Probability theory..... | 53 |
| 5.1.1 Cumulative distribution and probability density functions | 53 |
| 5.1.2 Mean and Covariance | 54 |
| 5.1.3 Bayes' rule..... | 55 |
| 5.2 Bayes' rule and inversion | 55 |
| 5.2.1 Estimators..... | 57 |
| 5.2.2 Gaussian statistics for noise and prior information | 57 |
| 5.2.3 Result analysis | 59 |
| 5.3 Nonlinear optimization..... | 60 |
| 5.3.1 General methods | 60 |
| 5.3.2 Methods for the minimization of a sum of squares | 61 |
| 5.3.3 Application to the elastic inverse problem | 62 |
| 6 Elastic stratigraphic Inversion | 65 |
| 6.1 Introduction..... | 65 |
| 6.1.1 Elastic parametrization..... | 66 |
| 6.1.2 Wavelet and initial model | 66 |
| 6.2 Non-uniqueness aspects of the elastic inverse problem..... | 68 |
| 6.2.1 An analysis using the approximated reflectivity functions..... | 68 |
| 6.2.2 Angle vs. ray parameter..... | 70 |
| 6.2.3 Small offsets | 70 |
| 6.2.4 Contour plots | 71 |

| | |
|--|------------|
| 6.3 Prior information for elastic stratigraphic inversion | 73 |
| 6.3.1 Targetzone averages of the elastic parameters | 74 |
| 6.3.2 Empirical relations | 74 |
| 6.4 Robustness parameters | 76 |
| 6.4.1 Traveltime errors | 76 |
| 6.4.2 Amplitude errors | 78 |
| 6.4.3 Non-uniqueness aspects | 79 |
| 6.5 Litho-elastic inversion | 79 |
| 6.5.1 Basic strategy | 80 |
| 6.5.2 Elastic parameters as a function of the porosity | 82 |
| 6.5.3 Time average equation | 84 |
| 7 Examples | 87 |
| 7.1 Elastic inversion for a 1D target under a 2D overburden. | 88 |
| 7.1.1 Elastic model | 88 |
| 7.1.2 Modeling and pre-processing | 88 |
| 7.1.3 Data at the target level | 92 |
| 7.1.4 Robustness, Initial and Prior models | 95 |
| 7.1.5 Results | 96 |
| 7.1.6 Conclusions | 100 |
| 7.2 Inversion for a laterally varying targetzone | 101 |
| 7.2.1 Modeling and processing | 102 |
| 7.2.2 Inversion considerations | 103 |
| 7.2.3 Inversion results for PP data only | 105 |
| 7.2.4 Inversion results for a combination of PP and SS data | 110 |
| 7.2.5 Conclusions | 110 |
| 7.3 Litho-elastic inversion example | 111 |
| 7.3.1 Modeling | 113 |
| 7.3.2 Processing | 114 |
| 7.3.3 Inversion considerations | 116 |
| 7.3.4 Inversion results for PP data only | 120 |
| 7.3.5 Inversion results for a combination of PP and SP data | 120 |
| 7.3.6 Conclusions | 120 |
| 8 Conclusions and discussion | 121 |
| 8.1 Elastic prior information | 122 |
| 8.2 Lithologic prior information | 123 |
| 8.3 Discussion and recommendations | 123 |

| | |
|---|------------|
| Appendix A Scattering in terms of particle displacements and Lamé potentials | 127 |
| <i>A1 Particle motion for homogeneous and inhomogeneous waves</i> | <i>127</i> |
| <i>A2 Potentials and particle-displacements</i> | <i>129</i> |
| Appendix B Explicit expressions for the scattering coefficients | 133 |
| References | 135 |
| Summary | 141 |
| Samenvatting | 143 |
| Curriculum Vitae | 145 |

1.1 Seismic amplitudes

For the longest part of the seismic exploration history, amplitudes have played a minor role in the processing and interpretation of seismic measurements. It was not until the 1970's that interpreters started to associate high amplitudes on stacked sections, so-called bright spots, with the presence of gas. This caused many oil companies to have a new look at their data.

However, many of the drilled bright spots appeared to be due to other anomalies than the desired presence of hydrocarbons. Then, a decade later, the next hidden treasure was discovered: the amplitudes in the *prestack* data. It appeared that the amplitude *variation* with offset of the gas related bright spots was much larger than those of the non-gas related events. The classical papers of Ostrander, Ostrander (1982, 1984), were the first ones to describe the anomalous amplitude versus offset (AVO) behavior of the frequently encountered case of a gas sand embedded in shale. The AVO behavior of this particular sequence has been the basis of many AVO (inversion) techniques and, therefore, deserves a description in this introduction.

Fig. 1-1a, adopted from Ostrander (1984) shows an elastic model consisting of a gas sand embedded in shale. The values of the elastic parameters (P-wave velocity α , density ρ and Poisson's ratio σ) are typical for an unconsolidated, young geologic section. The gas fill of the sand causes a strong decrease of the P-wave velocity, while the S-wave velocity remains practically unaffected, leading to an anomalously low Poisson's ratio. Fig. 1-1a shows the plane-wave reflection coefficients of the top and base of the gas sand as a function of the incident angle θ_1 . Observe that the absolute value of the reflectivity increases considerably with incident angle for both reflecting interfaces. If the gas sand would be replaced by a brine-filled rock with an equally low P-wave velocity, but the same Poisson's ratio as that of the surrounding shale, the reflectivity would remain approximately constant, as shown by the striped lines in Fig. 1-1b.

For the AVO analysis at some specific locations for a specific target, it may suffice to do some forward modeling experiments in order to match the observed prestack amplitudes. However, when one is interested in, say, the lateral extent of a reservoir, such a "manual" procedure would be too laborious. In such a case, automated methods, that relate the prestack amplitudes to the elastic parameters and, ultimately to the lithology are to be preferred. One can distinguish between AVO feature extraction methods and more sophisticated inversion methods, see Fig. 1-2. The first type of methods often accomplish no more than pre-selecting heterogeneities in the subsurface that, under certain assumptions, can be related to hydrocarbon accumulations: The feature is used as an indicator. Inversion methods yield an elastic image of the subsurface that would enable a *quantitative* lithologic analysis. Before discussing the merits of both methods (in Sections 1.3 and 1.4), the inversion formalism will be discussed.

1.2 Seismic inversion

Seismic inversion is the process of inferring information about the subsurface from seismic measurements. In this thesis, *elastic* inversion will be discussed, meaning the retrieval of the *elastic* properties of the subsurface. The term inversion is some-

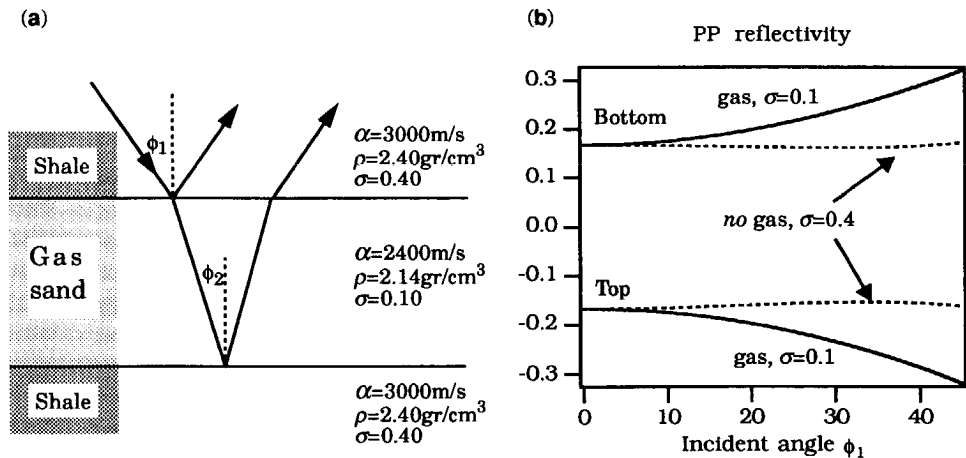


Fig. 1-1 (a) Some typical values for the elastic parameters of a gas sand embedded in shale in a young sedimentary setting, where α , ρ and σ respectively denote P-wave velocity, density and Poisson's ratio. (b) The angle dependent reflection functions of the top and bottom of the gas sand show a strong increasing amplitude with increasing angle. The dotted lines show the practically constant reflectivity when the gas sand is replaced by a brine-filled rock with the same P-wave velocity and density but a Poisson's ratio that is equal to that of the surrounding shale (0.40).

what ambiguous because it is used for two quite different methodologies. Let me introduce the mathematical formalism of the so-called forward model:

$$\mathbf{d} = \mathbf{g}(\mathbf{x}) + \mathbf{n} \quad (1-1)$$

where \mathbf{d} is the vector that contains the seismic measurements, \mathbf{x} is the vector that contains all the subsurface parameters and \mathbf{g} is the set of relations that constitute the forward model. The additive noise is represented by the vector \mathbf{n} .

1.2.1 Inversion by data fitting

The most common type of inversion can be described as data fitting. This means that one seeks a set of parameters that minimizes some norm of the difference between the observed data and the predicted data. In general, the l_2 norm of the data mismatch \mathbf{e} is minimized, leading to the following objective function:

$$F(\mathbf{x}) = |\mathbf{d} - \mathbf{g}(\mathbf{x})|^2 = |\mathbf{e}|^2 \quad (1-2)$$

Often, extra mismatch terms and varying weights of the different terms are used in the objective function, see Section 5.2.2, but this is not relevant for the present discussion. The solution to the inverse problem is defined as the set of parameters $\hat{\mathbf{x}}$ for which $F(\hat{\mathbf{x}})$ is the global minimum of the function F .

In the general case of a nonlinear forward model, the objective function is minimized by iteratively updating an initial guess \mathbf{x}_0 of the model parameters. In each iteration, at least one forward modeling is needed to obtain the current residuals:

$$\mathbf{e}_n = \mathbf{d} - \mathbf{g}(\mathbf{x}_n), \quad (1-3)$$

where the subscript n denotes the n^{th} iteration. A general formulation for the update formula that describes the iterative parameter updates is, see Section 5.3:

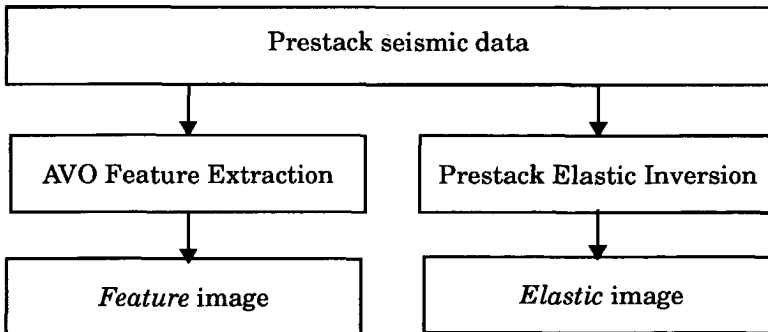


Fig. 1-2 The amplitude information in the prestack data can be analyzed through AVO feature extraction or through—more sophisticated—inversion methods.

$$\mathbf{x}_{n+1} = \mathbf{x}_n + \alpha_n \mathbf{H}_n \mathbf{J}_n^t \mathbf{e}_n, \quad (1-4)$$

where α_n is the "step length", \mathbf{H}_n is a positive definite "conditioning" matrix and \mathbf{J}_n is the Jacobian matrix of first order derivatives of \mathbf{e}_n . The last two terms are the gradient of the objective function: $\text{grad } F = \mathbf{J}_n^t \mathbf{e}_n$. The different optimization methods differ with respect to the choice for the step length α_n and, most importantly, the matrix \mathbf{H}_n .

For a linear forward model, $\mathbf{d} = \mathbf{A}\mathbf{x}$, the well known Gauss-Newton equation yields an analytical solution for the parameters:

$$\hat{\mathbf{x}} = (\mathbf{A}^t \mathbf{A})^{-1} \mathbf{A}^t \mathbf{d} \quad (1-5)$$

In this thesis, inversion by means of data fitting will be used to estimate elastic subsurface models.

1.2.2 Direct Inversion

For the other, less frequently used type of inversion, a series of mathematical transformations—often involving various approximations—is used to manipulate the forward relation (1-1) into an inverse relation:

$$\hat{\mathbf{x}} = \mathbf{g}^{-1}(\mathbf{d}) \quad (1-6)$$

In seismology, the term inverse scattering is generally used to denote the direct inversion methods. The inverse scattering approach basically consists of applying a sequence of mathematical operators that convert the observed data into a model. These operators are derived from the conventional forward scattering theory. Layer stripping methods for 1D media belong to this general class of inverse scattering methods. This "direct inversion" can only be accomplished for relatively simple forward models, e.g. the 1D acoustic situation. Note that the data fit concept does not play a role here, which can lead to a surprisingly poor match between observed data and the synthetic data of the estimated model.

Sofar, the discussion has been limited to inversion for an image of the subsurface. In a broader context, inversion includes many model based processing algorithms, e.g. deconvolution and redatuming, since here too, a forward relation is inverted. The result of such an inversion is a new dataset. Direct inversion is well suited for such processing algorithms, because wave propagation is a linear process. The subsurface parameters, however, determine the seismic response in a nonlinear fashion, which makes the data-fitting inversion approach more feasible for the determination of subsurface models.

1.2.3 Parametrization

A second distinction that can be made, concerns the representation of the subsurface in the vector \mathbf{x} . A very straightforward way of representation consists of sam-

pling the subsurface properties on a regular grid. In this *gridded* inversion, no assumptions are made about the structure of the subsurface, which can be considered a pro. On the negative side, the number of parameters (the length of \mathbf{x}) is typically very large and the solution will be bandlimited.

Its counterpart is parametric inversion which means that the subsurface is parametrized with a number of distinct layers. The layer boundaries are then assumed to be parametric functions (e.g. splines) of the lateral position. The elastic properties within a layer can either be constant or parametric functions of the lateral position and, sometimes, depth. A simpler layered parametrization is shown in Fig. 1-3 where the model is gridded in the lateral direction. In the vertical direction, the model consists of homogeneous layers. In Section 2.2, it will be argued that an inversion per lateral position is attractive and feasible for well-behaved subsurface geometries. Assuming that the elastic quantities of interest are e.g. the P-wave velocity α , S-wave velocity β and density ρ , the parameter vector at position $j\Delta h$ will be:

$$\mathbf{x} = (\alpha_1, \dots, \alpha_4, \beta_1, \dots, \beta_4, \rho_1, \dots, \rho_4, \Delta z_1, \dots, \Delta z_3)^t. \quad (1-7)$$

Now that the principles of inversion are outlined, the discussion of the AVO and prestack inversion methods continues.

1.3 AVO feature extraction

Feature extraction methods generally assume NMO corrected CMP data as input. Usually, the data are processed to correct for source/receiver directivity and ampli-

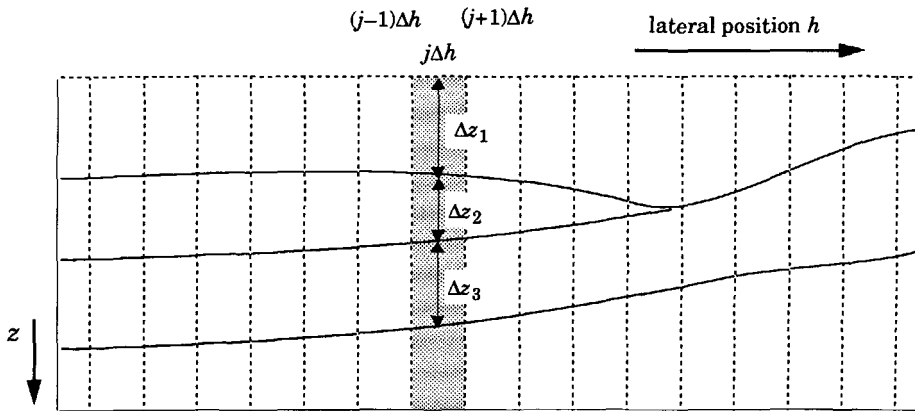


Fig. 1-3 Subsurface model with a gridded representation in the lateral direction. A cross-section of the elastic properties in the vertical direction is assumed to be a piecewise constant function.

tude loss due to the divergence of the wavefield. Often some extra processing—e.g. surface consistent amplitude corrections and inverse-Q filtering—is done to insure that the observed amplitudes pertain to the local lithology and not to effects of propagation and data acquisition, see e.g. Yu (1985) and Mazzotti (1991).

Most feature extraction methods are based on a weighted stacking procedure, a term that was introduced by Smith and Gidlow (1987). The weighted stack derives its name from the fact that every sample of its output trace—corresponding to a certain two-way traveltime—is a weighted sum of the samples in the NMO corrected CMP gather, at the same traveltime. By comparison, for the normal stack, all the weights would be equal to unity. The used weighting function depends on the incident angle. The latter one is a function of traveltime and offset and is usually obtained by ray tracing in a macro velocity model.

The weighted stacking methods are based on approximations of the angle dependent reflectivity functions that are linear in the relative parameter contrasts, see Section 3.6.2. In its simplest form, the plane-wave reflection coefficient for *P*-waves can be approximated with:

$$r(\theta) = a + b \sin^2 \theta \quad (1-8)$$

where θ is the incident angle. Often, a higher order approximation with an extra $\sin^4 \theta$ term is used, see e.g. Smith and Gidlow (1987) and Shuey (1985). Other authors, e.g. Balogh et al. (1986), Ursin and Dahl (1990), have introduced the offset (instead of the incident angle) as the independent variable in the reflection coefficient approximation.

For the above approximation, the weighted stacking procedure actually fits relation (1-8) to every line of samples of constant two-way traveltime in the CMP gather and yields a normal incidence *a* trace and a gradient *b* trace. Since the forward model (1-8) is linear in the parameters *a* and *b*, this fitting can be done by applying the Gauss-Newton relation (1-5). So, the weighted stack can be considered a data fitting inversion method with a linear forward model and a gridded (in terms of traveltime) subsurface representation.

By itself, the normal incidence and the gradient trace can already serve as useful features. But they can be combined in order to highlight the typical gas sand AVO behavior pictured in Fig. 1-1. According to Treadgold et al. (1990a,b), the product of the *a* and *b* traces is commonly used as an indicator of hydrocarbons. Clearly, this product trace has a strong positive response when the normal incidence and gradient trace are strong and have the same polarity, as is the case for the top and base reflectors of Fig. 1-1. Reflectors without AVO variations (*b*=0) simply disappear on the *a***b* section.

Smith and Gidlow (1987) opted for a procedure that is based on empirical relations between the elastic parameters to highlight the presence of hydrocarbons: Using the Gardner relation between P-wave velocity and density and the Mudrock relation of Castagna et al. (1985) between P- and S-wave velocity, they derive a weighted stack for their so-called fluid factor, that highlights deviations with respect to the aforementioned empirical relations; these deviations are assumed to be due to gas fill.

Weighted stacking has two main advantages over more sophisticated nonlinear inversion methods:

- 1) The computational cost is small so that complete 2D and even 3D sections, see Vail et al. (1990), can routinely be processed.
- 2) There are no numerical problems like slow convergence and local minima that often occur with nonlinear inversion.

On the other hand, weighted stacking is based on quite restrictive assumptions:

- 1) The subsurface model is assumed to be approximately 1D, so that the incident angles and the geometrical divergence factor can be easily calculated as a function of the offset and the two-way traveltime. Furthermore, the 1D assumption is needed to insure that the CMP data is related to one lateral position (no reflection point smear).
- 2) The NMO correction has to be *very* accurate. It has been shown, see Spratt (1987), that the gradient and higher order traces are very sensitive to residual NMO errors. Interfering reflections with a different AVO behavior will cause a phase change with offset of the observed waveform. This will appear as a residual NMO effect but should *not* be corrected for. So there is a fundamental problem with judging the accuracy of the NMO correction.
- 3) Moderate angles (pre-critical) and moderate parameter contrasts.

Even if the above conditions are satisfied, there is a problem with the interpretation of the results. Gas sands do not always exhibit the strong AVO behavior as pictured in Fig. 1-1, see Rutherford and Williams (1990). On the other hand, a strong AVO behavior need not always be due to the presence of gas, see Ball (1987). From a physical point of view, this is perfectly understandable: The angle dependent reflectivity of an interface between two elastic media depends solely on the elastic parameters of *both* media and many parameter combinations will cause a strong AVO behavior.

So, a possible strategy would be to estimate the elastic parameters from the observed amplitudes and use them, in a second step, to infer the lithology. This is indeed the approach that is followed in the DELPHI project of our group, see Chapter 2. There is little chance though, to obtain independent estimates of all three elastic parameters from weighted stacking: Swan (1990) demonstrated that, using angles up to 30° , the noise on the P-wave velocity ($\Delta\alpha/\alpha$) and density ($\Delta\rho/\rho$) traces is 5 to 50 times higher than the noise on the prestack data! Some authors, e.g. Lörtzer and Berkhout (1990) use stabilization to obtain less noisy results. A drawback of weighted stacking remains, however, that it is based on a linear formulation that is valid for small offsets, whereas the large offsets actually contain the information that is needed to resolve all parameters independently.

1.4 Nonlinear prestack inversion

Contrary to the conventional AVO methods described in the previous section, nonlinear inversion of prestack data is still in the research stage. As already mentioned in Section 1.2, it is sensible to make a distinction between direct inversion methods and data fitting inversion methods. In this introduction on prestack inversion, only inversion by means of data fitting will be discussed.

1.4.1 Gridded inversion with the adjoint-state technique

Most of the published least squares inversion methods for prestack data are gridded ones. In all the gridded inversion methods, the same clever method is used to calculate the gradient of the objective function. A brute force calculation, by perturbing the gridded model parameters one by one and using a finite difference approximation to obtain the derivatives, would lead to an insurmountable computational burden, since it requires N forward modeling steps, where N is the—typically huge—number of parameters.

This clever method is the so-called adjoint-state technique, which requires only two forward modeling steps to calculate the gradient. Some authors use the terms adjoint equation or adjoint Green's function to denote this technique. It is a general mathematical tool that can be applied to optimization problems related to the solution of (partial) differential equations. McGillivray and Oldenburg (1990) give a general overview of techniques to calculate the Jacobian matrix \mathbf{J} for a discrete parameter space and its equivalent, the Fréchet derivatives, for the continuous case and give many references of applications in a variety of disciplines. The adjoint-state method is one of those techniques and, as they describe on pp. 511-512, it can be modified to solely calculate the gradient $\mathbf{J}^t \mathbf{e}$ of a least-squares objective function using only two forward modeling steps.

The introduction of this technique to the seismic inverse problem is due to Bamberger, Chavent, Hemon and Lailly (1982), where it was applied to normal-incidence

dence acoustic impedance inversion. The prestack 1D acoustic problem was first addressed by Lailly (1983). He demonstrated that the gradient follows from the correlation of the forward propagating source wavefield and the reverse-time propagating data residuals. This process resembles conventional prestack migration.

A lucid treatment of the adjoint-state technique applied to the general (multi-shot, 2D or 3D) prestack acoustic case can be found in Tarantola (1984a). The elastic case was subsequently solved by Tarantola (1984b). Mora (1987) gives a less formal but better comprehensible treatment of the elastic case. Also for the general acoustic/elastic case, the gradient is found by a correlation of the forward propagating source wavefield and the reverse-time propagating data residuals.

1.4.2 Acoustic gridded inversion

The actual *application* of prestack least squares inversion using the adjoint state gradient calculation started with the computationally least demanding case of the 1D acoustic problem. Kolb, Collino and Lailly (1986) inverted a synthetic shot record in the h - t (offset - travelttime) domain for the velocity, assuming a known density. Kolb and Canadas (1986) extended that experiment to invert for both velocity and density. Helgesen (1991) augmented the 1D method to account for source and receiver arrays.

Since the number of parameters for the 1D problem is relatively small (500-5000), it is computationally feasible to use a Quasi-Newton optimization scheme where the matrix \mathbf{H} in (1-4) approximates the inverse Hessian, see Section 5.3.2. In the above mentioned papers a Quasi-Newton scheme is used indeed.

Some authors have applied the adjoint-state technique in the p - τ (ray parameter – intercept time) domain. For acoustic wave propagation in a 1D medium, every trace of constant p can be described by a separate one-dimensional wave equation and an impedance function $Z(p, \tau)$. In Chapel, Kolb and Canadas (1989) and Kolb, Chapel and Picart (1989), this property is used to estimate the primary reflectivity as a function of p . Pan et al. (1988, 1989) apply the adjoint-state technique in the p - τ domain to invert for the density and the velocity.

1.4.3 Elastic gridded inversion

Judged by the number of publications, there is nowadays more research in elastic inversion than in acoustic inversion. The present emphasis on elastic inversion is fully justified in the authors opinion: The properties of the subsurface—at least at depths that are of interest to petroleum exploration—are obviously more *elastic* than *acoustic*. Furthermore, the angle dependent reflectivity of an elastic contrast is generally quite different from that of the corresponding acoustic contrast, see Section 3.6.2. This means that acoustic methods are not suitable for analyzing the prestack amplitude information in a quantitative manner.

Another trend is the increasing popularity of 2D elastic inversion over 1D inversion. Subsurface structures that are of interest to petroleum exploration are often *not* approximately one-dimensional. 2D (and ultimately 3D) inversion methods therefore hold a much greater promise to become valuable exploration tools than their 1D counterparts.

The present bloom of 2D gridded elastic inversion based on data fitting is mainly due to Albert Tarantola of the Paris based Institute de Physique du Globe. Together with co-workers, more than twenty-five papers have been published on this subject; a convenient bibliography can be found in Tarantola et al. (1990).

In the majority of the papers, the conventional least squares criterion is minimized to estimate the gridded subsurface parameters. Since a 2D slice of the subsurface is inverted for, the data vector will contain a number of shot gathers *at the surface*. Since the number of parameters N is also very large (typically, $N > 10^5$), full $N \times N$ matrices which are needed for Newton type optimization methods are far too big to fit even on the largest computer systems. This is why conjugate gradient algorithms, for which the matrix \mathbf{H} in (1-4) is diagonal, are generally used for the 2D inversion problem. The required gradient is calculated with the aforementioned adjoint-state technique.

The idea of using all available seismic data simultaneously in one big inversion scheme is conceptually simple. It is also an attractive idea, because the information that is present in multiples, surface waves and converted waves, is not discarded but actually used in the inversion. However, there is one major problem with such large-scale inversion methods (the term large-scale being used as opposite to target-oriented): They are generally unable to retrieve the low-wavenumber velocity model (the trend). This low-wavenumber information is present in the traveltimes of the reflections. But since the forward model is strongly nonlinear with respect to the velocity trend, the gradient-based optimization technique will usually not converge to the true model.

2.1 The DELPHI scheme for elastic processing and inversion.

Within the Laboratory of Seismics and Acoustics, the seismic inverse problem is solved in a hierarchical manner. In the Delft Philosophy on Elastic Inversion (DELPHI), see Berkhout and Wapenaar (1990), three mechanisms determine the seismic response: Surface interaction, propagation and reflection. Rather than inverting the total seismic response with a single algorithm, each of the three parts of the seismic response is processed or inverted by optimally chosen algorithms.

After the first phase of exploration, one is interested in the detail of specific parts of the subsurface, e.g. a potential reservoir. It is therefore sufficient to invert only for the detail of such a target zone instead of inverting for the detail of the whole subsurface. Target oriented inversion is one of the key strategies that underlie the DELPHI scheme, pictured in Fig. 2-1, which consists of the following 6 modules:

- 1a) Wave field decomposition of the multicomponent shot gathers into shot gathers that correspond to pure P- or S-wave sources and receivers, see Wapenaar et al. (1990). For the 2D case this means that the input gathers $u_x \tau_{xz}$, $u_z \tau_{xz}$, $u_x \tau_{zz}$ and $u_z \tau_{zz}$ are decomposed into PP, SP, PS and SS gathers, where the first symbol denotes the receiver type and the second symbol denotes the source type:
 - τ_{xz} , τ_{zz} : shear, tensile stress on a horizontal surface,
 - u_x , u_z : horizontal, vertical particle velocity,
 - P: P-wave potential,
 - S: SV-wave potential.
- 1b) Surface related multiple elimination. Since the free surface is a very strong reflector, the surface related multiples can completely mask the primary reflections from deeper interfaces. The elimination procedure consists of an adaptive direct inversion process, see Verschuur (1991). It uses the pre-

stack data itself in the multiple prediction operator and therefore requires no knowledge about the subsurface.

- 2a) **Macro model estimation.** The propagation through the subsurface is mainly determined by the macro velocity models (both for P- and S-waves). The macro models are estimated with a focussing and/or imaging analysis, see Cox (1991).
- 2b) **True amplitude, prestack redatuming of the PP, PS, SP and SS shot gathers,** using the estimated macro models, see de Bruin et al. (1990). In this procedure, the propagation effects are removed from the data by direct inversion, and data acquisition just above the targetzone can be simulated.

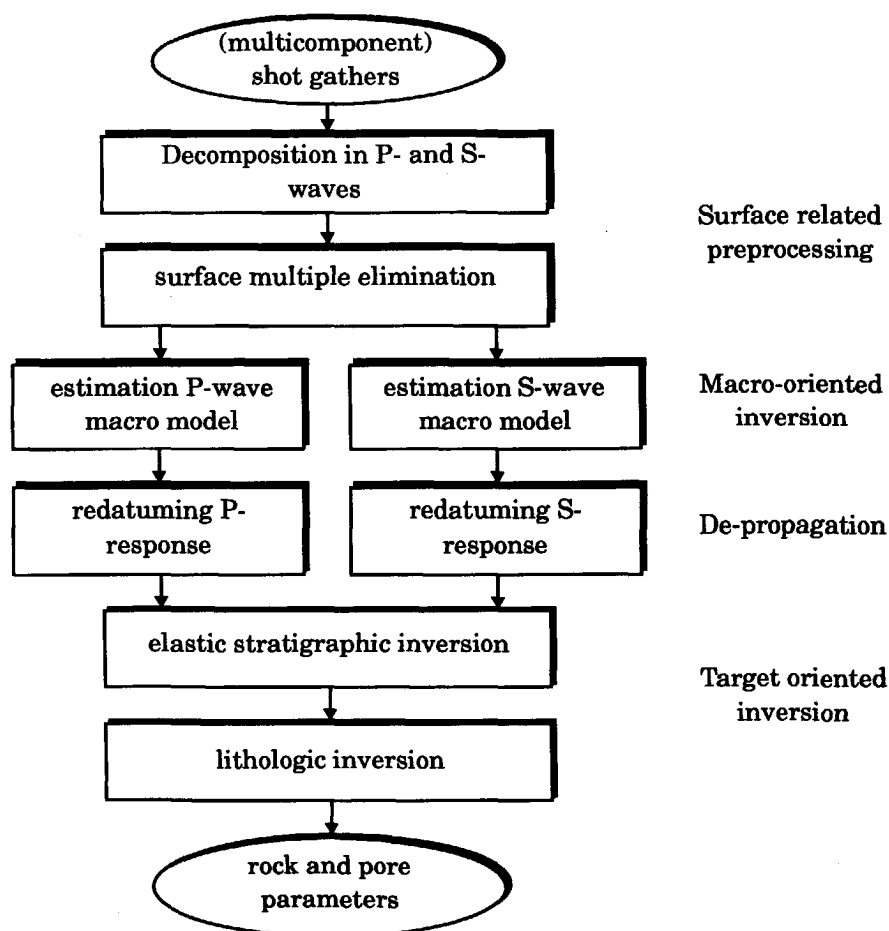


Fig. 2-1 The hierarchical DELPHI scheme for elastic processing and inversion.

- 3a) Elastic inversion of the redatumed gathers. This is the module that is discussed in this thesis.
- 3b) Lithologic inversion of the previously estimated elastic parameters for the rock and pore parameters, see Lörtzer (1990), Lörtzer and Berkhout (1992).

Modules 1a) and 1b) are the surface related preprocessing steps. The parameters of importance are the source and receiver characteristics and the near surface properties. It is important to note that *no* information about the subsurface is needed. Modules 2a) and 2b) deal with the propagation properties (traveltime and amplitude) of the overburden. These are mainly determined by the macro properties of the subsurface. Ultimately, modules 3a) and 3b) aim at retrieving the detailed elastic and lithologic properties of the targetzone.

The multiple elimination (1b) and redatuming (2b) steps are based on linear wave propagation, so that a direct inversion approach is appropriate. The macro model estimation (2a) and elastic and lithologic inversion (3a,b) are based on nonlinear forward models which calls for a data fitting inversion approach.

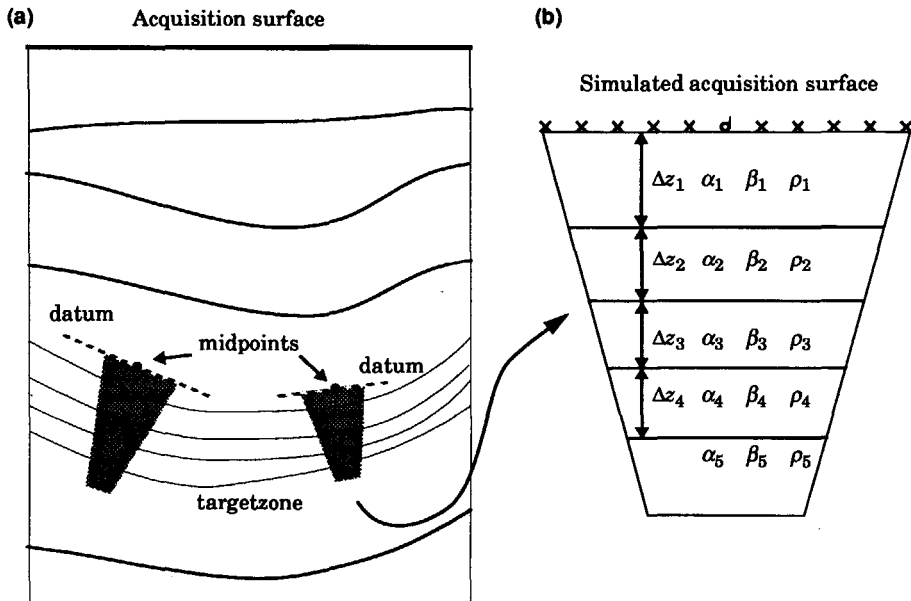


Fig. 2-2 (a) Two-dimensional subsurface model with target zone. The dotted lines indicate the redatuming levels. (b) At the redatuming level, (the simulated acquisition surface) the targetzone looks like a 1D model.

2.2 Concept of a locally 1D target

Consider the 2D subsurface model pictured in Fig. 2-2a. Treating the surface data with 1D processing and inversion algorithms would certainly lead to erroneous results. It will be argued now, that, given appropriate preprocessing, it is still possible to make use of a 1D elastic inversion algorithm for the targetzone. To that end, the redatuming level, see step 2a) of the DELPHI scheme, is chosen just above and parallel to the local layering of the targetzone as pictured in Fig. 2-2a. Subsequently, the redatumed data are reordered into CMP gathers. These two steps guarantee that the reflection point smear is small for the targetzone reflectors. In other words, the information in the CMP's is related to *one* lateral position. At the redatuming level, the CMP's are transformed to the p - τ domain. As will be argued in Section 4.1, it is computationally advantageous to perform the inversion in the p - τ domain. Note that each reflectivity type (PP, PS, SP or SS) is independently redatumed to yield one CMP gather of the same type at the new datum.

Assuming small conflicting dips within the targetzone, the targetzone can *locally* be parametrized by a 1D elastic model, see Fig. 2-2b. This allows the use of a 1D inversion algorithm for the data at a certain lateral position along the target. In the redatuming stage, one specifies the positions where the local p - τ data are to be generated. Subsequently, the elastic inversion is carried out at these locations. Any combination of the four different reflectivity types can be used (e.g. PP only, PP and SS or all four). Finally, the individual solutions must be integrated to form a consistent 2D (or 3D) targetzone model, see Fig. 2-3.

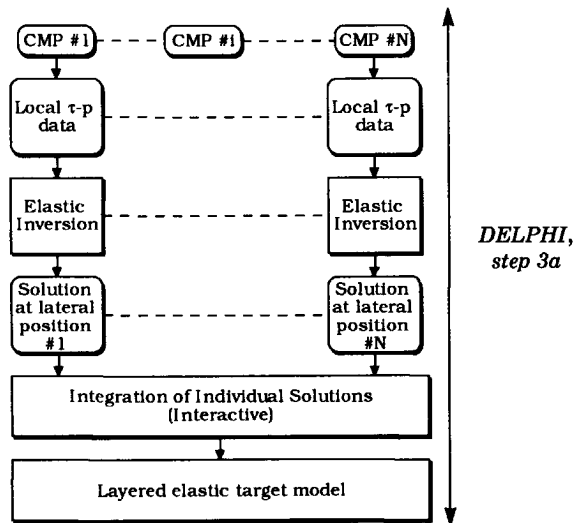


Fig. 2-3 Integration of the solutions at individual midpoints to form a 2D or 3D targetzone model.

The choice of inverting for a layered elastic model is an important one. An advantage over gridded inversion is that layers with a thickness smaller than the dominant seismic wavelength can be resolved. A second advantage is the smaller number of parameters, which generally leads to a better determined inverse problem. A third and major advantage is that the—geology based—parametrization in terms of layers allows for the specification of geology based prior information.

Although the proposed parametrization in terms of locally 1D layered models should be quite adequate for many situations that are encountered in practice, there are some exceptions:

- In structurally complex areas, e.g. with many faults, the 1D assumption will not hold.
- If it appears from logs that the elastic parameters show strong vertical gradients within a layer or that important layers are just not homogeneous enough, the parametrization in terms of homogeneous layers is not accurate.

Scattering of plane waves at a horizontal boundary

In this chapter, the scattering of plane waves at a horizontal boundary between two homogeneous isotropic elastic media will be discussed, the term scattering denoting both reflection and transmission. The reflection and transmission coefficients that will be derived, are used in the forward modeling scheme that is discussed in Chapter 4. Approximation formulas, that give an insight in the dependence of the angle dependent reflectivity on the medium parameters are discussed at the end of the chapter.

3.1 P- and S-waves

In this section, the scattering matrix (i.e. the matrix that contains the reflection and transmission coefficients) for a horizontal interface between two homogeneous isotropic elastic media will be introduced. Besides compressional waves (P-waves), elastic media support the propagation of shear waves (S-waves). The terms P- and S- do not originate from pressure and shear but rather from global seismology because the P(rietary) waves propagate faster and are earlier recorded than the S(econdary) waves. Apart from the evanescent part of the wave field, P-waves are longitudinal waves, meaning that the direction of particle motion coincides with the direction of wave propagation. Under the same restriction, S-waves are transverse waves, meaning that the direction of particle displacement is perpendicular to the direction of wave propagation. These properties are only valid in homogeneous isotropic elastic media. For a more extensive discussion, the reader is referred to Section 3.3.3.

For two-dimensional media (i.e. the medium is invariant in the y -direction), one can distinguish between two types of S-waves, depending on their polarization:

- SH-waves are horizontally polarized, the particle motion is in the horizontal (x - y) plane.

- SV-waves are vertically polarized, the particle motion is in the plane that is defined by the vertical and the direction of wave propagation.

In this thesis, only line sources (in the y direction) over 1D or 2D media will be considered, see Fig. 3-1. Consequently, the elastic wave fields will also be invariant in the y direction. In that case, the propagation of SH-waves is an independent problem (no wave conversions), that can be described by a single, scalar wave equation. Although reflections of SH-waves certainly exhibit angle dependence, a choice has been made for this research to consider only P- and SV-waves.

3.2 The wavenumber-frequency and plane-wave domains

Before continuing the discussion of the scattering of elastic waves, the definitions of the various domains that play a role in this thesis will be introduced. Since the discussion in this thesis is limited to elastic media and wave fields that bear no y -dependence, the spatially varying functions have only x - and z -dependence. The notation convention for the various domains that play a role in this thesis is summarized in Table 3-1. Any function in the space-time domain (x, z, t) will be denoted by a lowercase symbol. The corresponding function in the space - frequency domain (x, z, ω) will be denoted by the corresponding uppercase symbol. The corresponding function in the wavenumber - frequency (k_x, z, ω) domain will be denoted by the corresponding uppercase symbol with a tilde (\sim). To denote functions that depend on the horizontal slowness p , another typeface is used, see Table 3-1. Functions in the horizontal slowness - intercept time domain (p, z, τ) are denoted with a lower-

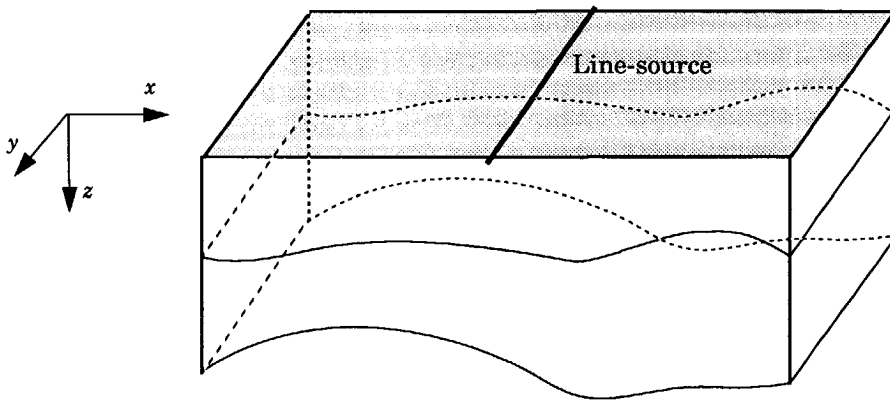


Fig. 3-1 Line-source over an elastic medium of which the properties do not vary in the y -direction.

case symbol. The corresponding function in the horizontal slowness - frequency domain (p, z, ω) is denoted by the corresponding uppercase symbol.

The temporal Fourier transform of a space- and time dependent function is defined by:

$$A(x, z, \omega) = \int_{-\infty}^{\infty} a(x, z, t) e^{-i\omega t} dt. \quad (3-1)$$

Considering only real functions $a(x, z, t)$, it suffices to consider only positive frequencies in the inverse temporal Fourier transform

$$a(x, z, t) = \frac{1}{\pi} \operatorname{Re} \left[\int_0^{+\infty} A(x, z, \omega) e^{i\omega t} d\omega \right]. \quad (3-2)$$

It is convenient to define the spatial Fourier transform with the opposite sign in the exponent as compared to the temporal Fourier transform

$$\tilde{A}(k_x, z, \omega) = \int_{-\infty}^{\infty} A(x, z, \omega) e^{+ik_x x} dx. \quad (3-3)$$

Its inverse is

$$A(x, z, \omega) = \frac{1}{2\pi} \int_{-\infty}^{\infty} \tilde{A}(k_x, z, \omega) e^{-ik_x x} dk_x. \quad (3-4)$$

Table 3-1 Notation convention for the different domains that play a role in this thesis. The quantities in the x - t , x - ω and k_x - ω domains are represented through the serif typefaces 'New Century Schoolbook' and 'Symbol'. The quantities in the p - τ and p - ω domains are represented through the sans-serif typefaces 'Helvetica' and 'New Greek Helvetica'.

| DOMAIN | SCALAR | VECTOR | MATRIX |
|--------------------|--|--|--|
| (x, z, t) | a, f, ϕ, ψ | $\mathbf{a}, \mathbf{f}, \boldsymbol{\phi}, \boldsymbol{\psi}$ | not used |
| (x, z, ω) | A, F, Φ, Ψ | $\mathbf{A}, \mathbf{F}, \boldsymbol{\Phi}, \boldsymbol{\Psi}$ | not used |
| (k_x, z, ω) | $\tilde{A}, \tilde{F}, \tilde{\Phi}, \tilde{\Psi}$ | $\tilde{\mathbf{A}}, \tilde{\mathbf{F}}, \tilde{\boldsymbol{\Phi}}, \tilde{\boldsymbol{\Psi}}$ | $\tilde{\mathbf{A}}, \tilde{\mathbf{F}}, \tilde{\boldsymbol{\Phi}}, \tilde{\boldsymbol{\Psi}}$ |
| (p, z, τ) | a, f, ϕ, ψ | $\mathbf{a}, \mathbf{f}, \boldsymbol{\phi}, \boldsymbol{\psi}$ | not used |
| (p, z, ω) | A, F, Φ, Ψ | $\mathbf{A}, \mathbf{F}, \boldsymbol{\Phi}, \boldsymbol{\Psi}$ | $\mathbf{A}, \mathbf{F}, \boldsymbol{\Phi}, \boldsymbol{\Psi}$ |

This sign convention causes a plane-wave with positive k_x to propagate in the positive x -direction. Besides the wavenumber - frequency domain, the horizontal slowness - frequency (p, z, ω) domain is convenient for the derivation of the scattering matrix. The horizontal wavenumber k_x is related to the horizontal slowness p through

$$k_x = \omega p. \quad (3-5)$$

A function in the (p, z, ω) domain can simply be derived from the corresponding function in the (k_x, z, ω) domain by substituting (3-5) for k_x :

$$A(p, z, \omega) = \tilde{A}(\omega p, z, \omega). \quad (3-6)$$

Applying an inverse Fourier transform to $A(p, z, \omega)$ over ω yields the corresponding function in the horizontal slowness - intercept time (p, z, τ) domain:

$$a(p, z, \tau) = \frac{1}{\pi} \operatorname{Re} \left[\int_0^{+\infty} A(p, z, \omega) e^{i\omega\tau} d\omega \right]. \quad (3-7)$$

It is interesting to note that $a(p, z, \tau)$ can also be obtained by the well-known slant-stack procedure. From (3-3) and (3-6) it follows:

$$A(p, z, \omega) = \int_{-\infty}^{+\infty} A(x, z, \omega) e^{i\omega p x} dx. \quad (3-8)$$

Applying an inverse temporal Fourier transform to both sides and making use of the shift property, yields the slant-stack expression:

$$a(p, z, \tau) = \int_{-\infty}^{+\infty} a(x, z, \tau + px) dx. \quad (3-9)$$

Note that the depth dependence is explicitly expressed in the above definitions. Often, one wants to describe registrations on a certain horizontal acquisition surface. For convenience, the z -dependence is then omitted from the notation.

3.3 Elastic wave equations

3.3.1 Definition of the Lamé potentials for P- and S-waves

The various reflection and transmission coefficients are most easily defined in terms of the so-called Lamé potentials for P- and S-waves. Following appendix B of Wapenaar et al. (1990), the elastic wave equation for the particle velocity in a homogeneous elastic medium reads in the space - frequency domain:

$$(\lambda + 2\mu) \nabla(\nabla \cdot \mathbf{V}) - \mu \nabla \times \nabla \times \mathbf{V} + \rho \omega^2 \mathbf{V} = \mathbf{0}, \quad (3-10)$$

where λ and μ are the Lamé coefficients.

In order to arrive at separate wave equations for P- and S-waves, the velocity is defined in terms of the Lamé potentials Φ and Ψ (Ψ is a 3x1 column vector):

$$\mathbf{V} = -\frac{1}{i\omega\rho}(\nabla\Phi + \nabla \times \Psi). \quad (3-11)$$

The factor $-(i\omega\rho)^{-1}$ is different with respect to the usual definition. It is used here, because it makes Φ equal to the acoustic pressure in the limiting case of $\mu \rightarrow 0$, i.e. an acoustic medium. Substitution of (3-11) in (3-10) yields:

$$\nabla\{(\lambda + 2\mu)\nabla^2\Phi + \rho\omega^2\Phi\} + \nabla \times \{-\mu\nabla \times \nabla \times \Psi + \rho\omega^2\Psi\} = \mathbf{0}. \quad (3-12)$$

Since the velocity has three components and Φ and Ψ together have four components, equations (3-11) do not uniquely define the Lamé potentials. In order to do so, the convenient choice is made that both terms within braces in (3-12) are zero:

$$(\lambda + 2\mu)\nabla^2\Phi + \rho\omega^2\Phi = 0, \quad (3-13a)$$

$$-\mu\nabla \times \nabla \times \Psi + \rho\omega^2\Psi = \mathbf{0}. \quad (3-13b)$$

Applying the divergence operator to (3-13b) and making use of the general relation $\nabla \cdot (\nabla \times \mathbf{f}) = 0$, yields

$$\nabla \cdot \Psi = 0, \quad (3-14)$$

which is the result of the particular choice that was made before. Relation (3-13b) can be simplified by making use of the general property

$$-\nabla \times \nabla \times \mathbf{f} + \nabla(\nabla \cdot \mathbf{f}) = \nabla^2 \mathbf{f}. \quad (3-15)$$

Because $\nabla \cdot \Psi = 0$, it follows that $\nabla \times \nabla \times \Psi = -\nabla^2 \Psi$, so that (3-13b) transforms into:

$$\mu\nabla^2\Psi + \rho\omega^2\Psi = \mathbf{0}. \quad (3-16)$$

The definitions of the P-wave velocity α and S-wave velocity β are given by:

$$\begin{aligned} \alpha &= \sqrt{(\lambda + 2\mu)/\rho}, \\ \beta &= \sqrt{\mu/\rho}. \end{aligned} \quad (3-17)$$

With (3-17), equations (3-13a) and (3-16) can be rewritten in the familiar form of the independent wave equations for P- and S-waves in homogeneous, isotropic media:

$$\begin{aligned}\nabla^2 \Phi + \frac{\omega^2 \Phi}{\alpha^2} &= 0, \\ \nabla^2 \Psi + \frac{\omega^2 \Psi}{\beta^2} &= 0,\end{aligned}\tag{3-18}$$

As was mentioned before, the elastic models and wave fields that are considered in this thesis are invariant in the y direction. Because only P- and SV-waves are considered, there is no particle motion in the y direction. Because $\nabla \times (\nabla \Phi) = 0$ (this is a general property), applying the rotation operator to (3-11) yields:

$$\nabla \times \mathbf{V} = -\frac{1}{i\omega\rho} \nabla \times \nabla \times \Psi.\tag{3-19}$$

Together with (3-13b), the following simple relation results:

$$\nabla \times \mathbf{V} = \frac{i\omega}{\mu} \Psi.\tag{3-20}$$

Expanding the rotation of the velocity field yields:

$$\Psi = \begin{pmatrix} \Psi_x \\ \Psi_y \\ \Psi_z \end{pmatrix} = \frac{\mu}{i\omega} \begin{pmatrix} \frac{\partial V_z}{\partial y} - \frac{\partial V_y}{\partial z} \\ \frac{\partial V_x}{\partial z} - \frac{\partial V_z}{\partial x} \\ \frac{\partial V_y}{\partial x} - \frac{\partial V_x}{\partial y} \end{pmatrix}.\tag{3-21}$$

Since V_y and all derivatives with respect to y are zero, it follows that $\Psi_x = \Psi_z = 0$ and that Ψ_y completely describes the SV-waves. For convenience, the subscript y will be dropped and the scalar $\Psi (= \Psi_y)$ will denote the SV-wave potential. In the remainder of this thesis, the term S-wave will be used to indicate an S-wave with SV polarization.

3.3.2 Downgoing and upgoing P- and S-waves

Using the definition (3-4) of the inverse spatial Fourier transform and relation (3-5) between k_x and p , it follows that the transform pair for the x -derivative of a function is given by:

$$\frac{\partial}{\partial x} A(x, z, \omega) \leftrightarrow -i\omega p A(p, z, \omega).\tag{3-22}$$

Using (3-22), (3-18) reads in the horizontal slowness - frequency domain (p, z, ω) :

$$\begin{aligned}\frac{\partial^2 \Phi}{\partial z^2} - \omega^2 p^2 \Phi + \omega^2 \Phi / \alpha^2 &= 0, \\ \frac{\partial^2 \Psi}{\partial z^2} - \omega^2 p^2 \Psi + \omega^2 \Psi / \beta^2 &= 0.\end{aligned}\quad (3-23)$$

Similar as above, the scalar $\Psi = \psi$, is defined as the only non-zero element of the S-wave (vector) potential Ψ :

$$\Psi = (0, \psi, 0)^t. \quad (3-24)$$

The general solution is comprised of downgoing and upgoing P- and S-waves:

$$\begin{aligned}\Phi &= \Phi^+ + \Phi^-, \\ \Psi &= \Psi^+ + \Psi^-, \end{aligned}\quad (3-25)$$

where a superscript '+' indicates that the wave is traveling downward in the positive z -direction. Likewise, a superscript '-' indicates that a wave is traveling upward in the negative z -direction. The downgoing and upgoing waves that satisfy (3-23) are defined by:

$$\begin{aligned}\Phi^\pm(p, z, \omega) &= A_\Phi^\pm \exp\{\mp i\omega q_p z\}, \\ \Psi^\pm(p, z, \omega) &= A_\Psi^\pm \exp\{\mp i\omega q_s z\},\end{aligned}\quad (3-26)$$

where the factors A are arbitrary complex constants and q_p and q_s are the vertical slownesses of P- and S-waves respectively, which obey:

$$\begin{aligned}p^2 + q_p^2 &= 1/\alpha^2, \\ p^2 + q_s^2 &= 1/\beta^2.\end{aligned}\quad (3-27)$$

3.3.3 Propagating and evanescent plane waves

One can distinguish between propagating and evanescent plane waves. Propagating waves have a horizontal phase velocity p^{-1} that is larger than or equal to the corresponding propagation velocity (α or β). They are also called homogeneous plane waves, because the amplitude is constant over a wavefront, the latter one being defined as a surface of constant phase. In accordance with (3-26), the horizontal slownesses of propagating waves are defined as real, *positive* quantities:

$$\begin{aligned}q_p &= \sqrt{1/\alpha^2 - p^2} \text{ for } p^2 \leq 1/\alpha^2, \\ q_s &= \sqrt{1/\beta^2 - p^2} \text{ for } p^2 \leq 1/\beta^2.\end{aligned}\quad (3-28)$$

Evanescent or inhomogeneous waves have a horizontal phase velocity p^{-1} that is smaller than the corresponding propagation velocity. For these waves, the vertical slownesses are defined as *negative* imaginary quantities:

$$\begin{aligned} q_p &= -i\sqrt{p^2 - 1/\alpha^2} \text{ for } p^2 > 1/\alpha^2, \\ q_s &= -i\sqrt{p^2 - 1/\beta^2} \text{ for } p^2 > 1/\beta^2. \end{aligned} \quad (3-29)$$

Substituting (3-29) in (3-26), it follows that the amplitude of a “downgoing” evanescent wave decreases exponentially with increasing depth. This is only true for positive frequencies, but then, only positive frequencies are considered in the definition of the inverse temporal Fourier transform (3-2). Likewise, the amplitudes of an “upgoing” evanescent wave decrease exponentially with decreasing depth. Note that evanescent waves cannot exist in an unbounded source-free homogeneous elastic medium because of the exponential depth dependence.

The terms “downgoing” and “upgoing” are somewhat inappropriate for evanescent waves, because their wavefronts propagate horizontally. The amplitude over a wavefront is not constant (exponential depth dependence), hence the term inhomogeneous waves. As will be shown in Appendix A, an evanescent P-wave is *not* a pure longitudinal wave because its particle motion has a nonzero z -component. Likewise, an evanescent S-wave is *not* a pure transverse wave, because its particle motion has a nonzero x -component.

For an extensive discussion of propagating and evanescent waves, the reader is referred to Wapenaar and Berkhout (1989), Section 1.4.2.

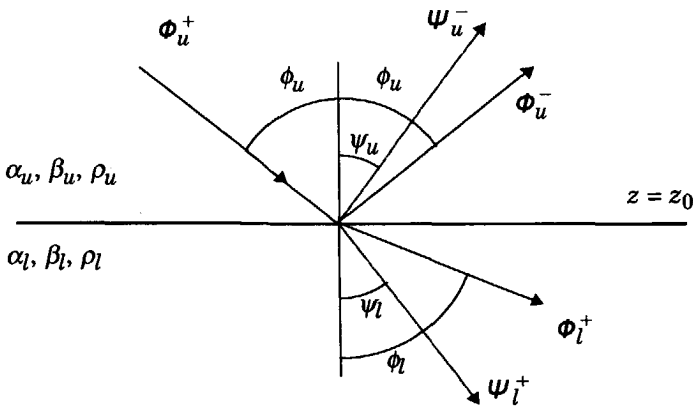


Fig. 3-2 An incident P-wave in the upper half-space causes reflected (Φ_u^- , Ψ_u^-) and transmitted (Φ_l^+ , Ψ_l^+) waves. The subscripts u and l denote upper and lower half-spaces.

3.4 Definition of the scattering matrix

Consider an interface between two elastic half-spaces, as pictured in Fig. 3-2. An incident P-wave (Φ_u^+) will cause reflected and transmitted P- and S-waves. The reflection and transmission coefficients are defined in terms of the potentials:

$$\left. \begin{aligned} \Phi_u^-(p, z_0, \omega) &= R_{11}^+(p) \Phi_u^+(p, z_0, \omega) \\ \Psi_u^-(p, z_0, \omega) &= R_{21}^+(p) \Phi_u^+(p, z_0, \omega) \end{aligned} \right\} \text{Reflection} \quad (3-30)$$

$$\left. \begin{aligned} \Phi_l^+(p, z_0, \omega) &= T_{11}^+(p) \Phi_u^+(p, z_0, \omega) \\ \Psi_l^+(p, z_0, \omega) &= T_{21}^+(p) \Phi_u^+(p, z_0, \omega) \end{aligned} \right\} \text{Transmission}$$

The incident and scattered waves are defined at z_0 , the depth of the interface. The subscripts u and l indicate whether the particular wave propagates respectively in the upper or lower half-space. As will be shown in Section 3.5, the scattering coefficients are independent of frequency. All waves in Fig. 3-2 obey Snell's law, i.e. they all have the same horizontal slowness p , also called the *ray parameter*:

$$p = \frac{\sin \phi_u}{\alpha_u} = \frac{\sin \phi_l}{\alpha_l} = \frac{\sin \psi_u}{\beta_u} = \frac{\sin \psi_l}{\beta_l}. \quad (3-31)$$

The reflection and transmission coefficients are actually elements of reflection and transmission *matrices*. The general case of scattering of plane waves at an inter-

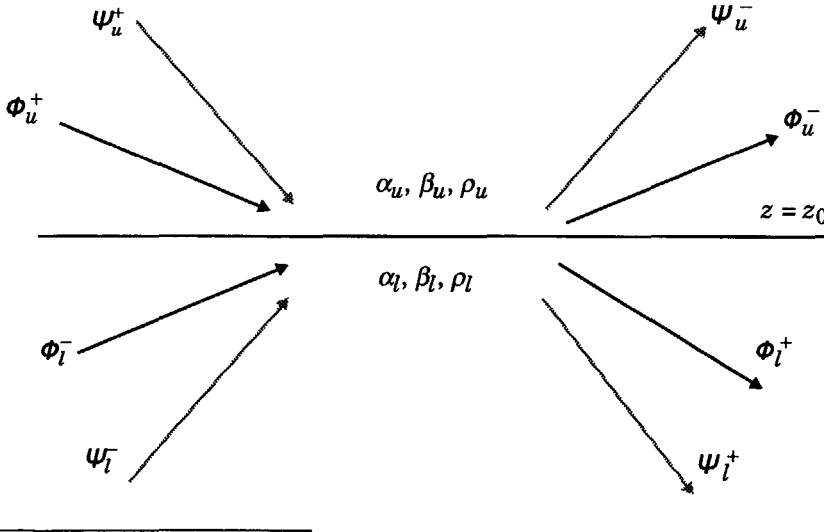


Fig. 3-3 The general case of scattering of plane waves at a horizontal interface between two elastic media. At the left are the four incident waves; at the right are the four scattered waves.

face between two elastic half-spaces is pictured in Fig. 3-3. Incident P- and S-waves exist in both half-spaces.

It is convenient to group the downgoing and upgoing waves in 2×1 vectors \mathbf{D}^+ and \mathbf{D}^- respectively:

$$\mathbf{D}^\pm = \begin{pmatrix} \phi^\pm \\ \psi^\pm \end{pmatrix}. \quad (3-32)$$

The 4×4 scattering matrix is then defined by:

$$\begin{pmatrix} \mathbf{D}_u^-(p, z_0, \omega) \\ \mathbf{D}_l^+(p, z_0, \omega) \end{pmatrix} = \underbrace{\begin{pmatrix} \mathbf{R}^+(p) & \mathbf{T}^-(p) \\ \mathbf{T}^+(p) & \mathbf{R}^-(p) \end{pmatrix}}_{\text{Scattering matrix}} \begin{pmatrix} \mathbf{D}_u^+(p, z_0, \omega) \\ \mathbf{D}_l^-(p, z_0, \omega) \end{pmatrix}. \quad (3-33)$$

As pictured in Fig. 3-3, the 2×2 submatrices \mathbf{R}^+ and \mathbf{T}^+ describe respectively reflection and transmission of a downgoing wave field in the upper half-space. The same is true for 2×2 submatrices \mathbf{R}^- and \mathbf{T}^- , but now for an upgoing incident wave field in the lower half-space. If there is only an incident P-wave in the upper half-space, ϕ_u^+ is the only nonzero element of the incident-wave vector, and the system of equations (3-33) reduces to (3-30).

3.5 Derivation of the scattering matrix

The scattering matrix for the P-SV problem of a plane interface between two homogeneous isotropic elastic media follows from the boundary conditions at the interface, which state that the particle velocity and the traction be continuous. In this section, the relations between the total elastic wave field (in terms of particle veloc-

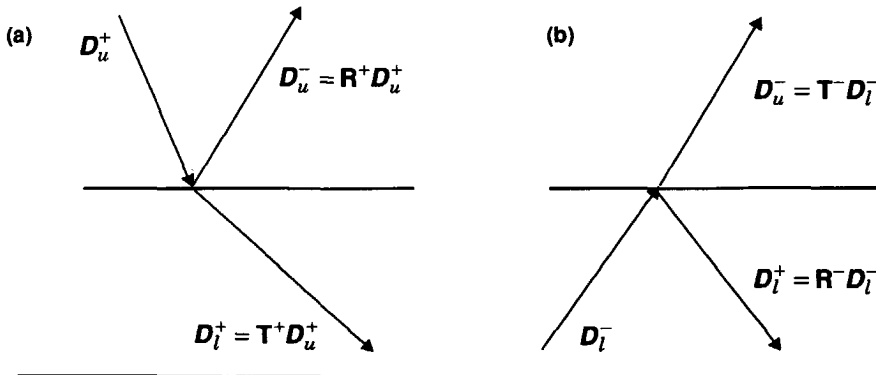


Fig. 3-4 Definition of the submatrices of the scattering matrix. (a) Scattering of an incident wave field (P and S) in the upper half-space. (b) Scattering of an incident wave field (P and S) in the lower half-space.

ity and traction) and the one-way wave fields (in terms of the Lamé potentials) will be derived. From these relations, an expression for the 4×4 scattering matrix can be derived.

3.5.1 Composition and decomposition matrices for elastic wave fields

The derivation of the composition and decomposition matrices that is given here, is largely based on Appendix B of Wapenaar et al. (1990) and Chapter IV of Wapenaar and Berkhout (1989). One difference is that here only particle motion in the x - z plane is considered (i.e. the P-SV problem). A second difference is that Wapenaar's expressions are in the k_x - ω domain, whereas the ones here are in the horizontal slowness - frequency domain. This has the advantage that the frequency drops out of the relations for the (de)composition matrices.

Since only the P-SV problem is considered, there is no wave motion in the y -direction. Neither do the wave fields vary as a function of y . So, the velocity v and the traction τ both have two components:

$$v(x, z, t) = \begin{pmatrix} v_x(x, z, t) \\ v_z(x, z, t) \end{pmatrix}, \quad (3-34a)$$

$$\tau(x, z, t) = \begin{pmatrix} \tau_{xz}(x, z, t) \\ \tau_{zz}(x, z, t) \end{pmatrix}. \quad (3-34b)$$

With definition (3-34a) and transform pair (3-22), it follows that relation (3-11) which relates the particle velocity to the Lamé potentials reads as follows in the horizontal slowness - frequency domain (p, z, ω):

$$V = \frac{-1}{i\omega\rho} \begin{pmatrix} -ip\omega\Phi - \frac{\partial\psi}{\partial z} \\ \frac{\partial\Phi}{\partial z} - ip\omega\psi \end{pmatrix}. \quad (3-35)$$

The z -derivatives of the up- and downgoing wave fields follow from (3-26):

$$\begin{aligned} \frac{\partial}{\partial z} \Phi^\pm(p, z, \omega) &= \mp i\omega q_p \Phi^\pm, \\ \frac{\partial}{\partial z} \psi^\pm(p, z, \omega) &= \mp i\omega q_s \psi^\pm. \end{aligned} \quad (3-36)$$

Substituting (3-25) in (3-35) and making use of (3-36), yields the following relation for the *composition* of the particle velocity from down- and upgoing P- and S-wave potentials:

$$V = L_1^+ D^+ + L_1^- D^-, \quad (3-37)$$

with the composition matrices defined by:

$$\mathbf{L}_1^\pm = \frac{1}{\rho} \begin{pmatrix} p & \mp q_s \\ \pm q_p & p \end{pmatrix}. \quad (3-38)$$

The relation between the traction and the velocity in the space - time domain (x, z, t), see Wapenaar and Berkhout (1989), p69, reads as follows:

$$\begin{aligned} \frac{\partial \tau_{xz}}{\partial t} &= \mu \left(\frac{\partial v_x}{\partial z} + \frac{\partial v_z}{\partial x} \right), \\ \frac{\partial \tau_{zz}}{\partial t} &= \lambda \nabla \cdot \mathbf{v} + 2\mu \frac{\partial v_z}{\partial z}. \end{aligned} \quad (3-39)$$

Using the transform pair for the temporal derivative

$$\frac{\partial}{\partial t} a(x, z, t) \leftrightarrow i\omega A(x, z, \omega), \quad (3-40)$$

and transform pair (3-22) yields the corresponding relation for the traction in the horizontal slowness - frequency domain:

$$\mathbf{T} = \begin{pmatrix} \mu \frac{\partial V_x}{\partial z} - i\omega p \mu V_z \\ -i\omega p \lambda V_x + (\lambda + 2\mu) \frac{\partial V_z}{\partial z} \end{pmatrix}. \quad (3-41)$$

Substituting (3-35) for the velocity in (3-41) and making use of the relations (3-36) for the z -derivatives yields the following expression for the composition of the traction from downgoing and upgoing P- and S-waves:

$$\mathbf{T} = \mathbf{L}_2^+ \mathbf{D}^+ + \mathbf{L}_2^- \mathbf{D}^-, \quad (3-42)$$

with the composition matrices defined by:

$$\mathbf{L}_2^\pm = \beta^2 \begin{pmatrix} \mp 2pq_p & q_s^2 - p^2 \\ p^2 - q_s^2 & \mp 2pq_s \end{pmatrix}. \quad (3-43)$$

Relations (3-37) and (3-42) can be combined to yield the *composition* of the total elastic wave field from downgoing and upgoing P- and S-waves:

$$\underbrace{\begin{pmatrix} \mathbf{V} \\ \mathbf{T} \end{pmatrix}}_{\mathbf{Q}} = \underbrace{\begin{pmatrix} \mathbf{L}_1^+ & \mathbf{L}_1^- \\ \mathbf{L}_2^+ & \mathbf{L}_2^- \end{pmatrix}}_{\mathbf{L}} \underbrace{\begin{pmatrix} \mathbf{D}^+ \\ \mathbf{D}^- \end{pmatrix}}_{\mathbf{P}} \quad (3-44)$$

or

$$\mathbf{Q} = \mathbf{L}\mathbf{P}. \quad (3-45)$$

Decomposition of the total elastic wave field into downgoing and upgoing P- and S-waves is achieved by the inverse of (3-44):

$$\begin{pmatrix} \mathbf{D}^+ \\ \mathbf{D}^- \end{pmatrix} = \begin{pmatrix} \mathbf{N}_1^+ & \mathbf{N}_2^+ \\ \mathbf{N}_1^- & \mathbf{N}_2^- \end{pmatrix} \begin{pmatrix} \mathbf{V} \\ \mathbf{T} \end{pmatrix} \quad (3-46)$$

or

$$\mathbf{P} = \mathbf{N}\mathbf{Q}, \quad (3-47)$$

with $\mathbf{N} = \mathbf{L}^{-1}$. The expressions for the decomposition matrices are given by:

$$\mathbf{N}_1^\pm = \rho\beta^2 \begin{pmatrix} p & \pm \frac{1}{2}(q_s^2 - p^2)/q_p \\ \mp \frac{1}{2}(q_s^2 - p^2)/q_s & p \end{pmatrix} \quad (3-48)$$

and

$$\mathbf{N}_2^\pm = \frac{1}{2} \begin{pmatrix} \mp p/q_p & -1 \\ 1 & \mp p/q_s \end{pmatrix}. \quad (3-49)$$

3.5.2 Boundary conditions

At a boundary between two elastic media, the traction and particle velocity vectors have to be continuous. Fig. 3-3 shows the general situation of four incident and four scattered waves. The boundary conditions state:

$$\lim_{z \downarrow z_0} \begin{pmatrix} \mathbf{V}(p, z, \omega) \\ \mathbf{T}(p, z, \omega) \end{pmatrix} = \lim_{z \uparrow z_0} \begin{pmatrix} \mathbf{V}(p, z, \omega) \\ \mathbf{T}(p, z, \omega) \end{pmatrix}. \quad (3-50)$$

Denoting the limits in the upper and lower half-space with the subscripts u and l respectively and making use of (3-44) yields:

$$\begin{pmatrix} \mathbf{L}_{1,u}^+ & \mathbf{L}_{1,u}^- \\ \mathbf{L}_{2,u}^+ & \mathbf{L}_{2,u}^- \end{pmatrix} \begin{pmatrix} \mathbf{D}_u^+ \\ \mathbf{D}_u^- \end{pmatrix} = \begin{pmatrix} \mathbf{L}_{1,l}^+ & \mathbf{L}_{1,l}^- \\ \mathbf{L}_{2,l}^+ & \mathbf{L}_{2,l}^- \end{pmatrix} \begin{pmatrix} \mathbf{D}_l^+ \\ \mathbf{D}_l^- \end{pmatrix}. \quad (3-51)$$

After rearranging terms, the following relation for the scattering results:

$$\begin{pmatrix} \mathbf{D}_u^- \\ \mathbf{D}_l^+ \end{pmatrix} = \underbrace{\begin{pmatrix} \mathbf{L}_{1,u}^- & -\mathbf{L}_{1,l}^+ \\ \mathbf{L}_{2,u}^- & -\mathbf{L}_{2,l}^+ \end{pmatrix}^{-1} \begin{pmatrix} -\mathbf{L}_{1,u}^+ & \mathbf{L}_{1,l}^- \\ -\mathbf{L}_{2,u}^+ & \mathbf{L}_{2,l}^- \end{pmatrix}}_{4 \times 4 \text{ scattering matrix}} \begin{pmatrix} \mathbf{D}_u^+ \\ \mathbf{D}_l^- \end{pmatrix}, \quad (3-52)$$

which can be compared with (3-33):

$$\begin{pmatrix} \mathbf{D}_u^-(p, z_0, \omega) \\ \mathbf{D}_l^+(p, z_0, \omega) \end{pmatrix} = \begin{pmatrix} \mathbf{R}^+(p) & \mathbf{T}^-(p) \\ \mathbf{T}^+(p) & \mathbf{R}^-(p) \end{pmatrix} \begin{pmatrix} \mathbf{D}_u^+(p, z_0, \omega) \\ \mathbf{D}_l^-(p, z_0, \omega) \end{pmatrix}. \quad (3-53)$$

After some manipulations, the following expressions result for the 2×2 submatrices of the scattering matrix:

$$\mathbf{R}^+(p) = \sum_{i=1,2} \mathbf{N}_{i,u}^- \mathbf{L}_{i,l}^+ \left(\sum_{i=1,2} \mathbf{N}_{i,u}^+ \mathbf{L}_{i,l}^+ \right)^{-1}, \quad (3-54a)$$

$$\mathbf{T}^+(p) = \sum_{i=1,2} \left(\mathbf{N}_{i,u}^+ \mathbf{L}_{i,l}^+ \right)^{-1}, \quad (3-54b)$$

$$\mathbf{R}^-(p) = \sum_{i=1,2} \mathbf{N}_{i,l}^+ \mathbf{L}_{i,u}^- \left(\sum_{i=1,2} \mathbf{N}_{i,l}^- \mathbf{L}_{i,u}^- \right)^{-1}, \quad (3-54c)$$

$$\mathbf{T}^-(p) = \sum_{i=1,2} \left(\mathbf{N}_{i,l}^- \mathbf{L}_{i,u}^- \right)^{-1}. \quad (3-54d)$$

Explicit expressions for the sixteen elements of the scattering matrix can be found in Cervený and Ravindra (1971) and Aki and Richards (1980). In both references, however, the scattering matrix is defined in terms of particle displacements rather than potentials. In Appendix A, relations are developed between the two types of scattering coefficients. In appendix B, explicit expressions for the potential coefficients are given.

3.6 Some properties of the scattering coefficients

3.6.1 Dependence on the elastic parameters

The explicit expressions for reflectivity and transmission of Appendix B are useful for an efficient computer implementation. However, some basic properties of the scattering coefficients can not easily be observed from these expressions. To reveal these properties, the system of equations that determines the scattering coeffi-

cients for the case of Fig. 3-2, an incident P-wave in the upper half-space, is given below:

$$\begin{bmatrix} \sin \phi_u & \frac{\alpha_u}{\beta_u} \cos \psi_u & -\frac{\rho_u \alpha_u}{\rho_l \alpha_l} \sin \phi_l & \frac{\rho_u \alpha_u}{\rho_l \beta_l} \cos \psi_l \\ -\cos \phi_u & \frac{\alpha_u}{\beta_u} \sin \psi_u & -\frac{\rho_u \alpha_u}{\rho_l \alpha_l} \cos \phi_l & -\frac{\rho_u \alpha_u}{\rho_l \beta_l} \sin \psi_l \\ \sin 2\phi_u & \frac{\alpha_u^2}{\beta_u^2} \cos 2\psi_u & \frac{\alpha_u^2 \beta_l^2}{\alpha_l^2 \beta_u^2} \sin 2\phi_l & -\frac{\alpha_u^2}{\beta_u^2} \cos 2\psi_l \\ \cos 2\psi_u & -\sin 2\psi_u & -\cos 2\psi_l & -\sin 2\psi_l \end{bmatrix} \begin{bmatrix} r_{11}^+(\phi_u) \\ r_{21}^+(\phi_u) \\ t_{11}^+(\phi_u) \\ t_{21}^+(\phi_u) \end{bmatrix} = \begin{bmatrix} -\sin \phi_u \\ -\cos \phi_u \\ \sin 2\phi_u \\ -\cos 2\psi_u \end{bmatrix} \quad (3-55)$$

These equations have been derived from the general case as given e.g. by Aki and Richards (1980) and by substituting the relations between particle velocity and potential coefficients that are given in Appendix A. The corresponding equations for the particle displacement coefficients are widely known as the Zoeppritz equations.

Note that the scattering coefficients in (3-55) are defined as a function of the incident angle ϕ_u instead of the ray parameter. All other angles are related to ϕ_u through Snell's law (3-31). This means that all angles are related to each other through the *ratios* of the velocities. Note that also in the other terms of (3-55) only velocity *ratios* appear. Also the densities appear solely in the terms as the ratio ρ_u/ρ_l . This means that the scattering as a function of the *angle* is completely determined by three velocity ratios (e.g. α_u/α_l , β_u/α_u and β_l/α_l) and the density ratio ρ_u/ρ_l . Of course, any other set of four parameters that is uniquely related to these four can equally well be considered to completely determine the *angle* dependent scattering. This result is not limited to the four scattering coefficients of (3-55), but is true for all sixteen scattering coefficients.

When considering the scattering as a function of the ray parameter instead of the incident angle, the absolute velocities become important. This is because the ray parameter is the ratio of the sine of the angle and the absolute velocity. So, the *p*-dependent scattering is effectively determined by five parameters: the four velocities and the density ratio.

3.6.2 Approximation formulas

The general behavior of the reflection coefficients as a function of the incident angle and the way they depend on the medium parameters can not easily be envisaged from the exact expressions of Appendix B. Fortunately, approximation formulas exist, that provide a good insight in the behavior of the reflectivity. Such

formulas have been published by a.o. Bortfeld (1961), Aki and Richards (1980) and Shuey (1985). The approximations are accurate for small parameter contrasts. They are not valid for postcritical angles.

The published approximations are linear in the relative parameter contrasts $\Delta x/\bar{x}$, with:

$$\begin{aligned}\Delta x &= x_l - x_u, \\ \bar{x} &= \frac{1}{2}(x_l + x_u),\end{aligned}\quad (3-56)$$

where x_u and x_l are the values of parameter x above and below the boundary. Aki and Richards (1980), give approximate expressions for all scattering coefficients. Only the approximations of the four reflection coefficients for an incident P- or S-wave in the upper half-space are reproduced below:

$$r_{pp}(\bar{\phi}) = R_{11}^+(p) \approx \frac{1}{2}(1 - 4\bar{\beta}^2 p^2) \frac{\Delta \rho}{\bar{\rho}} + \frac{1}{2\cos^2 \bar{\phi}} \frac{\Delta \alpha}{\bar{\alpha}} - 4\bar{\beta}^2 p^2 \frac{\Delta \beta}{\bar{\beta}}, \quad (3-57a)$$

$$\begin{aligned}r_{sp}(\bar{\phi}) = R_{21}^+(p) \approx & -\frac{p\bar{\beta}}{2\cos \bar{\psi}} \left[\left(1 - 2\bar{\beta}^2 p^2 + 2\bar{\beta}^2 \frac{\cos \bar{\phi}}{\bar{\alpha}} \frac{\cos \bar{\psi}}{\bar{\beta}} \right) \frac{\Delta \rho}{\bar{\rho}} \right. \\ & \left. - \left(4\bar{\beta}^2 p^2 - 4\bar{\beta}^2 \frac{\cos \bar{\phi}}{\bar{\alpha}} \frac{\cos \bar{\psi}}{\bar{\beta}} \right) \frac{\Delta \beta}{\bar{\beta}} \right],\end{aligned}\quad (3-57b)$$

$$\begin{aligned}r_{ps}(\bar{\psi}) = R_{12}^+(p) \approx & \frac{p\bar{\alpha}}{2\cos \bar{\phi}} \left[\left(1 - 2\bar{\beta}^2 p^2 + 2\bar{\beta}^2 \frac{\cos \bar{\phi}}{\bar{\alpha}} \frac{\cos \bar{\psi}}{\bar{\beta}} \right) \frac{\Delta \rho}{\bar{\rho}} \right. \\ & \left. + \left(4\bar{\beta}^2 p^2 - 4\bar{\beta}^2 \frac{\cos \bar{\phi}}{\bar{\alpha}} \frac{\cos \bar{\psi}}{\bar{\beta}} \right) \frac{\Delta \beta}{\bar{\beta}} \right],\end{aligned}\quad (3-57c)$$

$$r_{ss}(\bar{\psi}) = R_{22}^+(p) \approx \frac{1}{2}(1 - 4\bar{\beta}^2 p^2) \frac{\Delta \rho}{\bar{\rho}} + \left(\frac{1}{2\cos^2 \bar{\psi}} - 4\bar{\beta}^2 p^2 \right) \frac{\Delta \beta}{\bar{\beta}}, \quad (3-57d)$$

with the average angles $\bar{\phi}$ and $\bar{\psi}$ defined by:

$$\begin{aligned}\bar{\phi} &= \frac{1}{2}(\phi_u + \phi_l), \\ \bar{\psi} &= \frac{1}{2}(\psi_u + \psi_l).\end{aligned}\quad (3-58)$$

The original expressions of Aki and Richards (1980) are given in terms of particle displacements and the conversion relations of Appendix A have been used to transform them into the potential coefficients of (3-57a-d). Note that a less formal notation has been introduced for the reflection coefficients: r_{pp} , r_{sp} , r_{ps} and r_{ss} , where the first subscript denotes the type of reflected wave and the second subscript denotes the type of incident wave.

The PP approximation

Looking at these approximations, it is readily apparent that only the PP reflectivity depends on the relative contrast $\Delta\alpha/\alpha$ of the P-wave velocity. The other three reflectivity types depend only on the relative contrasts in S-wave velocity and density. Making use of $p = \sin \bar{\phi}/\bar{\alpha}$ and the exact relation $1/\cos^2 \bar{\phi} = 1 + \tan^2 \bar{\phi}$, the expression for the PP reflectivity can be written as:

$$r_{pp}(\bar{\phi}) = \underbrace{\frac{1}{2} \left(\frac{\Delta\rho}{\bar{\rho}} + \frac{\Delta\alpha}{\bar{\alpha}} \right) + \frac{1}{2} \frac{\Delta\alpha}{\bar{\alpha}} \tan^2 \bar{\phi}}_{\text{fluid factor}} - \underbrace{2 \frac{\bar{\beta}^2}{\bar{\alpha}^2} \left(\frac{\Delta\rho}{\bar{\rho}} + 2 \frac{\Delta\beta}{\bar{\beta}} \right) \sin^2 \bar{\phi}}_{\text{shear factor}}. \quad (3-59)$$

In analogy with Hiltermann (1983), the first (combined) term is called the fluid factor, since it is an approximation of the reflectivity of a fluid-fluid boundary, i.e. the acoustic reflectivity. The second term is called the shear factor, since it is proportional to the relative contrast of the shear modulus μ , one of the Lamé coefficients. With (3-17), it follows $\mu = \rho\beta^2$, so that the relative μ contrast is given by:

$$\frac{\Delta\mu}{\bar{\mu}} = \frac{\Delta\rho}{\bar{\rho}} + 2 \frac{\Delta\beta}{\bar{\beta}}. \quad (3-60)$$

For "normal" geologic layers, the magnitudes of the velocities and the density are correlated, so that the relative contrasts in α , β , and ρ will generally have the same sign. This means that the multipliers of the \sin^2 and \tan^2 terms in (3-59) have generally opposite signs, implying that the angle dependence of the elastic contrast is smaller than that of the corresponding acoustic contrast (same P-wave velocities and densities, zero S-wave velocities). Using $\sin^2 \bar{\phi} \approx \tan^2 \bar{\phi}$ and assuming a typical value of $\bar{\beta}/\bar{\alpha} = 1/2$ in (3-59) yields:

$$r_{pp}(\bar{\phi}) \approx \frac{1}{2} \left(\frac{\Delta\rho}{\bar{\rho}} + \frac{\Delta\alpha}{\bar{\alpha}} \right) + \frac{1}{2} \left(\frac{\Delta\alpha}{\bar{\alpha}} - \frac{\Delta\rho}{\bar{\rho}} - 2 \frac{\Delta\beta}{\bar{\beta}} \right) \sin^2 \bar{\phi}, \quad (3-61)$$

which shows clearly the opposite effects of fluid and shear terms.

As was already mentioned in Section 1.1, the strong angle dependence of reflections from gas sands has been one of the main reasons for the industry's interest in AVO techniques. This strong angle dependence can be easily explained with the above approximation formulas. As described in e.g. Ostrander (1984), gas fill strongly reduces the compression modulus k

$$k = \lambda + \frac{2\mu}{3}, \quad (3-62)$$

whereas the shear modulus μ remains practically constant. Since the P-wave velocity can be written as

$$\alpha = \sqrt{\frac{k + 4\mu/3}{\rho}}, \quad (3-63)$$

the gas fill will cause a strong decrease in P-wave velocity. Considering a boundary between a gas-filled and a brine-filled sand, this causes a negligible shear factor in (3-59) that will hardly influence the strong AVO behavior due to the large P-wave velocity contrast (the $\tan^2 \bar{\phi}$ term).

The SS approximation

Using $p \approx \sin \bar{\psi} / \bar{\beta}$ and the exact relation $1 / \cos^2 \bar{\psi} = 1 + \tan^2 \bar{\psi}$, the expression for the SS reflectivity (3-57d) can be written as:

$$\begin{aligned} r_{ss}(\bar{\psi}) &\approx \frac{1}{2} \left(\frac{\Delta \rho}{\bar{\rho}} + \frac{\Delta \beta}{\bar{\beta}} \right) - 2 \left(\frac{\Delta \rho}{\bar{\rho}} + \frac{\Delta \beta}{\bar{\beta}} \right) \sin^2 \bar{\psi} + \frac{1}{2} \frac{\Delta \beta}{\bar{\beta}} \tan^2 \bar{\psi}, \\ \sin \bar{\psi} \approx \tan \bar{\psi} &= \frac{1}{2} \left(\frac{\Delta \rho}{\bar{\rho}} + \frac{\Delta \beta}{\bar{\beta}} \right) - \left(2 \frac{\Delta \rho}{\bar{\rho}} + \frac{3}{2} \frac{\Delta \beta}{\bar{\beta}} \right) \sin^2 \bar{\psi}. \end{aligned} \quad (3-64)$$

Assuming again parameter contrasts of the same sign, the normal incidence term and the \sin^2 term have opposite signs. Because the multiplier of $\sin^2 \bar{\psi}$ is between 3 and 4 times larger than the normal incidence term, the SS reflectivity will usually exhibit a polarity reversal at a certain angle. Although possible, this is quite uncommon for PP reflectivity.

A second important observation is that for parameter contrasts of the same sign, the angle dependence of the SS reflectivity is much larger than that of the PP reflectivity, as can be seen by comparing the \sin^2 terms in (3-61) and (3-64).

3.6.3 Examples

It is instructive to plot some reflectivity curves in order to demonstrate some of the properties that have been derived in the previous section. Table 3-2 defines the elastic parameters of the models that will be used for the examples. Note that models 3 and 4 are obtained from models 2 and 1 by simply interchanging the upper and lower half-spaces. Likewise, models 7 and 8 are obtained from models 5 and 6. Models 1-4 are chosen such that $\Delta \beta / \bar{\beta} = \frac{1}{2} \Delta \alpha / \bar{\alpha}$ and $\Delta \rho / \bar{\rho} = 0$ so that the \tan^2 and \sin^2 terms in (3-59) will approximately cancel each other. The resulting exact and approximated PP reflectivity curves are shown in Fig. 3-6. The angle dependence is indeed very small for angles up to 35° . It is also apparent that for precritical angles, the difference between the approximated and the exact reflectivity curves is negligible. The PP reflectivity curves of models 1 and 2 exhibit critical angles at $\phi_u = \arcsin \alpha_u / \alpha_l$. Beyond these angles, the reflectivity becomes complex valued and is not plotted anymore in Fig. 3-5.

Models 5-8 have the same P-wave velocities as models 1-4. However, the S-wave velocity and the density are now anticorrelated with the P-wave velocity: $\Delta\beta/\bar{\beta} = -\Delta\alpha/\bar{\alpha}$ and $\Delta\rho/\bar{\rho} = -\frac{1}{2}\Delta\alpha/\bar{\alpha}$. According to (3-59), this should lead to a pronounced amplitude increase with offset, which can indeed be observed from Fig. 3-6. Now there is a marked difference between the approximated and the exact reflectivity, although the approximation is still very accurate.

The accuracy of the approximation formulas is often not as good as pictured in Figures 3-5 and 3-6. Many elastic models with parameter contrasts comparable to the ones shown here, will have a larger error in the approximated reflectivity, see Bortfeld (1961), Fig. 5. Another factor that contributes to the accuracy is that the approximated reflectivity is plotted as a function of the true incident angle ϕ_u rather than as a function of the average angle $\bar{\phi}$ as defined by (3-58). When approaching the critical angle, the difference between these two becomes large.

Of model 5, the amplitude and phase of the four different reflectivity types (PP, PS, SP and SS) are plotted in Fig. 3-7. Note that the SS reflectivity has two critical angles at $\psi_u = \arcsin \beta_u/\alpha_u$ and $\psi_u = \arcsin \beta_u/\alpha_l$, respectively 38.7° and 30° . At these angles, the converted P-waves in the upper respectively lower half-spaces become evanescent. Only when $\beta_u < \beta_l$, the SS reflectivity has a third critical angle at $\arcsin \beta_u/\beta_l$. The zero crossing of the SS reflectivity, predicted by (3-64) is at 26.5° . Note that in the limit of ϕ_u or ψ_u approaching 90° , the reflection coefficients r_{pp} and r_{ss} are real and equal to -1 . At this limit, there are no wave conversions; $r_{sp} = r_{ps} = 0$.

Table 3-2 The elastic parameters of the 'dual half-space' elastic models.

| Model No. | α_u | α_l | β_u | β_l | ρ_u | ρ_l | σ_u | σ_l |
|-----------|------------|------------|-----------|-----------|----------|----------|------------|------------|
| 1 | 0.8 | 1.0 | 0.447 | 0.500 | 1.00 | 1.00 | 0.273 | 0.333 |
| 2 | 0.9 | 1.0 | 0.474 | 0.500 | 1.00 | 1.00 | 0.308 | 0.333 |
| 3 | 1.0 | 0.9 | 0.500 | 0.474 | 1.00 | 1.00 | 0.333 | 0.308 |
| 4 | 1.0 | 0.8 | 0.500 | 0.447 | 1.00 | 1.00 | 0.333 | 0.273 |
| 5 | 0.8 | 1.0 | 0.500 | 0.400 | 1.00 | 0.89 | 0.179 | 0.405 |
| 6 | 0.9 | 1.0 | 0.444 | 0.400 | 1.00 | 0.95 | 0.339 | 0.405 |
| 7 | 1.0 | 0.9 | 0.400 | 0.444 | 0.95 | 1.00 | 0.405 | 0.339 |
| 8 | 1.0 | 0.8 | 0.400 | 0.500 | 0.89 | 1.00 | 0.405 | 0.179 |

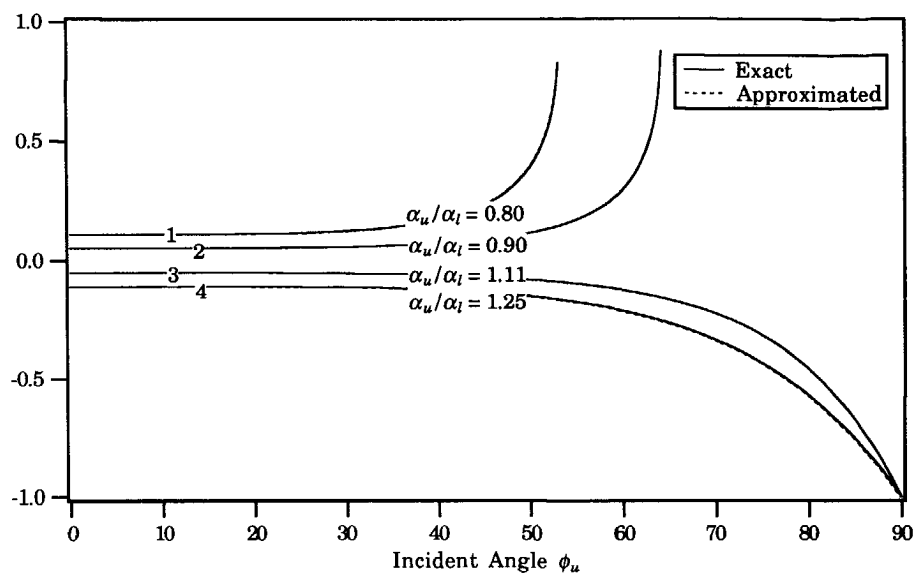


Fig. 3-5 Exact and approximated precritical PP reflectivity curves for models 1-4. The approximated and exact reflectivity curves practically overlaid each other.

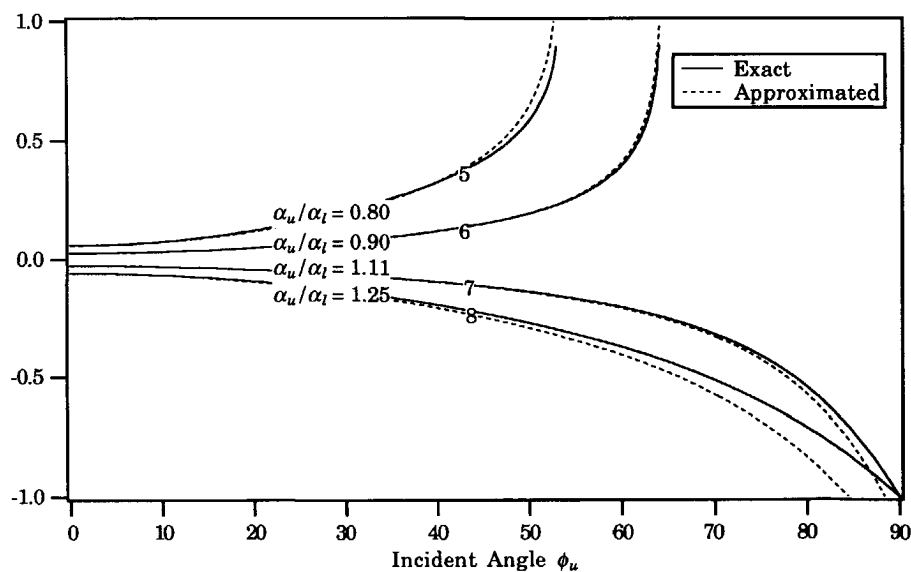


Fig. 3-6 Exact and approximated precritical PP reflectivity curves for models 5-8.

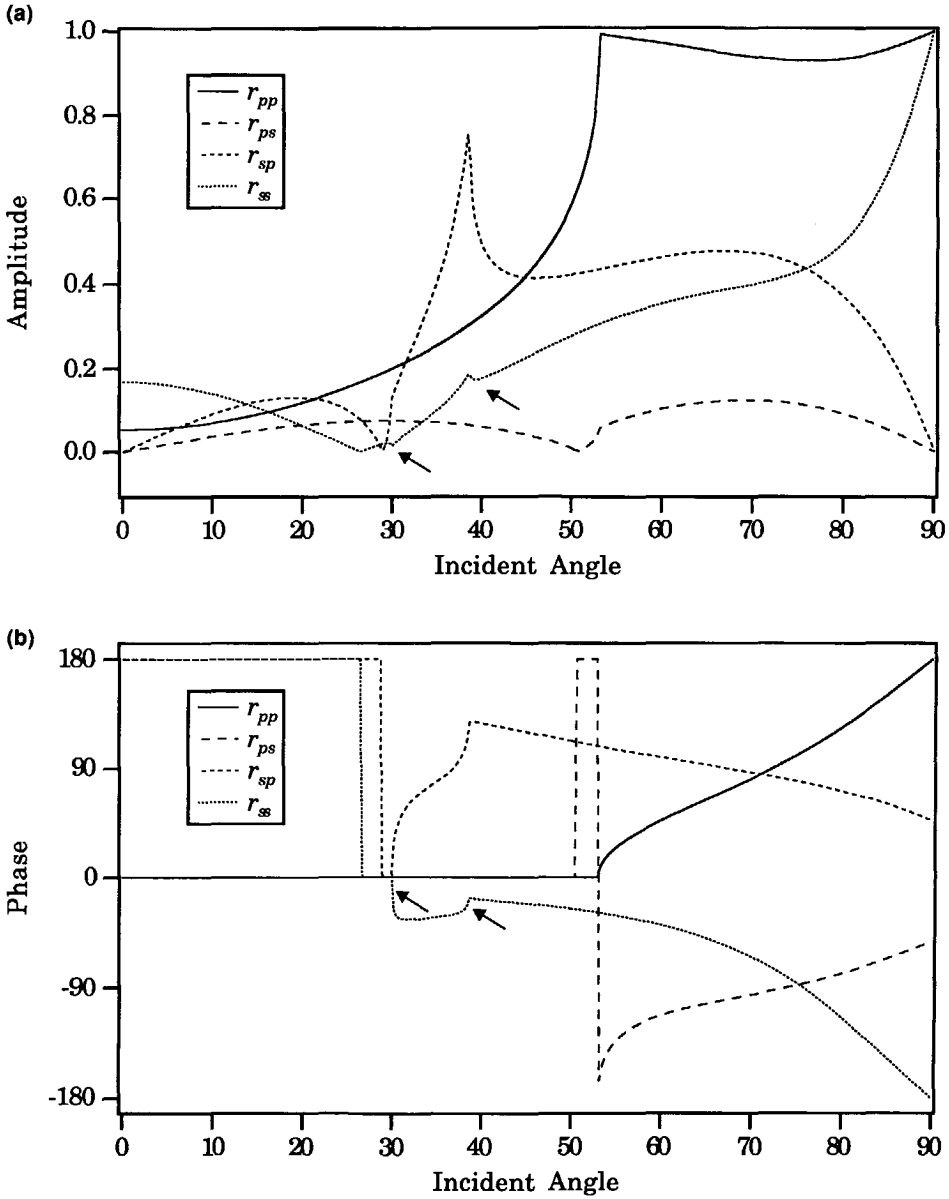


Fig. 3-7 Amplitude (a) and phase (b) of the PP, PS, SP and SS reflectivity of model 5 (see Table 3-2), plotted as a function of the incident angle, being θ_u for the PP and PS reflectivity and ϕ_u for the SP and SS reflectivity. The two critical angles of the SS reflectivity are indicated by arrows.

4 Forward modeling in the horizontal slowness - frequency domain

4.1 Introduction

As was already mentioned in Chapter 2, the horizontal slowness - intercept time domain (p - τ) has been chosen for the inversion. Since the iterative nonlinear inversion procedure requires several forward modeling steps, it is important that the forward modeling is fast. Because of the full-waveform character of the inversion procedure, it is also important that the forward modeling correctly models phase shifts due to postcritical reflection as well as multiples and conversions. The so-called reflectivity method in the p - τ domain satisfies these two requirements.

It is computationally advantageous to remain in the slowness domain. As will appear later, an integration over the ray parameter (or equivalently, horizontal wavenumber) is required to obtain the response in the x - t domain. For this integration, the ray parameter needs to be densely sampled to prevent aliasing in the x -direction. Since five parameters determine the reflectivity of an elastic boundary, see Section 3.6.1, only five traces with different ray parameter would theoretically suffice to estimate the elastic parameters of a layered model. In practice, one will use more traces in order to suppress noise, but the number of traces (say 10-25) will be typically more than ten times smaller than the number of traces that would be required for an inverse transformation.

4.2 The reflectivity method

4.2.1 Introduction

The reflectivity method was originally developed by Fuchs (Fuchs 1968) to calculate the x - t response of a medium with arbitrary depth dependent properties. In the original algorithm, the source is supposed to be located in either a top or bottom half-space. Later, extensions have been developed to allow for a free surface and an arbitrary source location within the 1D model, see Müller (1985). Kennett (1974) developed an elegant recursive formulation for the 1D problem. In Berkhout

(1982), Chapter 6, it is demonstrated that the same recursive formulation can also be applied to the general case of an inhomogeneous medium with arbitrary source and receiver positions.

For the inversion application that is discussed here, the data have been obtained through a redatuming procedure and it can be assumed that the source and receivers are effectively located in an upper half-space. Furthermore, it will be assumed that the (target) medium consists of a stack of homogeneous elastic layers with arbitrary thickness. The general situation of a stack of layers between two half-spaces is pictured in Fig. 4-1. As can be expected, the notion of reflectivity plays a crucial role in the reflectivity method. For downgoing incident waves in the upper half-space, the 2×2 global reflectivity matrix \mathbf{G} is defined at any level z within the layered medium by:

$$\mathbf{D}^-(p, z, \omega) = \mathbf{G}(p, z, \omega) \mathbf{D}^+(p, z, \omega), \quad (4-1)$$

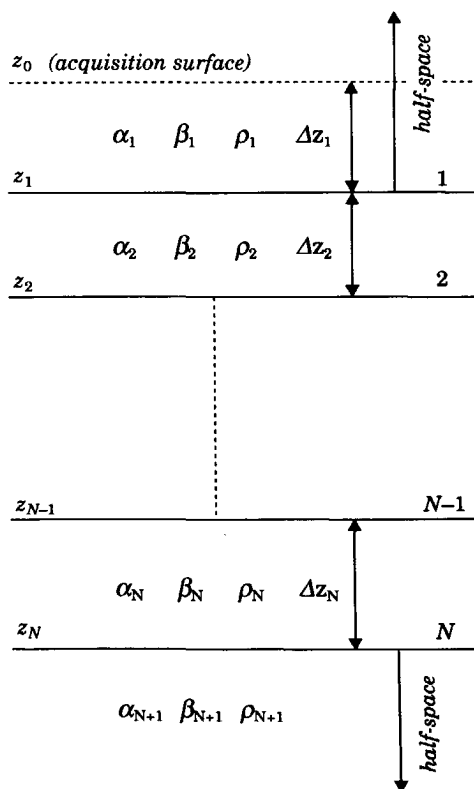


Fig. 4-1 Layered medium consisting of $N-1$ homogeneous layers between two half-spaces. Note that the interface indices run from 1 up to N .

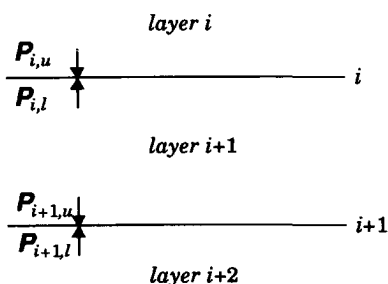


Fig. 4-2 The wave fields $\mathbf{P} = (\Phi^+, \Psi^+, \Phi^-, \Psi^-)^t$ are defined at the interface locations as the limits coming from above (u) and below (l) the interface.

with $\mathbf{D}^{\pm}=(\Phi^{\pm}, \Psi^{\pm})^t$. The term global reflectivity is used as opposite to local reflectivity, i.e. the reflectivity of a single boundary. The reader is referred to Table 3-1 on page 19 for the notation convention. The global reflectivity matrix at level z describes all reflections (including multiples and conversions) that occur below z . Assuming that the source and the receivers are located at level z_0 within the upper half-space, the plane-wave response of the stack of layers is given by $\mathbf{G}(p, z_0, \omega)$. Using $k_x=p\omega$, a double inverse transform yields the response in the x - t domain:

$$d(x, z_0, t) = \frac{1}{2\pi^2} \text{Re} \left[\int_0^{\infty} d\omega e^{i\omega t} \int_{-\infty}^{\infty} \underbrace{dp \omega}_{k_x} \mathbf{G}(p, z_0, \omega) \mathbf{S}(p, \omega) e^{-i\omega p x} \right], \quad (4-2)$$

where \mathbf{S} is the source function. The integral over p requires an adequately small sampling to give an accurate, unaliased x - t section. As mentioned before, the inversion procedure uses p - τ data and therefore the integration over p is not needed. The p - τ data are simply obtained by an inverse temporal Fourier transform:

$$d(p, z_0, \tau) = \frac{1}{\pi} \text{Re} \left[\int_0^{\infty} \mathbf{G}(p, z_0, \omega) \mathbf{S}(p, \omega) e^{i\omega \tau} d\omega \right]. \quad (4-3)$$

Note that the source function \mathbf{S} is a 2×1 vector with a P-wave and an S-wave component. By using a pure P-wave and a pure S-wave source consecutively, the four reflectivity gathers (PP, SP, PS and SS) are obtained. Note that exactly these four gathers are the output from the redatuming step in the DELPHI scheme of Fig. 2-1.

The main problem that needs to be addressed is the calculation of the global reflectivity matrix. In Section 4.2.2, a simple procedure will be introduced, that allows a simple formulation of the global reflectivity. Unfortunately, this procedure is numerically unstable for the evanescent part of the wave field. A stable recursive formulation, due to Kennett (1974), will be discussed in Section 4.3. The latter algorithm will be used in the forward modeling part of the iterative elastic inversion.

4.2.2 The propagator method

A conceptually simple scheme to calculate the reflectivity makes use of the so-called propagator matrices, originally introduced by Haskell (1953), see also Gilbert and Backus (1966). The method is usually presented in terms of stresses and particle velocities, but in this section, the potentials for up- and downgoing waves are used.

Considering Fig. 4-2, it is supposed that the wavefield $\mathbf{P}_{i+1,u}$ just above boundary $i+1$ is known. As defined by (3-44), the 4×1 vector $\mathbf{P}=(\Phi^+, \Psi^+, \Phi^-, \Psi^-)^t$ contains both

up- and downgoing P- and S-waves. First, the wavefield is propagated upwards through layer $i+1$ to a level just below the boundary i . With relation (3-26), it follows that the wavefield extrapolation can simply be accomplished with:

$$\mathbf{P}_{i,l} = \mathbf{W}_{i+1} \mathbf{P}_{i+1,u}, \quad (4-4)$$

with

$$\begin{aligned} \mathbf{W}_{i+1} &= \begin{pmatrix} \mathbf{F}_{i+1}^+ & \mathbf{0} \\ \mathbf{0} & \mathbf{W}_{i+1}^- \end{pmatrix}, \\ \mathbf{F}_i^+ &= \text{diag} \left\{ \exp^{i\omega q_{p,i} \Delta z_i}, \exp^{i\omega q_{s,i} \Delta z_i} \right\}, \\ \mathbf{W}_i^- &= \text{diag} \left\{ \exp^{-i\omega q_{p,i} \Delta z_i}, \exp^{-i\omega q_{s,i} \Delta z_i} \right\}, \quad \Delta z_i = z_i - z_{i-1}, \end{aligned} \quad (4-5)$$

where the vertical slownesses q_p, q_s are defined by (3-28) or (3-29).

$\mathbf{P}_{i,l}$ can be easily transmitted upwards through the boundary by making use of the boundary conditions (3-50) that state that the particle velocity and the traction be continuous. Making use of the composition relation (3-45), the upward transmission through boundary i is established with:

$$\mathbf{P}_{i,u} = \mathbf{L}_i^{-1} \mathbf{L}_{i+1} \mathbf{P}_{i,l}, \quad (4-6)$$

where the subscripts u and l denote the limits approaching from above and below the boundary:

$$\begin{aligned} \mathbf{P}_{i,u} &= \lim_{z \uparrow z_i} \mathbf{P}(p, z, \omega), \\ \mathbf{P}_{i,l} &= \lim_{z \downarrow z_i} \mathbf{P}(p, z, \omega). \end{aligned} \quad (4-7)$$

The composition matrices \mathbf{L} only depend on the medium parameters (not on depth within the layer) and are subscripted with the layer number.

Relations (4-4) and (4-6) together propagate the wavefield \mathbf{P} exactly one layer upward. A repeated application of these equations, starting with $\mathbf{P}_{i,l}$ just below the deepest boundary, yields the following expression for the wavefield at the acquisition level z_0 :

$$\mathbf{P}(p, z_0, \omega) = \mathbf{P}_0 = \underbrace{\prod_{i=1}^N [\mathbf{W}_i \mathbf{L}_i^{-1} \mathbf{L}_{i+1}]}_{\mathbf{X}} \mathbf{P}_{N,l}, \quad (4-8)$$

with the obvious order for the matrix multiplications, $i=1$ on the left and $i=N$ on the right. In order to obtain the global reflectivity at the surface, the "bottom to top" propagator matrix \mathbf{X} is calculated. Using $\mathbf{P}=(\mathbf{D}^+, \mathbf{D}^-)^t$ in (4-8) results in:

$$\begin{pmatrix} \mathbf{D}_0^+ \\ \mathbf{D}_0^- \end{pmatrix} = \begin{pmatrix} \mathbf{X}_{11} & \mathbf{X}_{12} \\ \mathbf{X}_{21} & \mathbf{X}_{22} \end{pmatrix} \begin{pmatrix} \mathbf{D}_{N,l}^+ \\ \mathbf{D}_{N,l}^- \end{pmatrix}. \quad (4-9)$$

In the lower half-space, only downgoing waves can exist, so that $\mathbf{D}_{N,l}^- = \mathbf{0}$. After elimination of $\mathbf{D}_{N,l}^+$, the following relation results:

$$\mathbf{D}_0^- = \mathbf{X}_{21} \mathbf{X}_{11}^{-1} \mathbf{D}_0^+, \quad (4-10a)$$

so that the global reflectivity at the surface is given by:

$$\mathbf{G}_0 = \mathbf{X}_{21} \mathbf{X}_{11}^{-1}. \quad (4-10b)$$

Unfortunately, (4-8) is numerically unstable for the evanescent part of the wave field. This is due to the inverse extrapolation operator \mathbf{F}_i^+ that has to undo the exponential decrease of amplitude with depth for the evanescent part of the downgoing wave field. For an evanescent P-wave in layer i , the vertical slowness $q_{p,i}$ becomes imaginary according to (3-29), yielding

$$\mathbf{F}_i^+(1,1) = \exp\left\{\omega \Delta z_i \sqrt{p^2 - 1/\alpha_i^2}\right\}, \quad (4-11)$$

which is a real positive quantity that is larger than unity. To illustrate that this factor can easily get very large, the following example is given: Assume a layer of 250m thickness with $\alpha=2000\text{m/s}$ and $\beta=1000\text{m/s}$ and choose p such that the P-wave is evanescent while the S-wave propagates under 45 degrees with the normal. At a frequency of 60Hz, equation (4-11) results in $\mathbf{F}_i^+(1,1) = 2.9 \times 10^{20}$ so that small numerical errors will blow up. For the propagating S-wave however, the action of \mathbf{F}_i^+ is a mere phase shift. A numerical solution has been developed (Dunkin 1965) that involves the so-called Haskell-Dunkin 6×6 matrices, see Phinney et al. (1987). However, the elegant recursive procedure due to Kennett (1974) is preferred here, since it requires a smaller programming effort and has a smaller operations count.

4.3 Recursive reflectivity algorithm

4.3.1 Theory

In the method of the previous section, the total wavefield in terms of up- and downgoing waves is propagated upwards. In the recursive method of Kennett (1974), one can say that the global reflectivity matrix is "propagated" upwards.

Considering Fig. 4-1a, suppose that the global reflectivity just above boundary $i+1$ is known:

$$D_{i+1,u}^- = G_{i+1,u} D_{i+1,u}^+ . \quad (4-12)$$

The reflectivity is first propagated upward through layer $i+1$, i.e. from level A to B. With $D^\pm = (\phi^\pm, \psi^\pm)^t$ and using (4-4) and (4-5) yields:

$$\begin{aligned} D_{i,l}^- &= W_{i+1}^- D_{i+1,u}^- , \\ D_{i,l}^+ &= F_{i+1}^+ D_{i+1,u}^+ . \end{aligned} \quad (4-13)$$

As follows from (4-5), F_{i+1}^+ is the inverse of W_{i+1}^- , so that the following expression results for the reflectivity at level B just below boundary i :

$$D_{i,l}^- = W_{i+1}^- G_{i+1,u} W_{i+1}^- D_{i,l}^+ , \quad (4-14a)$$

or

$$D_{i,l}^- = G_{i,l} D_{i,l}^+ \quad (4-14b)$$

with

$$G_{i,l} = W_{i+1}^- G_{i+1,u} W_{i+1}^- . \quad (4-14c)$$

Contrary to the propagation rule (4-4), the propagation of the global reflectivity only involves multiplications by W^- . The modulus of the elements of W^- is smaller

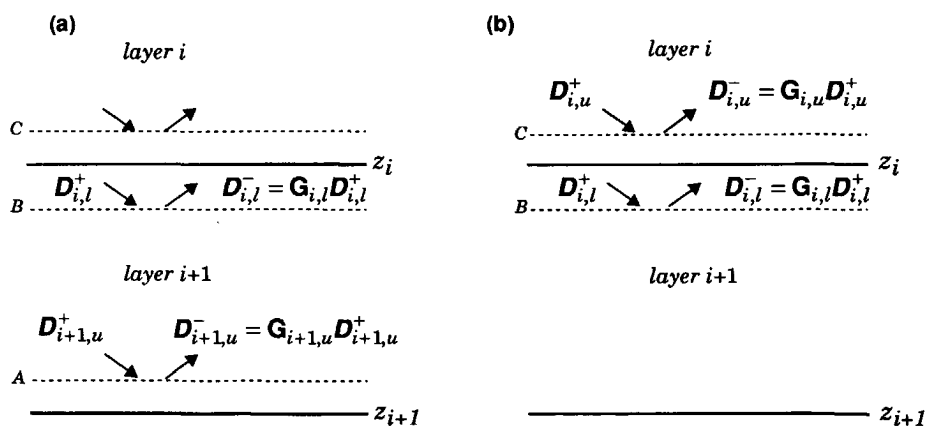


Fig. 4-1 Upward "propagation" of the global reflectivity matrix G . The levels A, B and C are actually infinitesimally close to the respective interfaces. (a) Propagation through a homogeneous layer. (b) Transmission through a boundary.

than or equal to unity for all ray parameters, so that (4-14c) will never introduce an instability.

The next step is to transmit the reflectivity upward through the boundary i , i.e. from level B to C as pictured in Fig. 4-1b. This involves the local reflection (\mathbf{R}_i^+ , \mathbf{R}_i^-) and transmission matrices (\mathbf{T}_i^+ , \mathbf{T}_i^-) of the i^{th} boundary. Rewriting (3-33) yields:

$$\begin{aligned} \mathbf{D}_{i,u}^- &= \mathbf{R}_i^+ \mathbf{D}_{i,u}^+ + \mathbf{T}_i^- \mathbf{D}_{i,l}^-, \\ \mathbf{D}_{i,l}^+ &= \mathbf{T}_i^+ \mathbf{D}_{i,u}^+ + \mathbf{R}_i^- \mathbf{D}_{i,l}^-. \end{aligned} \quad (4-15)$$

With the aid of (4-14b), $\mathbf{D}_{i,l}^+$ is eliminated from the above equations by substituting

$$\mathbf{D}_{i,l}^+ = \mathbf{G}_{i,l}^{-1} \mathbf{D}_{i,l}^-. \quad (4-16)$$

From the resulting two equations, $\mathbf{D}_{i,l}^-$ is eliminated, yielding:

$$\mathbf{D}_{i,u}^- = \left[\mathbf{R}_i^+ - \mathbf{T}_i^- (\mathbf{R}_i^- - \mathbf{G}_{i,l}^{-1})^{-1} \mathbf{T}_i^+ \right] \mathbf{D}_{i,u}^+, \quad (4-17)$$

which defines the global reflectivity $\mathbf{G}_{i,u}$ at position C, just above boundary i . The expression can be rewritten by making use of the matrix identity $[\mathbf{P}^{-1} + \mathbf{Q}]^{-1} = \mathbf{P}[\mathbf{I} + \mathbf{QP}]^{-1}$ to yield:

$$\mathbf{D}_{i,u}^- = \mathbf{G}_{i,u} \mathbf{D}_{i,u}^+, \quad (4-18a)$$

$$\mathbf{G}_{i,u} = \mathbf{R}_i^+ + \mathbf{T}_i^- \mathbf{G}_{i,l} (\mathbf{I} - \mathbf{R}_i^- \mathbf{G}_{i,l})^{-1} \mathbf{T}_i^+. \quad (4-18b)$$

This equation is essentially identical to equation (30) of Kennett (1974). Equations (4-14c) and (4-18b) propagate the global reflectivity exactly one layer upwards.

The calculation of the global reflectivity starts just above the lowest interface where the global reflectivity is equal to the local reflectivity for downgoing waves: $\mathbf{G}_{N,u} = \mathbf{R}_N^+$. A recursive application of (4-14c) and (4-18b) will subsequently yield the global reflectivity $\mathbf{G}_0 = \mathbf{G}(p, z_0, \omega)$ at the surface.

4.3.2 An Interpretation in terms of rays

The inverse term in (4-18b) can be expanded in a power series:

$$\mathbf{G}_{i,u} = \mathbf{R}_i^+ + \mathbf{T}_i^- \mathbf{G}_{i,l} \sum_{n=0}^{\infty} (\mathbf{R}_i^- \mathbf{G}_{i,l})^n \mathbf{T}_i^+. \quad (4-19)$$

The first term of this expression, \mathbf{R}_i^+ , is simply the reflection from the i^{th} boundary. As will appear shortly, the other term that contains the infinite series represents

all reflections *below* the i^{th} boundary. In Fig. 4-2 the first three terms of this series are shown with their corresponding rays. Note that the matrix multiplications should be read from the left to the right to allow an easy comparison with the pictorial representation. The first term represents all ray paths that have two "legs" in layer $i+1$. The second term represents all ray paths that have four "legs" in layer $i+1$ and so on. The second order and higher terms represent *all* multiple reflections that involve the i^{th} boundary and whose ray paths are completely below it.

With the power series expansion, the modeling algorithm can be easily modified to generate only multiples up to a certain order or no multiples at all. Another option is to model without wave conversions, which can be accomplished by setting the off-diagonal terms of the local reflection and transmission matrices to zero.

4.3.3 Implementation aspects

Since the speed of the forward modeling largely determines the duration of the inversion, a discussion of some implementation aspects is appropriate. The generation of the p - τ seismograms basically consists of two steps:

- 1) Calculation of the global reflectivity $\mathbf{G}(p, 0, \omega)$ at the surface for a number of ray parameters and frequencies. The frequencies are regularly sampled.
- 2) Per ray parameter trace, a multiplication with the source function and an inverse temporal Fourier transform.

Of these, step 1) mainly determines the computation time. As is shown in the algorithm below, the calculation of $\mathbf{G}(p, 0, \omega)$ consists of three loops:

For all ray parameters do

For boundary $i = N, (-1), 1$ do

Calculate the local scattering matrix for boundary i .

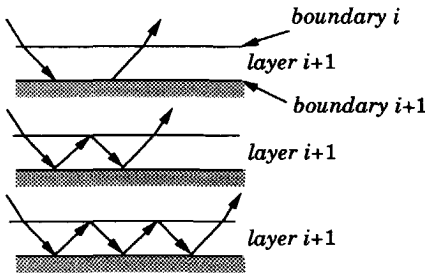
$$\begin{aligned}
 & \mathbf{T}_i^- \mathbf{G}_{i,l} \mathbf{T}_i^+ \\
 & + \mathbf{T}_i^- \mathbf{G}_{i,l} \mathbf{R}_i^- \mathbf{G}_{i,l} \mathbf{T}_i^+ \\
 & + \mathbf{T}_i^- \mathbf{G}_{i,l} \mathbf{R}_i^- \mathbf{G}_{i,l} \mathbf{R}_i^- \mathbf{G}_{i,l} \mathbf{T}_i^+ \\
 & + \text{Higher order terms}
 \end{aligned}$$


Fig. 4-2 Expansion of the multiple generating term of equation (4-19).

For all frequencies do

Calculate \mathbf{G} using (4-14c) and (4-18b).

The local scattering coefficients are frequency independent and can therefore be calculated outside the frequency loop. The explicit expressions of Appendix B are used in the implementation. The frequency loop is chosen as the inner loop because this allows vectorization of the algorithm. If the boundary and frequency loops had been interchanged, vectorization would not have been possible because of the recursive nature of relation (4-18b).

The recursive reflectivity calculation consists of 2×2 matrix operations. These can easily be expanded into expressions for the individual four components. Since the frequency loop is the innermost one, all matrix elements (including partial results) need to be stored in complex *arrays* of length N_{REQ} , the number of frequencies to be modeled.

For the inversion application, the ray parameter range of the modeling should approximately match that of the input data. The ray parameter interval does not need to obey a strict sampling criterion. Using 10 to 25 different ray parameters is generally sufficient. The number of frequencies and the sampling interval depend in the usual way on the frequency content of the source and the duration of the response.

4.4 Behavior at a horizontal slowness equal to the slowness of a layer

For horizontal slownesses that are exactly equal to the reciprocal of the P- or S-wave velocity of one of the *embedded* layers, the plane-wave response cannot be calculated in a straightforward fashion. This problem is not due to the specific algorithm that is used, but is of a more fundamental nature.

For the inversion application, it is necessary to model p - τ data for horizontal slowness ranges that one may encounter in practice in the redatumed gathers. For the SS gathers, this range will often include p -values equal to the reciprocals of the P-wave velocities. At such horizontal slownesses, the matrix $\mathbf{I} - \mathbf{R}_i^* \mathbf{G}_{i,j}$ in (4-18b), whose inverse generates the multiples, becomes singular. As will be demonstrated, this is due to the P-wave multiples whose contribution becomes unbounded when p approaches $1/\alpha$.

From a ray theory point of view, an explanation can best be given using an acoustic example. Consider Fig. 4-3 where the case of a single layer embedded between two half-spaces has been pictured. The global reflection coefficient $G_{I,u}$ just above the first interface is given by the scalar equivalents of (4-14c) and (4-18b):

$$G_{1,l} = e^{-2i\omega q_2 \Delta z} R_2^+, \quad (4-20a)$$

and

$$G_{1,u} = R_1^+ + \frac{T_1^- G_{1,l} T_1^+}{1 - R_1^- G_{1,l}} \quad (4-20b)$$

where the vertical slowness q in a layer is defined by:

$$q = \begin{cases} \sqrt{1/c^2 - p^2}, & p^2 \leq 1/c^2 \\ -i\sqrt{p^2 - 1/c^2}, & p^2 > 1/c^2 \end{cases} \quad (4-21)$$

and c is the acoustic velocity.

When the horizontal slowness approaches $1/c_2$, the vertical slowness q_2 in the layer becomes zero. This means that ϕ approaches 90 degrees, i.e. the waves in the embedded layer propagate almost horizontally. The two-way vertical traveltime $2q_2 \Delta z$ in the layer approaches zero, so that all multiples (in the p - τ domain) will have zero traveltime. For p approaching $1/c_2$, the local scattering coefficients become:

$$R_1^- \rightarrow -1, \quad R_2^+ \rightarrow -1, \quad T_1^- \rightarrow 0, \quad (4-22a)$$

$$R_1^+ \rightarrow 1, \quad T_1^+ \rightarrow 2. \quad (4-22b)$$

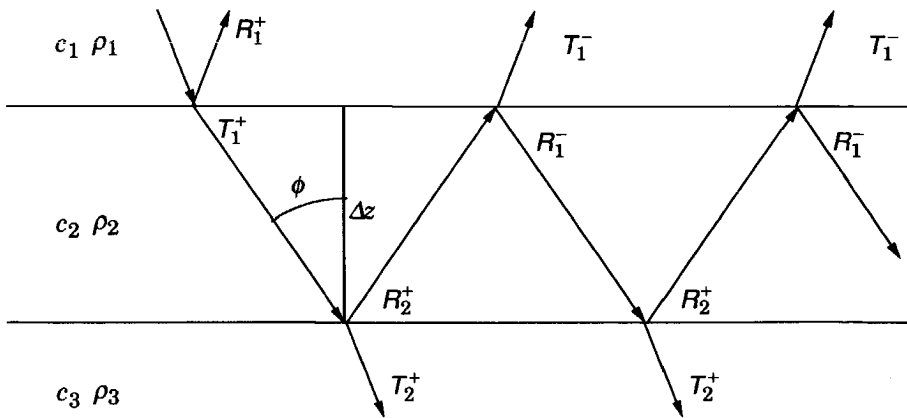


Fig. 4-3 Multiples in an acoustic layer that is embedded between two acoustic half-spaces.

Since $q_2=0$, it results from (4-20a) that $G_{1,l}=-1$ so that the numerator of the second term of (4-20b), $1-R_1^-G_{1,l}$, is zero.

The physical explanation for this is that all multiples have equal strength ($R_2^+ = R_1^- = -1$) and zero traveltimes, so that all contributions are in phase and the sum over all orders of multiples—the acoustic equivalent of (4-19)—does not converge. When limiting the calculation to a multiples up to a certain order, the instability will not occur.

The upward transmission T_1^- approaches zero, however, so that in equation (4-20b) a “zero divided by zero” situation results, for which the limit may exist. A numerical calculation of the global reflectivity $G_{1,u}$ for $p=1/c_2\pm\varepsilon$, with a small, positive ε yields effectively equal results. This supports the assumption that the limit for p approaching $1/c_2$ indeed exists.

For the *elastic* case, the upper left elements of the local scattering matrices (the PP elements) behave as (4-22a) for p equal to the reciprocal of the P-wave velocity. Therefore, the acoustic discussion of this section also explains the behavior of the elastic case. If the actual elastic modeling algorithm encounters a horizontal slowness that is equal to the reciprocal of a layer velocity, the value of the slowness is slightly altered, so that a numerical approximation to the limiting solution is obtained. At ray parameters equal to the reciprocal of the S-wave velocity of one of the *embedded* layers, a similar instability is encountered. The same procedure can be applied. As already mentioned in Section 4.3.2, the option also exists to use only a limited number of terms from the multiple series (4-19), in which case the instability will not occur.

4.5 Example

To illustrate some properties of the p - τ gathers of the four different reflectivity types, an example will be given. The elastic model that is used, consists of a layer of 50m thickness embedded between two half-spaces; its parameters are given in Table 4-1. The registration surface is 50m above the first interface. For the model-

Table 4-1 Parameters of the elastic model used in the example.

| Layer | α | $1/\alpha$ | β | $1/\beta$ | ρ | σ | Δz |
|-------|----------|---------------|---------|---------------|--------------------|----------|------------|
| | m/s | 10^{-6} s/m | m/s | 10^{-6} s/m | gr/cm ³ | | m |
| 1 | 2000 | 500 | 1000 | 1000 | 1 | 0.33 | 50 |
| 2 | 3000 | 333 | 1500 | 667 | 1 | 0.33 | 50 |
| 3 | 4000 | 250 | 2500 | 400 | 1 | 0.18 | |

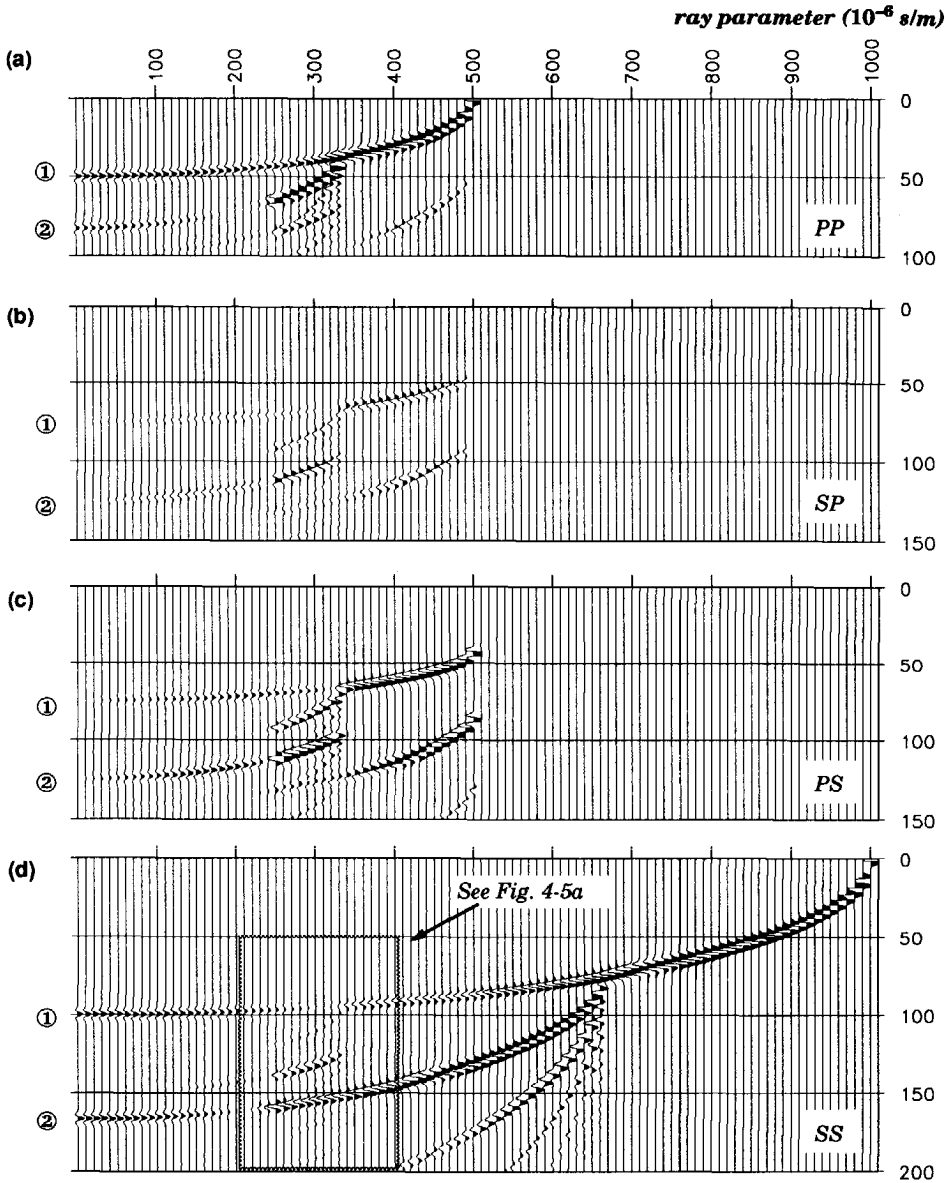


Fig. 4-4 Modeled p - τ gathers for the four different reflectivity types, PP, SP, PS and SS, where the first symbol indicates the receiver type and the second symbol indicates the source type. The elastic model is given by Table 4-1 and a 150Hz central frequency Ricker wavelet is used. There is no free surface; sources and receivers are located in the upper half-space. All gathers are plotted with the same scaling.

ing, a zero-phase Ricker wavelet with a central frequency of 150Hz is used, so that the individual events can be easily identified. The resulting p - τ gathers are shown in Fig. 4-4.

Besides the primary events, labeled ① and ②, all gathers exhibit strong events that have been converted more than one time (multiple conversions). Normal multiples are also present, most pronounced near the critical angles, where the primary reflections become very strong. At 250×10^{-6} s/m the P-waves in the lower half-space become evanescent. At 333×10^{-6} s/m the P-waves in the embedded layer become evanescent. Between these two ray parameters, the multiple conversions are very strong. At $p=1/\alpha_2 (=333 \times 10^{-6}$ s/m), these conversions cease to exist rather abruptly, because the P-waves in the layer become evanescent.

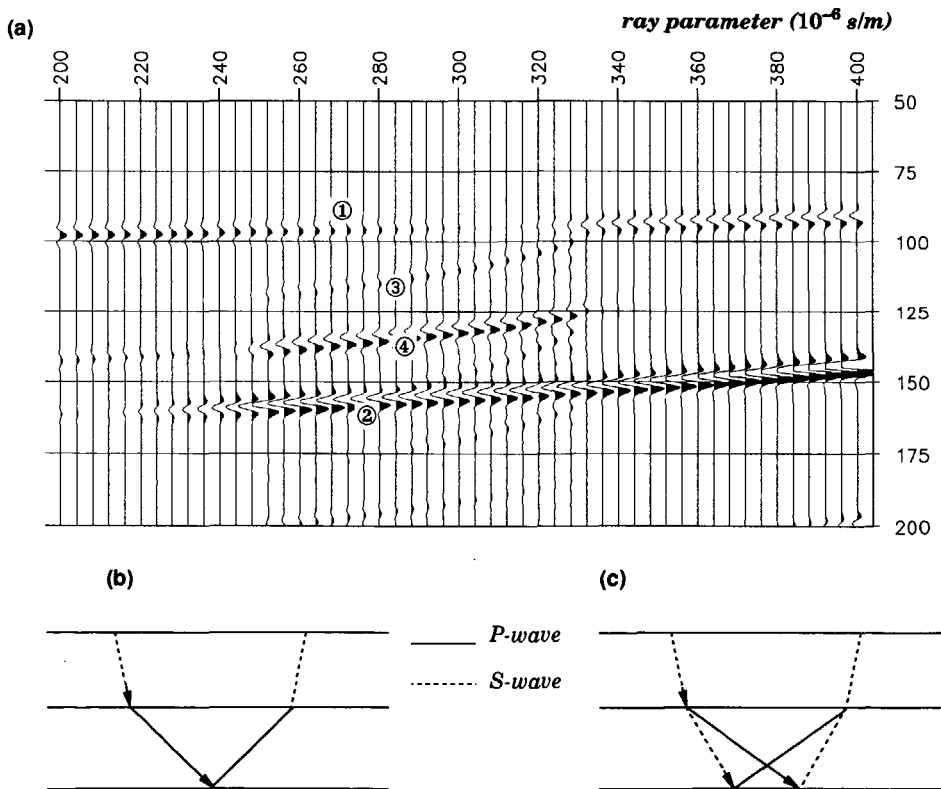


Fig. 4-5 (a) A closer look at the middle part of Fig. 4-4d, where the multiple conversions are most pronounced, e.g. events ③ and ④. Events ① and ② are the SS primaries. (b) The type of wave conversion that is associated with event ③. (c) The two types of wave conversion that are associated with event ④.

The p -values that are modeled are given by $(n-1)\Delta p$, $n=1,2,\dots,101$ with $\Delta p = 10 \times 10^{-6}$. Since neither $p=1/\alpha_2$ nor $p=1/\beta_2$ does belong to this set, the problem that was described in the previous section is not encountered.

Fig. 4-5 shows a closer look at the range of ray parameters, indicated by the gray box superimposed on Fig. 4-4d. It is obtained by a modeling with a ray parameter increment of 4×10^{-6} . Of two of the strongest multiple conversions (③ and ④), the ray paths are drawn in Fig. 4-5 b,c. Note that the amplitude of event ④ is as strong as that of the primary events. In the x - t domain, such multiple converted events will only be partly present in the (limited aperture) SS-gathers, because the P-waves propagate under very large angles when p approaches $1/\alpha$.

Event ④ is still visible in a few traces after $p=333 \times 10^{-6}$ s/m. This is due to the evanescent P-wave field in the embedded layer. In Fig. 4-6, the evanescent part of event ④, re-modeled with a small ray parameter increment, is shown in more detail. The wavelet broadening due to the frequency dependent damping of the evanescent waves is clearly visible.

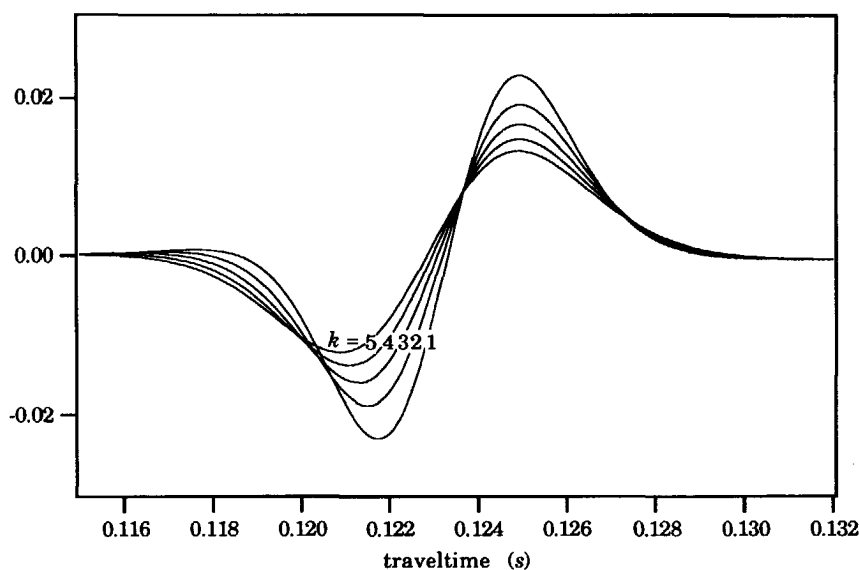


Fig. 4-6 The evanescent tail of event ④ of Fig. 4-5a for ray parameters $p=(333+k) \times 10^{-6}$ s/m with $k = 1, 2, \dots, 5$, just after the value $p=333.333 \times 10^{-6}$ s/m where the evanescent part commences.

Solving geophysical inverse problems by a data fitting approach, requires the minimization of an objective function, that is generally a nonlinear function of the model parameters. One of the problems that can occur is that the iterative minimization, based on the local derivatives of the objective function, ends up in a local minimum. Starting close enough to the actual global minimum (which is supposedly close to the true model) will often solve this problem. An alternative is the use of global optimization methods, based on Monte Carlo techniques, but these will not be considered here.

The second problem is that, around the global minimum, the objective function can be quite flat in one or more directions. These are the so-called ill-resolved directions. Mathematical stabilization is one way to improve the resolution of the inverse problem. Adding a constant value to the diagonal elements of a (forward) matrix that needs to be inverted is an example of such a stabilization. Incorporation of extra information—if available—can be considered a better method to stabilize inverse problems. Bayesian inversion is a methodology that combines the information in the data and the extra information in a statistically consistent manner.

5.1 Probability theory

In this section, the probabilistic concepts that underlie Bayesian inversion will be discussed. In the Bayesian interpretation, probability is seen as a degree of belief, which can either be objective (representing a “state of affairs”) or subjective (representing someone’s knowledge). The probability of an event can vary between zero and unity.

5.1.1 Cumulative distribution and probability density functions

The random variables that are considered in this thesis (model parameters and noise samples) can in principle assume every real value. The cumulative distribution function $F_X(x)$ of a continuous random variable X is defined by:

$$F_X(x) = \int_{-\infty}^x p(u) du = P(X \leq x), \quad (5-1)$$

where $P(A)$ denotes the probability of an event A . The function p is the probability density function (pdf) of X . Because of the properties of probability, it follows:

$$\begin{aligned} p(x) &\geq 0, \\ \int_{-\infty}^{\infty} p(x) dx &= 1. \end{aligned} \quad (5-2)$$

Definition (5-1) is easily extended for a set of n random variables. The *joint* distribution function and probability density functions are defined by:

$$\begin{aligned} F_X(\mathbf{x}) &= \int_{-\infty}^{x_1} du_1 \int_{-\infty}^{x_2} du_2 \cdots \int_{-\infty}^{x_n} du_n p(\mathbf{u}) \\ &= P(X_1 \leq x_1 \wedge X_2 \leq x_2 \wedge \dots \wedge X_n \leq x_n), \end{aligned} \quad (5-3)$$

with the vector \mathbf{X} being defined by $\mathbf{X} = (X_1, X_2, \dots, X_n)^t$ and likewise for the other vector quantities.

5.1.2 Mean and Covariance

The expectation of a (vector) function of a random (vector) variable is defined by:

$$E(\mathbf{f}(\mathbf{x})) = \int_X \mathbf{f}(\mathbf{x}) p(\mathbf{x}) d\mathbf{x}, \quad (5-4)$$

where the integration extends over the complete space of possible values for \mathbf{x} . The mean of a random variable is its expectation:

$$\bar{\mathbf{x}} = E(\mathbf{x}) = \int_X \mathbf{x} p(\mathbf{x}) d\mathbf{x}. \quad (5-5)$$

Another important quantity is the covariance:

$$\begin{aligned} C_{\mathbf{x}\mathbf{x}} &= E((\mathbf{x} - \bar{\mathbf{x}})(\mathbf{x} - \bar{\mathbf{x}})^t) \\ &= \int_X (\mathbf{x} - \bar{\mathbf{x}})(\mathbf{x} - \bar{\mathbf{x}})^t p(\mathbf{x}) d\mathbf{x}. \end{aligned} \quad (5-6)$$

The diagonal elements of the covariance matrix are the variances of the individual elements of \mathbf{x} . The square root of the variance is the standard deviation, denoted by σ .

5.1.3 Bayes' rule

The concepts of marginal and conditional pdf's play an important role in Bayesian inversion. Let the joint pdf of \mathbf{x} and \mathbf{y} be given by $p(\mathbf{x}, \mathbf{y})$. Assuming \mathbf{y} is an $m \times 1$ vector, the marginal pdf $p(\mathbf{x})$ is defined by:

$$\begin{aligned} p(\mathbf{x}) &= \int_{-\infty}^{\infty} dy_1 \int_{-\infty}^{\infty} dy_2 \cdots \int_{-\infty}^{\infty} dy_m p(\mathbf{x}, \mathbf{y}) \\ &= \int_Y p(\mathbf{x}, \mathbf{y}) d\mathbf{y}. \end{aligned} \quad (5-7)$$

It represents the probability density of \mathbf{x} alone, disregarding the variable \mathbf{y} . Two random variables \mathbf{x} and \mathbf{y} are called independent if their joint pdf is the product of the individual (marginal) pdf's:

$$p(\mathbf{x}, \mathbf{y}) = p(\mathbf{x})p(\mathbf{y}) \quad (5-8)$$

The conditional pdf $p(\mathbf{x} | \mathbf{y})$ represents the probability density of \mathbf{x} , given a certain value of the variable \mathbf{y} . It is defined by:

$$p(\mathbf{x} | \mathbf{y}) = \frac{p(\mathbf{x}, \mathbf{y})}{p(\mathbf{y})}. \quad (5-9)$$

Likewise, the conditional pdf $p(\mathbf{y} | \mathbf{x})$ is defined by:

$$p(\mathbf{y} | \mathbf{x}) = \frac{p(\mathbf{x}, \mathbf{y})}{p(\mathbf{x})}. \quad (5-10)$$

Combining (5-9) and (5-10), yields Bayes' rule:

$$p(\mathbf{x} | \mathbf{y}) = \frac{p(\mathbf{y} | \mathbf{x})p(\mathbf{x})}{p(\mathbf{y})}. \quad (5-11)$$

5.2 Bayes' rule and inversion

In Bayesian inversion, the random variables \mathbf{x} and \mathbf{y} in (5-11) represent model parameters and data respectively. Let $p(\mathbf{x}, \mathbf{y})$ reflect the "state of information" on parameters \mathbf{x} and data \mathbf{y} before measurements have been done. After the data \mathbf{y} has been obtained as a result of a measurement, the state of information on \mathbf{x} is represented by the conditional pdf $p(\mathbf{x} | \mathbf{y})$, the left-hand side of Bayes' rule (5-11).

The following interpretation of the elements on the right-hand side of (5-11) can be given: The conditional pdf $p(\mathbf{y} | \mathbf{x})$, usually called the likelihood function, represents the probability of the data \mathbf{y} , given the parameters \mathbf{x} . For its interpretation, it is convenient to assume that the data can be explained by:

$$y = g(x) + n, \quad (5-12)$$

where $g(x)$ is the forward model and n is the—additive—noise. The forward model $g(x)$ is determined by a set of *deterministic* physical relations that would describe the data in the absence of noise. Assuming x and n are independent, the following relation holds:

$$p(y|x) = p_n(y - g(x)), \quad (5-13)$$

where p_n is the pdf of the noise. It requires reasoning rather than mathematical manipulation to demonstrate the validity of (5-13). For the case of scalar random variables, Fig. 5-1 shows the conditional pdf's of the noise and data, given x . For a certain value of x , the conditional pdf of the noise is equal to $p_n(n|x)$, but since x and n are assumed to be independent, it follows:

$$p_n(n|x) = p(n, x)/p(x) = p_n(n) \quad (5-14)$$

because $p(n, x) = p_n(n)p(x)$. Since $y = g(x) + n$, it follows that, for a certain value of x , $p(y|x)$ is merely a shifted version of p_n , as is expressed by equation (5-12) and shown in Fig. 5-1.

The pdf $p(x)$ represents the state of knowledge on the model parameters, irrespective of the data. It is therefore called the *a priori* pdf. Geologic knowledge and data from well logs are important sources of prior information for geophysical inverse problems. It is generally sufficient to describe the prior information with the same generic model that is used for the data, i.e. relation (5-12), yielding:

$$x_p = g_p(x) + n_p. \quad (5-15)$$

Such a description includes simple prior information on the values of the parameters:

$$x_p = x + n_p, \quad (5-16)$$

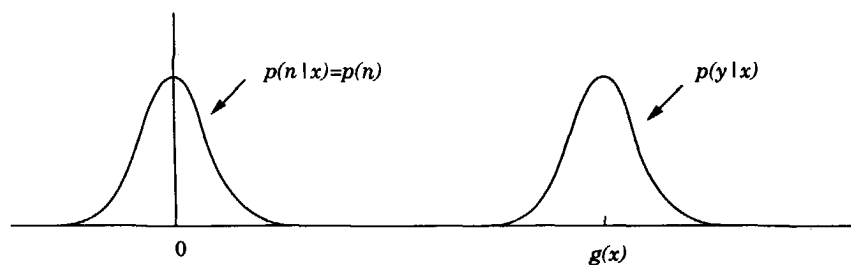


Fig. 5-1 Probability densities $p(n|x)$ and $p(y|x)$ for the case of independent parameter x and noise n .

where x_p are the prior values of the model parameters. But also relations *between* model parameters can conveniently be expressed with (5-15). The noise term is always used to express the degree of uncertainty in the prior relations.

Regarding the a posteriori pdf $p(\mathbf{x}|\mathbf{y})$ as a function of \mathbf{x} , the pdf $p(\mathbf{y})$ in the denominator of (5-11) is a constant factor that merely serves as a normalizing factor, i.e. it makes that the integral of $p(\mathbf{x}|\mathbf{y})$ over all \mathbf{x} evaluates to unity.

5.2.1 Estimators

As mentioned in the previous section, the pdf $p(\mathbf{x}|\mathbf{y})$ on the left of Bayes' rule (5-11) represents the total information about the parameters \mathbf{x} . It can be regarded as *the* solution to the inverse problem. However, for inverse problems with more than say, five parameters, it is impractical to evaluate and inspect the complete a posteriori pdf.

A more practical solution is to find a set of numbers which can be regarded as estimates of the parameters, a so-called point estimate. Ideally, an estimator $\hat{\mathbf{x}}$ should be unbiased, i.e. $E(\hat{\mathbf{x}} - \mathbf{x}) = 0$, so that

$$\int_{\mathbf{X}} (\hat{\mathbf{x}} - \mathbf{x}) p(\mathbf{x}|\mathbf{y}) d\mathbf{x} = 0. \quad (5-17)$$

Because $\hat{\mathbf{x}}$ is a constant with respect to the integration over \mathbf{x} , and since the integral over $p(\mathbf{x}|\mathbf{y})$ evaluates to unity, it follows:

$$\hat{\mathbf{x}} = \int_{\mathbf{X}} \mathbf{x} p(\mathbf{x}|\mathbf{y}) d\mathbf{x}, \quad (5-18)$$

which is the mean of the a posteriori pdf. This estimator is neither a practical solution, since it also requires an evaluation of the a posteriori pdf over the complete parameter space.

A more practical alternative is the MAP estimator, i.e. the set of parameters where the a posteriori pdf attains its maximum. If there is a unique point where this maximum (or mode) is reached, the pdf is called unimodal. If the a posteriori pdf is symmetric and unimodal, the mode and the mean coincide.

5.2.2 Gaussian statistics for noise and prior information

Sofar, no particular assumptions have been made regarding the characteristics of the involved pdf's. There are many reasons, however, to assume Gaussian pdf's, both for the noise and the prior information. Perhaps the most important reason is that Gaussian pdf's are mathematically most tractable. Fortunately, there are a number of other reasons to believe that the Gaussian pdf most accurately describes the uncertainty in data and prior information, see e.g. Duijndam (1988a) pp. 884-886.

For a Gaussian random variable \mathbf{z} with mean $\boldsymbol{\mu}$ and covariance \mathbf{C} , the pdf is given by:

$$p(\mathbf{z}) = \frac{1}{(2\pi)^{n/2} |\mathbf{C}|} \exp\left\{-\frac{1}{2}(\mathbf{z} - \boldsymbol{\mu})^t \mathbf{C}^{-1}(\mathbf{z} - \boldsymbol{\mu})\right\}, \quad (5-19)$$

where n is the number of elements of \mathbf{z} and $|\mathbf{C}|$ denotes the determinant of the covariance matrix. Assuming that the pdf of the noise \mathbf{n} on the data is Gaussian with zero mean and covariance \mathbf{C}_n , it follows with (5-13) that the likelihood function is given by:

$$p(\mathbf{y} = \mathbf{d} | \mathbf{x}) = \text{const.} \exp\left\{-\frac{1}{2}(\mathbf{d} - \mathbf{g}(\mathbf{x}))^t \mathbf{C}_n^{-1}(\mathbf{d} - \mathbf{g}(\mathbf{x}))\right\}. \quad (5-20)$$

Assuming that the noise \mathbf{n}_p on the prior relations (5-15) is also Gaussian distributed, with zero mean and covariance \mathbf{C}_p , the prior pdf is given by:

$$p(\mathbf{x}) = \text{const.} \exp\left\{-\frac{1}{2}(\mathbf{d}_p - \mathbf{g}_p(\mathbf{x}))^t \mathbf{C}_p^{-1}(\mathbf{d}_p - \mathbf{g}_p(\mathbf{x}))\right\}. \quad (5-21)$$

Apart from the normalizing term in the numerator of (5-11), the posterior pdf is given by the product of (5-20) and (5-21):

$$p(\mathbf{x} | \mathbf{y} = \mathbf{d}) = \text{const.} \times \exp\left\{-\frac{1}{2}(\mathbf{d} - \mathbf{g}(\mathbf{x}))^t \mathbf{C}_n^{-1}(\mathbf{d} - \mathbf{g}(\mathbf{x}))\right\} \times \\ \exp\left\{-\frac{1}{2}(\mathbf{d}_p - \mathbf{g}_p(\mathbf{x}))^t \mathbf{C}_p^{-1}(\mathbf{d}_p - \mathbf{g}_p(\mathbf{x}))\right\} \quad (5-22)$$

From this expression it is apparent that the information from the data and the prior information enters the posterior pdf in the same fashion.

Finding the maximum of a function is equivalent to finding the minimum of its logarithm. The MAP estimator $\hat{\mathbf{x}}$ that maximizes the posterior pdf is therefore equal to the point where the function $F(\mathbf{x})$ is minimum, with:

$$F(\mathbf{x}) = \frac{1}{2} \left\{ (\mathbf{d} - \mathbf{g}(\mathbf{x}))^t \mathbf{C}_n^{-1}(\mathbf{d} - \mathbf{g}(\mathbf{x})) + (\mathbf{d}_p - \mathbf{g}_p(\mathbf{x}))^t \mathbf{C}_p^{-1}(\mathbf{d}_p - \mathbf{g}_p(\mathbf{x})) \right\}. \quad (5-23)$$

Defining

$$\mathbf{e} = \begin{pmatrix} \mathbf{C}_n^{-1/2}(\mathbf{d} - \mathbf{g}(\mathbf{x})) \\ \mathbf{C}_p^{-1/2}(\mathbf{d}_p - \mathbf{g}_p(\mathbf{x})) \end{pmatrix}, \quad (5-24)$$

the expression for the objective function simplifies to:

$$F(\mathbf{x}) = \frac{1}{2} \mathbf{e}^t \mathbf{e}. \quad (5-25)$$

So, the inversion problem has been reduced to a (nonlinear) optimization problem. Various general purpose nonlinear optimization methods exist. They will be discussed in Section 5.3.

5.2.3 Result analysis

Once the minimum of the objective function has been found, it is important to assess its accuracy. Many types of result analysis exist, see Duijndam (1987) or Duijndam (1988b); the inspection of the a posteriori covariance being one of them. Although this matrix contains information about the correlation between the estimated parameters in its off-diagonal elements, it is often sufficient to consider only its diagonal elements. The square roots of the diagonal elements (the standard deviations) can be interpreted as error bars on the estimates.

In order to derive an expression for the a posteriori covariance, the objective function is expanded in a second order Taylor series:

$$F(\mathbf{x}) = F(\hat{\mathbf{x}}) + \mathbf{g}^t \Delta \mathbf{x} + \frac{1}{2} \Delta \mathbf{x}^t \mathbf{H} \Delta \mathbf{x}, \quad (5-26)$$

with $\Delta \mathbf{x} = \mathbf{x} - \hat{\mathbf{x}}$. The gradient \mathbf{g} and the Hessian \mathbf{H} are defined by respectively:

$$g_i = \frac{\partial F}{\partial x_i} \quad (5-27)$$

and

$$H_{ij} = \frac{\partial^2 F}{\partial x_i \partial x_j}. \quad (5-28)$$

If $\hat{\mathbf{x}}$ is the minimum of the objective function, the gradient must be zero, yielding:

$$F(\mathbf{x}) \approx F(\hat{\mathbf{x}}) + \frac{1}{2} \Delta \mathbf{x}^t \mathbf{H} \Delta \mathbf{x}. \quad (5-29)$$

Making use of the fact that the objective function is the negative logarithm of the a posteriori pdf yields:

$$p(\mathbf{x}|\mathbf{y}) \approx \text{const.} \exp\left\{\frac{1}{2}(\mathbf{x} - \hat{\mathbf{x}})^t \mathbf{H}(\mathbf{x} - \hat{\mathbf{x}})\right\}, \quad (5-30)$$

which means that the a posteriori pdf is Gaussian with mean $\hat{\mathbf{x}}$ and covariance \mathbf{H}^{-1} . This result depends heavily on the accuracy of (5-29) over the part of the parameter space where the exact a posteriori pdf is not negligible. The matrix \mathbf{H}^{-1} is still useful when this condition is not satisfied, since it contains information about the local behavior of the objective function around its minimum. Only when the forward model $\mathbf{g}(\mathbf{x})$ is linear, expression (5-30) is exact.

An inverse problem is called ill-resolved when the objective function is practically constant in one or more directions around its minimum. This is the case when the Hessian is nearly singular. The *ill-resolved* directions are given by the eigenvectors of the Hessian that correspond to eigenvalues that are close to zero. Note that all eigenvalues are greater than or equal to zero, since the Hessian is a positive semi-definite matrix. *Unresolved* directions correspond to eigenvectors whose eigenvalues are exactly zero.

It will be shown in Section 5.3.2 that the Hessian can be approximated if $F(\mathbf{x})$ is a sum of squares:

$$\mathbf{H} \approx \mathbf{J}^t \mathbf{J}, \quad J_{ij} = \frac{\partial e_i}{\partial x_j}, \quad (5-31)$$

where \mathbf{J} is the Jacobian matrix. The eigenvalue decomposition of the Hessian can then be replaced by a singular value decomposition of the Jacobian matrix. For a more extensive discussion, the reader is referred to Duijndam (1987).

5.3 Nonlinear optimization

Nonlinear optimization methods are designed to find the minimum or maximum of a multivariate objective function $F(\mathbf{x})$. Since minimizing $F(\mathbf{x})$ is equivalent to maximizing $-F(\mathbf{x})$, only minimization will be discussed from now on. For the inversion problem, $F(\mathbf{x})$ is a sum of squares, which can be seen as a special case of the general problem. As will appear later, special methods for minimizing a sum of squares exist.

The minimization methods that will be discussed here are based on the *local* derivatives of the objective function. As such, they are able to find a local extreme. For a extensive overview of this type of optimization methods, the reader is referred to Gill, Murray and Wright (1981). Global optimization methods, often based on Monte Carlo techniques, will not be considered here.

5.3.1 General methods

In the minimization methods that will be discussed here, the parameters \mathbf{x} are iteratively updated until certain convergence criteria are met:

$$\mathbf{x}_{k+1} = \mathbf{x}_k + \alpha_k \mathbf{p}_k, \quad (5-32)$$

where \mathbf{p}_k is the direction of the update and α_k is the step length. In most methods, the step length is not fixed. Given a search direction \mathbf{p}_k , it is determined such that it approximately minimizes F on the line $\mathbf{x}_k + \alpha_k \mathbf{p}_k$.

The simplest minimization methods use only first order derivatives, i.e. the gradient of the objective function, defined in (5-27). In the steepest descent method, the

search direction is simply opposite to the gradient, $\mathbf{p} = -\mathbf{g}$. The conjugate gradient method is a modification to the steepest descent method, in order to obtain a faster convergence. Since these methods do not use second derivatives of the objective function, they are suitable for problems with a large number of parameters like the 2D gridded inversion methods that were discussed in Section 1.4. For a small sized grid of 100×100 , the number of elastic parameters (three per grid point) is already $N=30,000$ so that the Hessian matrix of second derivatives would contain $N^2=0.9 \times 10^9$ elements. Besides the ungainly amount of computation time that would be required, the Hessian would not even fit in current supercomputer memories.

Newton methods employ the second derivatives and, consequently, have a better convergence rate than gradient methods. Around a certain point \mathbf{x}_0 , the second order Taylor expansion of the objective function is given by:

$$F(\mathbf{x}_0 + \Delta\mathbf{x}) = F(\mathbf{x}_0) + \mathbf{g}^t \Delta\mathbf{x} + \frac{1}{2} \Delta\mathbf{x}^t \mathbf{H} \Delta\mathbf{x}. \quad (5-33)$$

The minimum of this expression with respect to $\Delta\mathbf{x}$ is given by:

$$\Delta\mathbf{x} = \mathbf{H}^{-1} \mathbf{g}. \quad (5-34)$$

Hence, for Newton methods, the search direction is given by $\mathbf{p} = \mathbf{H}^{-1} \mathbf{g}$. Obviously, this involves the inversion of the Hessian matrix, so that Newton methods can not be employed for problems with a large number of parameters.

In so-called Quasi-Newton methods, the Hessian is not really calculated but rather approximated. In each iteration, new information about the curvature of the objective function becomes available, which is used to update the approximation of the Hessian. Since Quasi-Newton methods do not require the actual calculation of the second derivatives, they are often more efficient than true Newton methods.

5.3.2 Methods for the minimization of a sum of squares

Specially designed minimization algorithms are available for the case that the objective function is a sum of squares:

$$F(\mathbf{x}) = \frac{1}{2} |\mathbf{e}(\mathbf{x})|^2 \quad (5-35)$$

In that case, the gradient is given by:

$$\begin{aligned} \mathbf{g} &= \mathbf{J}^t \mathbf{e}, \\ \text{with } J_{ij} &= \frac{\partial e_i}{\partial x_j}, \end{aligned} \quad (5-36)$$

where \mathbf{J} is called the Jacobian matrix. With some straightforward algebra, it can be shown that the Hessian matrix is given by:

$$\mathbf{H} = \mathbf{J}^t \mathbf{J} + \mathbf{Q},$$

$$\text{with } \mathbf{Q} = \sum_{i=1}^M e_i \mathbf{G}_i \text{ and } \mathbf{G}_i = \frac{\partial^2 e_i}{\partial \mathbf{x}^2}.$$
(5-37)

In the Gauss-Newton method, the \mathbf{Q} term is neglected, so that the Hessian is approximated with $\mathbf{J}^t \mathbf{J}$, yielding the following search direction:

$$\mathbf{p} = (\mathbf{J}^t \mathbf{J})^{-1} \mathbf{J}^t \mathbf{e}.$$
(5-38)

This means that only the Jacobian matrix of first order derivatives of the residuals is needed which usually represents a large reduction in the amount of computations. Assuming a well-conditioned Jacobian, the Gauss-Newton approximation is accurate if the elements of \mathbf{Q} matrix are small compared to those of $\mathbf{J}^t \mathbf{J}$, which is the case when either:

- 1) The dependence of the residuals on the parameters \mathbf{x} is sufficiently linear so that the matrices \mathbf{G}_i will be small.
- 2) The residuals themselves are small

However, when $\mathbf{J}^t \mathbf{J}$ becomes close to singular in some point of the parameter space, (5-38) will become unstable. The often encountered Levenberg-Marquard method employs the following search direction

$$\mathbf{p} = (\mathbf{J}^t \mathbf{J} + \lambda \mathbf{I})^{-1} \mathbf{J}^t \mathbf{e},$$
(5-39)

where λ is adjusted after each iteration, depending on the reduction of the objective function that was achieved. In the Levenberg-Marquard method, the step length α_k in (5-32) is always unity.

Methods that incorporate a \mathbf{Q} term, either exact or approximated, are called corrected Gauss-Newton methods, see Section 4.7.5 of Gill, Murray and Wright (1981). They can be considered superior to the Levenberg-Marquard method.

5.3.3 Application to the elastic inverse problem

Because the number of parameters for the elastic inversion that is discussed in this thesis is quite small, fast Newton methods can be used. A corrected Gauss-Newton algorithm was chosen, because it can be expected to perform best under all conditions. The algorithm, E04ECF from the NAG library, only requires a user-supplied subroutine that returns the values of the residuals \mathbf{e} as a function of \mathbf{x} . The first derivatives of the residuals need not be supplied; they are calculated with finite differences. Besides a good deal of bookkeeping, the coding of the inversion scheme is hereby effectively reduced to the coding the forward model, i.e. the recursive reflectivity algorithm.

For N parameters, the calculation of the Jacobian matrix with finite differences requires $N+1$ forward modeling steps. Since the forward modeling is fast and the number of parameters is relatively small (say, $N < 50$) this is acceptable. It should be possible, however, to calculate the derivatives of the p - τ data with respect to the layer parameters directly.

One way to do so is suggested by Pan et al. (1990). In this paper, a target oriented elastic inversion of PP p - τ data is described. Without supplying any specifics, it is mentioned that the model perturbation in the iterative inversion is the "gradient-based back projection of the residual traces". Apparently, Pan et al. are referring to the adjoint-state technique that was discussed in Section 1.4.1. Although it is unclear to this author how this technique can be applied in case of a model-based parametrization (the layer thickness is a parameter), it would speed up the inversion considerably.

The derivatives may also be calculated by some procedure that operates in conjunction with the recursive reflectivity calculation, involving the derivatives of the local scattering coefficients with respect to the layer parameters. Both methods have not been further investigated.

6.1 Introduction

In the previous chapters, the majority of the components of the elastic inversion method have been discussed. To briefly name them:

- 1) Local parametrization (per lateral position) of the target zone with a (small) number of homogeneous layers with varying thickness.
- 2) The input data are gathers in the p - τ domain and result from the redatuming procedure of the DELPHI scheme. These gathers have sources and receivers for pure P- and S-wave potentials. Any combination of the four reflectivity types PP, SP, PS and SS can be used.
- 3) The inversion makes use of the Bayesian principle to combine data and prior information. The forward model for the data is based on the recursive reflectivity algorithm that was described in Section 4.3.
- 4) Assuming a Gaussian distribution of the noise on the data and the prior relations, the parameter estimates are found by minimizing the sum of squares of the mismatch terms. This is done by employing a corrected Gauss-Newton optimization algorithm, see Section 5.3.3.
- 5) Moving along the target, the inversion is performed *per* lateral position. Subsequently, the individual solutions are integrated to yield a 2D (or 3D) model of the laterally varying target zone.

The prior information that will be used is an important aspect of the inversion algorithm and will be discussed in Section 6.3. In order to explain why prior information is needed, a discussion of some non-uniqueness aspects of the elastic inverse problem is appropriate. This will be done in the next section.

Some extra robustness parameters will be introduced in Section 6.4, which account for inaccuracies in the redatuming procedure. An important alternative parametrization using lithological properties and prior information will be introduced in

Section 6.5. This parametrization effectively lumps the elastic and lithologic inversion modules of the DELPHI scheme (see Fig. 2-1) together.

6.1.1 Elastic parametrization

In the actual inversion program, a choice can be made between different parametrizations:

- α , β and ρ
- α , σ and ρ , where σ is Poisson's ratio, defined in equation (6-6a).
- Z_p , Z_s and ρ , where $Z_p = \rho\alpha$ is the acoustic impedance and $Z_s = \rho\beta$ is the shear impedance.
- λ , μ (the Lamé parameters) and ρ

Based on average results from a number of tests, all of the above parametrizations performed equally well in terms of convergence rate and accuracy of the solution. The option to choose different parametrizations was implemented for purely numerical reasons. The choice of parametrization has no effect on the way the results are presented to the user (usually α , β , ρ and σ). Neither does it effect the types of prior information that can be specified. E.g. when using a parametrization in terms of α , β and ρ , it is still possible to specify prior information on the Poisson's ratio because of the general form of prior relations (5-15).

6.1.2 Wavelet and initial model

The full-waveform inversion requires that the wavelet is available. The adaptive multiple elimination procedure of the DELPHI scheme (Verschuur 1991) is able to estimate the source wavelet at the surface. To obtain the effective wavelet at the target level, some filter may be applied to account for absorption and stratigraphic filtering.

Since the targetzone at one midpoint position is parametrized by a fixed number of layers, an initial model, that minimally specifies this number is required. If a well log is present, blocking the log will provide the number of layers in the vicinity of the well. The wavelet at the target level can now be refined by an estimation procedure that optimally matches the blocky log to a few seismic traces around the well, see Duijndam (1987). This procedure also involves small updates of the initial log model.

Therefore, close to the well the number of layers and the wavelet can be obtained. To keep track of the stratigraphy and the wavelet when moving away from the well, it is sufficient to use a poststack inversion procedure. In such a method, the forward model for a seismic trace on a poststack section is assumed to be a 1D convolution of the wavelet and a spiky reflectivity series:

$$\begin{aligned}
 s(t) &= w(t) * r(t) \\
 &= \sum r_i w(t - \tau_i).
 \end{aligned}
 \tag{6-1}$$

Given the wavelet and the seismic trace, one can then invert for the reflection coefficients r_i and the lagtimes τ_i . If prior information about the acoustic impedance level is available, one can invert for lagtimes and acoustic impedances. With the necessary modifications, this procedure can also be applied to stacked SS data and even to stacked converted gathers.

When performing such a trace inversion, chances are that when moving away from the well, the residuals grow. As Duijndam describes, this can be due to a changing wavelet (overall higher residuals) or a change in the number of layers (localized residuals). In the first case the wavelet is re-estimated, using essentially the same procedure that was used at the well. In the second case, one has to change the number of layers in the parametrization.

Besides the wavelet and the number of layers in the parametrization, the post-stack inversion can supply an initial model for the prestack elastic inversion, as is illustrated in Fig. 6-1. In order to avoid ending up in a local minimum, it is important that the initial model is in some sense close to the true model. One requirement is that the error in the initial traveltimes (for the used reflectivity types) is smaller than the peak to trough distance of the wavelet. Fortunately, the traveltimes can very reliably be estimated from the poststack data. Violating this condition will usually drive the inversion into a local minimum. The inversion is less sensitive to the initial values of the medium parameters, although it is preferable to take care that the initial reflectivity has at least the same sign as the observed reflectivity.

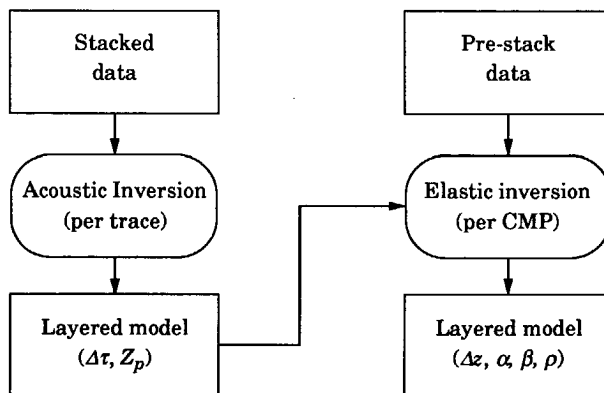


Fig. 6-1 A poststack stratigraphic inversion of stacked PP data yields a layered model in terms of time thickness and acoustic impedance. This model can serve as an initial model for the prestack elastic stratigraphic inversion.

6.2 Non-uniqueness aspects of the elastic inverse problem

The p - τ gathers that are used in the inversion, contain both amplitude and travel-time information. For thin layers, however, the reflections of successive boundaries will interfere, so that the amplitudes and traveltimes of the individual events cannot readily be obtained. This has been the main reason to choose for a full-waveform inversion scheme rather than using picked amplitudes and assuming they represent the actual reflectivity functions.

Besides the information about the velocities that is present in the moveout behavior of the reflections, the angle dependent amplitudes should largely contain the information that is necessary to resolve the elastic parameters. Transmission through interfaces is also angle dependent, but the relative amplitude change with angle is generally much smaller for transmission than for reflection. The properties of the reflectivity functions of the single boundary can therefore to some extent predict what can be expected from inversion for multiple layers.

6.2.1 An analysis using the approximated reflectivity functions

Studying the approximations to the reflection coefficients that were given in Section 3.6.2 reveals some aspects of non-uniqueness of the elastic inverse problem. Using $\sin \bar{\phi} \approx p\bar{\alpha}$ in the approximation of the PP reflectivity (3-57a) and rearranging terms, yields:

$$R_{pp}(p) \approx \frac{1}{2} \frac{\Delta \rho}{\bar{\rho}} - 2\bar{\beta}^2 \left(\frac{\Delta \rho}{\bar{\rho}} + 2 \frac{\Delta \beta}{\bar{\beta}} \right) p^2 + \frac{1}{2(1-p^2\bar{\alpha}^2)} \frac{\Delta \alpha}{\bar{\alpha}}. \quad (6-2)$$

As was discussed in Section 3.6.1, the exact p dependent reflectivity is determined by five parameters; the four velocities ($\alpha_u, \alpha_l, \beta_u, \beta_l$) and the density ratio (ρ_u/ρ_l). With (3-56), it follows that these five parameters are uniquely related to

$$\mathbf{x} = \left(\Delta \alpha, \bar{\alpha}, \Delta \beta, \bar{\beta}, \frac{\Delta \rho}{\bar{\rho}} \right)^t, \quad (6-3)$$

so that (6-3) is an equivalent parametrization.

In order to determine if the five parameters of (6-3) can in principle be estimated, it is assumed that (6-2) is the forward model and that noise-free measurements for at least five different p values are available. Since the three terms of (6-2), regarded as functions of p , are linearly independent, it can be seen that the following holds:

- 1) $\Delta \rho / \bar{\rho}$ can be determined.
- 2) The multiplier of the p^2 term can be determined, leaving one degree of freedom for $\Delta \beta$ and $\bar{\beta}$.

- 3) From the third term, both $\Delta\alpha$ and $\bar{\alpha}$ can be obtained.

The important result is that there is an unresolved direction for $\Delta\beta$ and $\bar{\beta}$, or equivalently, for β_u and β_l .

Assuming small angles so that $1/(1 - \bar{\alpha}^2 p^2) \approx 1 + \bar{\alpha}^2 p^2$, transforms (6-2) into:

$$R_{pp}(p) \approx \frac{1}{2} \left(\frac{\Delta\rho}{\bar{\rho}} + \frac{\Delta\alpha}{\bar{\alpha}} \right) + \left\{ \frac{1}{2} \bar{\alpha} \Delta\alpha - 2\bar{\beta}^2 \left(\frac{\Delta\rho}{\bar{\rho}} + 2\frac{\Delta\beta}{\bar{\beta}} \right) \right\} p^2 \quad (6-4)$$

Now, only the normal-incidence term and the multiplier of the p^2 term can be determined, leaving three completely unresolved directions for the five parameters to be estimated. Observe that these normal incidence and "gradient" terms (actually of $\sin^2 \bar{\phi}$ instead of p^2) are precisely the ones that are commonly used in conventional, linearized AVO inversion of NMO corrected CMP gathers (weighted stacking).

It should be noted, though, that the above results are based on approximations to the true reflectivity. Especially for large S-wave contrasts, the conditioning of the inverse problem (based on the exact expressions) improves considerably so that the S-wave velocities *can* be estimated. But in general, assuming some noise on the data, it will be difficult to accurately estimate all five parameters solely from the PP reflectivity of a single boundary.

In order to get an insight in the behavior of the multi-layer case, assume that the maximum incident angle is quite large, so that (6-3) needs to be used. As was mentioned, there is one completely unresolved direction for the S-wave velocities β_u and β_l . For the case of N boundaries, there are *not* N unresolved directions, but still only one! This can be concluded from the following reasoning:

- 1) Suppose β_1 is known. Consequently, β_2 is determined through the reflectivity of boundary #1.
- 2) With β_2 determined, β_3 follows from the reflectivity of boundary #2.
- 3) And so on.

Equivalently, supplying the average of all β_i 's would also suffice to determine all β_i 's. Note that this average is in fact a macro parameter and is as such available (from traveltimes information).

A similar analysis can be applied to the other three reflectivity types. In all cases it follows that there will be some unresolved directions when considering each reflectivity type individually. Combining data of different reflectivity types in a simultaneous inversion will remove the unresolved directions. Because of the fact that the SS approximation is of the same form as the PP approximation, it can be

seen that the S-wave velocities can be determined from approximation (3-57d) for the SS reflectivity. Combining PP and SS data would therefore remove the unresolved directions.

6.2.2 Angle vs. ray parameter

At this point it is worthwhile to make a small side-step and consider conventional, linearized AVO inversion (weighted stacking). In this technique, see Section 1.3, an approximated reflectivity function as a function of the incident *angle* is fitted to the aligned reflectivity in NMO corrected CMP gathers. Basically, this reflectivity function is given by approximation (3-59):

$$r_{pp}(\bar{\phi}) = \frac{1}{2} \left(\frac{\Delta\rho}{\bar{\rho}} + \frac{\Delta\alpha}{\bar{\alpha}} \right) - 2 \frac{\bar{\beta}^2}{\bar{\alpha}^2} \left(\frac{\Delta\rho}{\bar{\rho}} + 2 \frac{\Delta\beta}{\bar{\beta}} \right) \sin^2 \bar{\phi} + \frac{1}{2} \frac{\Delta\alpha}{\bar{\alpha}} \tan^2 \bar{\phi} \quad (6-5)$$

Some authors, e.g. Smith and Gidlow (1987), introduce linearized empirical relations ($\Delta\rho/\bar{\rho} = \frac{1}{4} \Delta\alpha/\bar{\alpha}$) to make the inversion more stable, but this is not relevant to the issue that is discussed here.

In order to obtain the incident angle field $\bar{\phi}$, ray tracing in a smooth, macro velocity model is applied. On a detailed level, these angles will be inaccurate, since, especially at the far offsets, the incident angle can vary considerably (increase, decrease) from reflector to reflector, depending on the *detailed* (thin layer) velocities. This effect is compensated somewhat for, because, as expressed in (3-58), the angle $\bar{\phi}$ is actually the average of the incident and refracted angles. The ray parameters, on the other hand, will gradually increase with depth and depend only slightly on detailed velocity variations.

By introducing the angles, however, one loses information in the sense that the *absolute* velocities cannot be estimated anymore. This can readily be seen from equation (6-5) where besides the global $\bar{\beta}/\bar{\alpha}$ model (which is an input parameter), only the relative contrasts are present. In the previous section, it was demonstrated that from the corresponding p -dependent reflectivity function (6-2), the absolute velocities *can* be estimated. So by introducing information (the angles) that is actually not available, one loses the ability to estimate the absolute velocities. A practical reason for using the angle dependent reflectivity (6-5) instead of the p dependent reflectivity (6-2) is that the former one is indeed linear in the three relative parameter contrasts, whereas the latter one is nonlinear in the five parameters (6-3).

6.2.3 Small offsets

If data is only available up to a relatively small ray parameter, the reflectivity will show little variation. In such a case, it is certainly not possible to accurately estimate the elastic parameters independently. For the case of solely PP or SS reflectivity, this means that the normal incidence reflectivity is the only well-resolved

parameter. Consequently, only the relative contrasts of the acoustic impedance $Z_p = \rho\alpha$ (for PP only) or the shear impedance $Z_s = \rho\beta$ (for SS only) can accurately be estimated.

Given the availability of accurate prior information about the targetzone average of the impedance, this means that also the impedances of the individual layers are resolved. If Both PP and SS data are available, this implies that also the ratio of the impedances is well resolved. Since $z_s/z_p = \beta/\alpha$, also the ratio of S-wave to P-wave velocity is resolved. This ratio is sensitive to the pore fill of the porous rock, and is therefore of practical importance. The often encountered Poisson's ratio σ is uniquely related to β/α by:

$$\sigma = \frac{\frac{1}{2} - (\beta/\alpha)^2}{1 - (\beta/\alpha)^2}, \quad (6-6a)$$

$$\frac{\beta}{\alpha} = \sqrt{\frac{\frac{1}{2} - \sigma}{1 - \sigma}}. \quad (6-6b)$$

So Poisson's ratio can in principle be determined from small offset PP and SS measurements. This is only the case, if indeed information about the absolute values of the impedances is a priori available.

An even more reliable source of information about β/α , or equivalently Poisson's ratio, is present in the traveltimes. It is known from research on target oriented poststack acoustic impedance inversion (Duijndam 1987), that the traveltimes are better resolved than the impedances (derived from the reflection amplitudes). Even for events with strong interference, the traveltimes remain well resolved. Also in the prestack situation, it can be expected that the traveltimes are well determined. Assume that for a certain layer, the normal-incidence traveltimes are given by $\Delta\tau_{pp}$ and $\Delta\tau_{ss}$ for PP and SS data respectively. For that layer, the ratio of β over α is then given by:

$$\frac{\beta}{\alpha} = \frac{\Delta\tau_{pp}}{\Delta\tau_{ss}}. \quad (6-7)$$

6.2.4 Contour plots

In Section 6.2.1, an unresolved direction for the S-wave velocities was found to exist when using only PP data, based on approximation (6-2) for the PP reflectivity. It is interesting to investigate the behavior if the exact reflectivity function is used. This can be done by studying contour plots of a suitably chosen objective function.

Consider Fig. 6-2a where the elastic parameters of a two-layer elastic model are given. The real and the imaginary parts of the corresponding PP reflectivity are

shown as a function of the ray parameter in Fig. 6-2b. Let the function $F(\mathbf{x})$ be defined by:

$$F(\mathbf{x}) = \frac{1}{2} |e|^2, \quad (6-8)$$

with $e_i = R_{pp}(p_i; \mathbf{x}_{true}) - R_{pp}(p_i; \mathbf{x})$,

where R_{pp} denotes the exact PP reflectivity and $\mathbf{x} = (\alpha_u, \alpha_l, \beta_u, \beta_l, \rho_u, \rho_l)$ denotes a perturbed version of the actual medium parameters \mathbf{x}_{true} . Using ray parameters on the interval $[0, 392 \times 10^{-6} \text{ s/m}]$, a contour plot of (a normalized) $F(\mathbf{x})$ in the (β_u, β_l) subspace is shown in Fig. 6-3a for the whole range of possible values of β_u and β_l . Note that the axes of the contour plot correspond to the ratio of S-wave to P-wave velocity, rather than the absolute value of the S-wave velocity. The P-wave velocities and the densities are kept on their true values. The maximum ray parameter that is used corresponds to an incident angle of 70° , which is well into the postcritical regime.

As can be seen, there is not a well defined minimum, but rather an elongated valley with very low values of the function F . The actual values of the S-wave velocities (indicated by the cross) lie of course within this valley. The value of $F(\mathbf{x})$ is nonzero everywhere except at the true model. This is shown in Fig. 6-3b where the logarithm of F at the "bottom of the valley" (the dotted line), is plotted. The exact value of the minimum was obtained by a univariate optimization in the β_l direction for all β_u values.

So, there is an *ill-resolved* direction for the S-wave velocities, rather than an *unresolved* direction, as was predicted in the previous section. This would also have been the case if only precritical ray parameters had been used. The difference between un- and ill-resolved is merely of theoretical importance; for practical purposes, all elastic models on the dotted line of Fig. 6-3a will have an effectively equal PP reflectivity.

(a)

| Parm. | Upper | Lower |
|----------------|-------|-------|
| α (m/s) | 2400 | 1600 |
| β (m/s) | 3000 | 1500 |
| ρ gr/cc | 2.34 | 2.60 |
| σ | 0.1 | 0.333 |

(b)

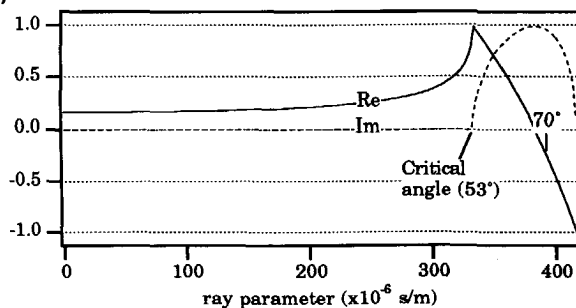


Fig. 6-2 (a) Elastic parameters of a two-layer elastic model. The values are typically those of a gas sand over a water sand. (b) Corresponding exact PP reflectivity for ray parameters up to $1/\alpha_u$. Both real and imaginary parts are plotted.

6.3 Prior information for elastic stratigraphic inversion

As was discussed in Section 6.2, the elastic inverse problem is generally ill-resolved. This is especially true when only one type of reflectivity can be used. Multi-component acquisition is not performed on a routine basis, so that in general, only pseudo PP data is available. When layers are thin, the reflections will interfere, which further decreases the resolution of the inverse problem.

The discussion of non-uniqueness aspects of the elastic inversion has clearly demonstrated that there is a need for extra information. When specifying the type of prior information and the corresponding uncertainty (as expressed by the prior covariance matrix), the following rules should be minded:

- 1) Use prior information that is available in practice.
- 2) Use realistic values for the uncertainty of the prior relations.
- 3) Use types of information that can be expected to "repair" the ill-resolved directions. It is not necessary to specify prior information on parameters that are already well-resolved.

Based on these rules, prior information on the targetzone averages of the elastic parameters and empirical relations *between* the elastic parameters are used. The

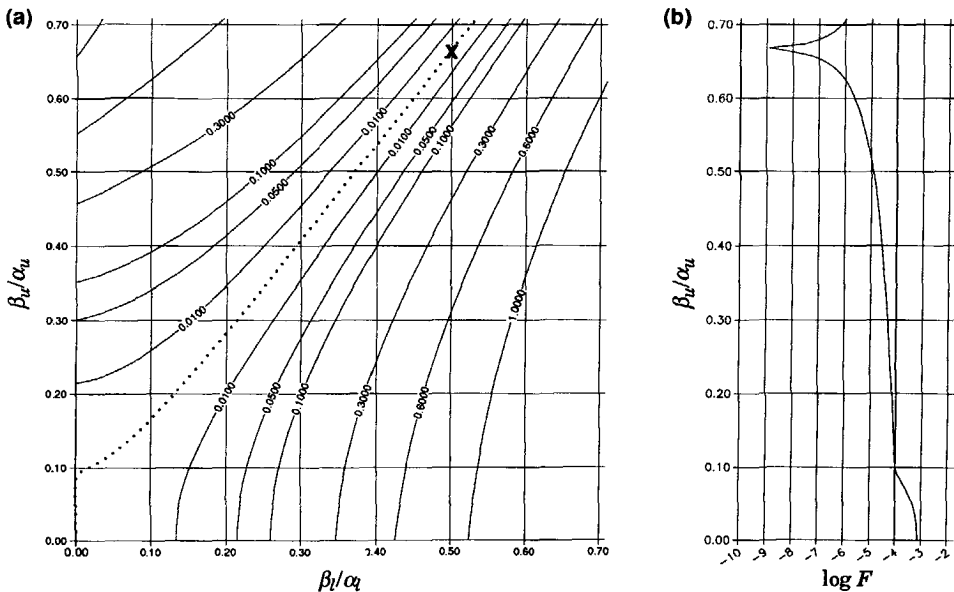


Fig. 6-3 (a) Contour plot of the objective function $F(x)$ of (6-8). The dotted line shows exactly where F is lowest. (b) Logarithm of $F(x)$ at the "bottom of the valley" where F is lowest.

noise terms on all prior relations that will be used are supposed to be statistically independent, so that the prior covariance matrix C_p is diagonal.

6.3.1 Targetzone averages of the elastic parameters

Rather than specifying prior information on the individual layer parameters, only information about their targetzone averages is supplied. Averages for P-wave velocity, density and Poisson's ratio are used. Poisson's ratio is chosen instead of the S-wave velocity because in general, more information about the ratio β/α is available than about the absolute value of β .

To be explicit, for e.g. the P-wave velocity, the following mismatch term is used:

$$\left\{ \langle \alpha \rangle_p - \frac{1}{N} \sum_{i=1}^N \alpha_i \right\} / \sigma_\alpha, \quad (6-9)$$

where N is the number of layers in the targetzone and $\langle \alpha \rangle_p$ is the prior value for the average P-wave velocity. The standard deviation σ_α expresses the uncertainty of the average P-wave velocity. This is just one of the terms that constitute the prior part of the residual vector e of equation (5-24). Because the targetzone has a considerable thickness, the $\langle \alpha \rangle_p$ that has to be supplied is in fact a macro parameter and can be obtained from a macro model that was previously derived from traveltimes information.

The average Poisson's ratio $\langle \sigma \rangle_p$ can also be obtained from traveltimes information. If both PP and SS data are available, it can be obtained from the ratio of the PP and SS traveltimes through the macro layer that contains the targetzone. If converted data (SP or PS) is available, the average Poisson's ratio can be obtained from the moveout behavior. If only PP data are available, one can use an empirical value for $\langle \sigma \rangle_p$, depending a.o. on the depth of the targetzone. Naturally, information from well logs can also be used; this applies for all averages.

The average value for the density cannot be obtained from seismic information. An empirical value needs to be used. Since the average density is a completely unresolved parameter, the average of the estimated densities will be practically equal to the specified value.

6.3.2 Empirical relations

The non-uniqueness of the elastic inversion can substantially be reduced by introducing relations *between* the elastic parameters. There are general, empirically based relations between the elastic parameters, that hold for a reasonably broad class of rocks. Two of these so-called empirical relations are used.

The Gardner relation between P-wave velocity and density is given by:

$$\alpha = c\rho^\varepsilon. \quad (6-10)$$

When measuring the velocity in m/s and the density in kg/m^3 , typical values for the constants (except for coal, salt and anhydrites) are $c=1.08 \times 10^{-10}$ and $\varepsilon=4$, see Sheriff and Geldart (1983). For these values, Fig. 6-4a shows a graph of the P-wave velocity as a function of the density.

In Castagna et al. (1985), a linear relation between the P-wave and S-wave velocity is proposed; the so-called mudrock line:

$$\alpha = a + b\beta. \quad (6-11)$$

When measuring both velocities in m/s, typical values for the constants are $a=1360$ and $b=1.16$ for water-saturated elastic silicate rocks. The corresponding graph of the P-wave velocity as a function of the S-wave velocity is given in Fig. 6-4b.

If a database of well-log data is available for the region of interest, better values for the constants of the empirical relations may be obtained through a data-fitting procedure. If prior to the elastic inversion, the lithotypes of the target layers can be given, the empirical constants may be determined per lithotype. A better procedure, however, is to include specific lithological information as prior information. This will be discussed in Section 6.5. For every layer i of the target zone, the Gardner and Mudrock relations each yield a residual term:

$$(\alpha_i - c\rho_i^\varepsilon) / \sigma_{gar}, \quad (6-12a)$$

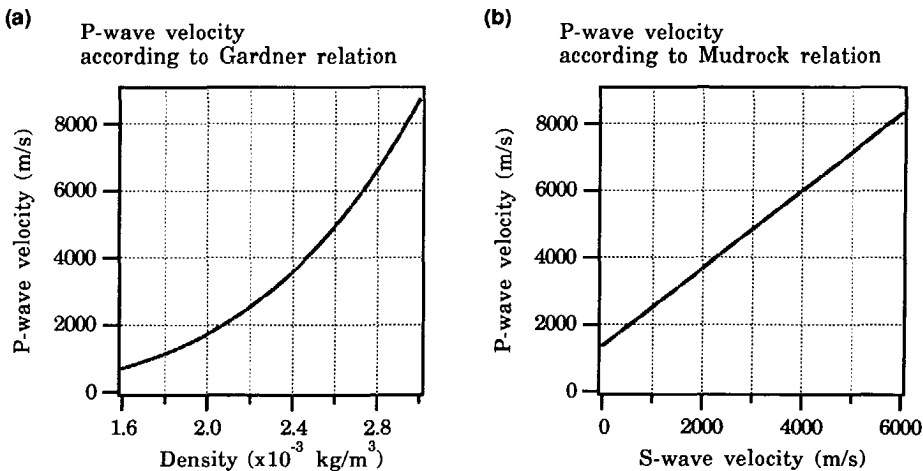


Fig. 6-4 (a) The Gardner relation (6-10) for $c=1.08 \times 10^{-10}$ and $\varepsilon=4$. (b) The Mudrock relation (6-11) for $a=1360$ and $b=1.16$.

$$(\alpha_i - a - b\beta_i)/\sigma_{mud}, \quad (6-12b)$$

where the standard deviations σ_{gar} and σ_{mud} express the uncertainty of the respective terms.

6.4 Robustness parameters

The p - τ gathers that are used in the inversion are obtained through the redatuming module of the DELPHI scheme. Errors in the macro velocity model(s) will introduce errors in the redatumed gathers. A distinction can be made between amplitude and traveltime errors.

6.4.1 Traveltimes errors

Regarding the traveltime errors, consider Fig. 6-5a where a simple model consisting of a homogeneous overburden over a target zone is pictured. For this simple

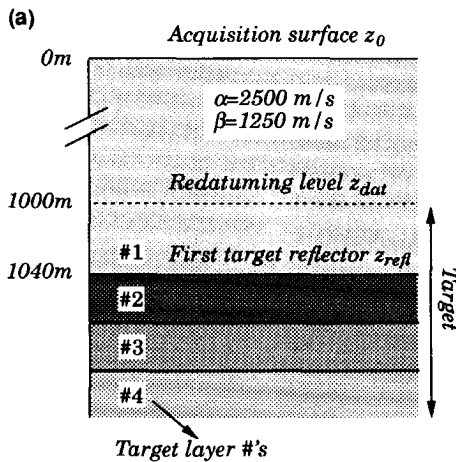
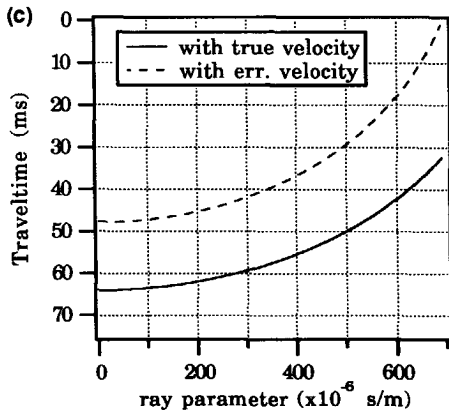
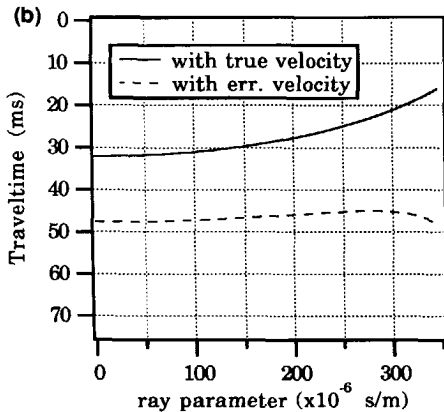


Fig. 6-5 (a) Model with a homogeneous overburden over a target zone. The first target layer, from 1000m to 1040m, has the same elastic properties as the overburden. (b) Traveltime curves for the redatumed PP data, using the true ($\alpha=2500$ m/s) and an erroneous ($\alpha=2550$ m/s) overburden velocity. (c) Traveltime curves for the redatumed SS data, using the true ($\beta=1250$ m/s) and an erroneous ($\beta=1237.5$ m/s) overburden velocity.



model, the redatuming can be done in the p - τ domain. For the first reflector of the target zone, the PP traveltimes at the surface z_0 are given by:

$$\tau_{surface} = 2(z_{refl} - z_0) \sqrt{\frac{1}{\alpha^2} - p^2}. \quad (6-13)$$

Going from the surface to a new datum at $z = z_{dat}$ can be accomplished by a simple time shift:

$$\tau_{dat} = \tau_{surface} - \Delta\tau, \text{ with} \quad (6-14a)$$

$$\Delta\tau = 2(z_{dat} - z_0) \sqrt{\frac{1}{\alpha^2} - p^2}. \quad (6-14b)$$

If one uses the correct velocity in the redatuming, the solid traveltime curve of Fig. 6-5b results. It is determined by:

$$\tau_{dat} = 2\Delta z \sqrt{\frac{1}{\alpha^2} - p^2} \quad (6-15)$$

where $\Delta z = z_{refl} - z_{dat}$ is the depth of the reflector with respect to the redatuming level. When using a redatuming velocity in (6-14b) that is only 2% too high, the striped curve of Fig. 6-5b results. Note that the erroneous traveltime shows less moveout than the true traveltime.

As was already mentioned in Section 6.2.3, the traveltimes of the events are accurately sensed by a full-waveform parametric inversion. The inversion algorithm can only match the erroneous moveout curve by assuming a velocity of the first target layer that is too low. Fitting relation (6-15) to the erroneous moveout curve on the interval between 0 and 250×10^{-6} s/m yields $\Delta z = 31$ m and $\alpha = 1308$ m/s. Therefore, based on traveltimes only, the P-wave velocity of the first target layer will be estimated much too low. The differential moveout of the target reflectors will remain correct, however. Assuming that the erroneous moveout of the first reflector remains approximately elliptic for the range of ray parameters that is used, implies that the estimated velocities for the other target layers remain unbiased.

So, based on the traveltimes, only the velocity of the first layer would be strongly affected. This will cause a high-amplitude reflection in the modeled data that is not present in the actual data. The elastic inversion algorithm will still try to fit the data, resulting in large estimation errors for all target layers.

If both PP and SS data are used in the inversion, the problems become even more obvious. Of the same elastic model, Fig. 6-5c shows the traveltimes of the redatumed SS data. The solid line represents the results with the true velocity,

whereas the striped line is obtained by using a velocity that is 1% too low. Note that the normal incidence time ($\approx 48\text{ms}$) is the same for both the erroneous PP and SS curves. The inversion algorithm can only accomplish this by making the P- and S-wave velocities of the first layer equal to each other. Since the S-wave velocity needs to be smaller than $1/\sqrt{2}$ times the P-wave velocity, this is physically impossible.

The discussed traveltimes errors will also exist for structurally more complex overburdens. The redatumed CMP gathers of types PP and SS will remain symmetric around $p=0$, however. This also holds when errors in the velocity model are present or if the new datum is not exactly parallel to (one of) the target layers. To account for the errors, a time shift is applied to the traces of the redatumed gathers. Because of the aforementioned symmetry, the time shifts that are applied to the PP and SS traces are parametrized through:

$$\begin{aligned}\Delta\tau_{type}(p) &= \tau_{type,0} + \tau_{type,2} p^2, \\ type &\in \{PP, SS\}.\end{aligned}\tag{6-16}$$

For the converted gathers, a linear relation is used:

$$\begin{aligned}\Delta\tau_{type}(p) &= \tau_{type,0} + \tau_{type,1} p, \\ type &\in \{SP, PS\}.\end{aligned}\tag{6-17}$$

The implementation in the actual inversion program is flexible: It is possible to use only a constant, p -independent time shift ($\tau_{type,0}$) or simply no correction at all.

6.4.2 Amplitude errors

The elastic inversion needs true amplitude data. Not only the *relative* amplitude behavior as a function of the ray parameter needs to be correct, but also the *absolute* values of the amplitudes. The multiple elimination procedure of the DELPHI scheme incorporates an adaptive procedure to obtain the absolute amplitudes of the surface data. An other method to obtain the absolute scaling is to match the data to a well-log derived reflectivity.

Subsequently, the redatuming procedure should restore the amplitude losses that occur during propagation. The geometrical divergence is determined by the velocity model and is implicitly corrected for in the redatuming. Amplitude losses due to elastic transmission and absorption can in principle be accounted for during the redatuming. It is difficult, however, to quantify these effects.

The inevitable amplitude errors in the redatumed gathers are modeled by a p -dependent scaling factor:

$$\text{Correct Trace} = s(p) \times \text{Redatumed Trace}\tag{6-18}$$

Again, because of their symmetry properties, the scaling factor for the PP and SS gathers is parametrized through:

$$\begin{aligned} s_{type}(p) &= s_{type,0} + s_{type,2} p^2, \\ type &\in \{PP, SS\}. \end{aligned} \quad (6-19)$$

For the converted gathers, a linear relation is used:

$$\begin{aligned} s_{type}(p) &= s_{type,0} + s_{type,1} p, \\ type &\in \{SP, PS\}. \end{aligned} \quad (6-20)$$

The same options that were mentioned in the traveltime discussion also apply here: It is possible to use only a constant, p -independent scaling ($s_{type,0}$) or simply no scaling correction at all.

6.4.3 Non-uniqueness aspects

There is a maximum of four robustness parameters (the polynomial coefficients) per data type. One can expect that especially the scaling parameters will introduce resolution problems. For the simple case of a targetzone with only two layers (i.e. one reflector), an extremely ill-resolved problem would result. But when the targetzone consists of a number of layers, the resolution will improve. Considering the traveltimes, the discussion in Section 6.4.1 has demonstrated that the traveltime parameters should be reasonably well resolved. Besides, all robustness parameters are stabilized through prior information.

Prior values for all robustness parameters but the 0th order scaling factor are zero. If the data is more or less on the correct amplitude scale, the prior value for $s_{type,0}$ is unity. All standard deviations are taken small enough to ensure that the time shifts remain small and the scaling factors remain close to unity.

6.5 Litho-elastic inversion.

In the majority of cases, only PP data will be available for the inversion. As was discussed in Section 6.2, the PP-only inverse problem is seriously ill-resolved. Especially when the data at large offsets are unreliable or simply not available, the inversion will heavily rely on the prior information that was discussed in Section 6.3. If the prior information is correct and "strong", accurate and stable results will be obtained.

The problem remains to relate the so-obtained elastic parameters (P-wave velocity, S-wave velocity and density) to quantities that are of importance for the description of hydrocarbon reservoirs. In the original DELPHI scheme, this is accomplished by a subsequent lithologic inversion of the elastic inversion results. From

the lithologic inversion research within DELPHI (Lörtzer and Berkhout 1992) the following was concluded:

- 1) It is generally possible to differentiate between different lithotypes. A lithotype denotes not only the lithology, e.g. sandstone, shale or limestone, but also the pore fill, gas, water or oil. So, a gas-filled and a water-filled sandstone are considered two different lithotypes.
- 2) The saturation of the pore fluids cannot accurately be obtained. For example, in the case of a gas sand, both P- and S-velocity remain practically constant when the gas saturation varies between 10% and 100%.
- 3) The porosity can accurately be determined.

The inversion approach of Lörtzer and Berkhout incorporates a classification step: The inversion is attempted for a number of possible lithotypes. The result with the lowest residual will identify the most like lithotype and its corresponding porosity.

In the lithologic inversion, relations between the rock- and pore parameters and the elastic parameters are used. If these relations are incorporated in the elastic inversion algorithm, the two inversion modules are effectively joined together.

6.5.1 Basic strategy

When assessing the economic value of a (potential) hydrocarbon reservoir, the porosity is one of the most important parameters. Fortunately, in many cases it can also be well resolved, as was concluded from the lithological inversion research. The following litho-elastic inversion strategy is proposed: The porosity will be included in the parametrization as a fourth layer parameter. Therefore, the following parametrization results:

- 1) Per layer, the P-wave velocity α , S-wave velocity β , density ρ and porosity ϕ .
- 2) For all layers but the last one, the layer thickness Δz .
- 3) Optionally, the robustness parameters as defined in Section 6.4.

The resolution of the resulting inverse problem is guaranteed by making use of relations between the elastic parameters and the porosity as prior information:

$$\begin{aligned}\alpha_i &= \alpha_i(\phi, z) + n_{\alpha,i}, \\ \beta_i &= \beta_i(\phi, z) + n_{\beta,i}, \\ \rho_i &= \rho_i(\phi) + n_{\rho,i}.\end{aligned}\tag{6-21}$$

The noise terms n express the assumed uncertainty on these relations. As the subscripts i indicate, a different set of relations is used *per* layer of the target zone. Only when the lithotypes of some of the layers are equal, equal relations are used.

The weighted mismatch terms with respect to the above lithologic relations will be appended to the residual vector \mathbf{e} , whose energy will be minimized:

$$\mathbf{e} = \begin{pmatrix} \mathbf{C}_n^{-1/2}(\mathbf{d} - \mathbf{g}(\mathbf{x})) \\ \mathbf{C}_{S,prior}^{-1/2}(\mathbf{d}_{S,prior} - \mathbf{g}_{S,prior}(\mathbf{x})) \\ \mathbf{C}_{L,prior}^{-1/2}(\mathbf{d}_{L,prior} - \mathbf{g}_{L,prior}(\mathbf{x})) \end{pmatrix}. \quad (6-22)$$

The first and second elements respectively denote the data mismatch and the “standard” prior relations mismatch, i.e. the macro parameters and the robustness parameters. The third element is the aforementioned mismatch with respect to the lithologic relations.

Following Lörtzer and Berkhout (1992), the Biot-Gassmann equations are used to relate the P- and S-wave velocity to the porosity. For some of the factors in these equations, an empirically obtained, linear depth dependence is used. This explains the z dependence that is seen in (6-21). If the target is sufficiently horizontal and of limited thickness, this dependence can be omitted. The simple volumetric average equation is used for the dependence of the density on the porosity. The specifics of the used relations will be discussed in Section 6.5.2.

All rock parameters (see Table 6-1) and pore fluid parameters (see Table 6-2) that occur in the Biot-Gassmann and density relations are considered to be known a priori. As Lörtzer and Berkhout (1992) describe, they can be obtained from nearby well logs, or from a rock physics database.

In principle, one would like to determine whether the pores of the rock are filled with merely water or (partially) with hydrocarbons, i.e. gas or oil. If there is indeed a mixture of water and hydrocarbons present, one would like to know the fractions of the different components. Unfortunately, the elastic parameters can only partially provide this information. Since the density and the compressibility of oil and water do not differ very much, it is generally not possible to distinguish between a water filled and an oil filled lithology. In case of a mixture of oil and gas, it will certainly not be possible to estimate the water saturation S_w , i.e. the fraction of the pore volume that is filled with water. Since the elastic properties of gas and water differ considerably, presence of gas *does* have a strong effect on the elastic parameters. Unfortunately a gas saturation of only 5% ($S_w=0.95$) has the same effect as a complete gas saturation ($S_w=0$).

So, based on the elastic parameters of a porous, fluid-filled rock, it is in practice only possible to distinguish between *some* gas and *no* gas. These two possibilities are classified as different lithotypes. For a sandstone lithology, a gas sand and a water sand are defined as two lithotypes, where it is understood that a sand with a small amount of gas is already considered a gas sand. In the same spirit, the oil

sand lithotype can be introduced, although it will be generally impossible to distinguish it from a water sand. Likewise, lithotypes for other lithologies are defined, e.g. a gas-filled limestone, a water-filled limestone etc.

For these discrete lithotypes, relations (6-21) will predict a different porosity dependence of the three elastic parameters. If, for a certain layer in the target zone a wrong lithotype assumption is made, this should lead to a reduced ability of the elastic inversion to match the data, i.e. higher residuals. Doing the inversion with different lithotype assumptions will then identify the most likely lithotype: the one with the lowest residuals. Making use of the fact that the objective function (the energy in the residuals) is the negative logarithm of the posterior pdf, relative probabilities of the different lithotypes can in theory be supplied, see Lörtzer and Berkhout (1992).

The advantages of the proposed strategy are threefold. First of all, the inverse problem is effectively stabilized by the three prior relations (6-21) per layer. Secondly, one of the layer parameters that is inverted for is the porosity, which is of direct practical significance. Thirdly, it is possible to test hypotheses of different lithotypes for a certain layer. The most likely lithotype will be identified by the result with the lowest residuals.

6.5.2 Elastic parameters as a function of the porosity

In this section, the specific form of the relations between the elastic parameters and the porosity—of which the generic definition was given by equations (6-21)—will be discussed. In principle, any set of relations, whether they are empirical or theoretical, can be used. It is e.g. conceivable to fit suitably chosen parametric relations to crossplots of well log data. In this research, the Gassmann-Biot relations are used for the P- and S-wave velocity. The relations will simply be introduced here, without discussing the physical principles they are based on. The contents of this section is largely based on Crans and Berkhout (1980) and Lörtzer and Berkhout (1992).

The Biot-Gassmann equation for the P-wave velocity is given by:

$$\alpha = \sqrt{\frac{1}{\rho \kappa_s} \left\{ 3 \frac{1 - \sigma_b}{1 + \sigma_b} \right\} \zeta + \frac{(1 - \zeta)^2}{1 - \zeta + \phi (\kappa_f / \kappa_s - 1)}}, \quad (6-23)$$

and for the S-wave velocity:

$$\beta = \sqrt{\frac{3\zeta}{4\rho \kappa_s} \left\{ \frac{1 - \sigma_b}{1 + \sigma_b} - 1 \right\}}, \quad (6-24)$$

where κ_s is the compressibility of the solid, σ_b is the Poisson's ratio of the bulk (i.e. the empty porous solid), ζ is the frame-strength factor and κ_f is the compressibility of the fluid in the pores. The frame strength factor is defined by:

$$\zeta = \frac{\kappa_s}{\kappa_b}, \quad (6-25)$$

where κ_b is the compressibility of the bulk.

The density that occurs in the relations is that of the fluid-filled porous rock and is equal to the density in the elastic parametrization. The density is obtained through a volumetric average of the fluid and solid constituents of the rock:

$$\rho = (1 - \phi)\rho_s + \phi\rho_f, \quad (6-26)$$

where ρ_s and ρ_f respectively denote the density of the solid and the pore fluid.

If the fluid in the pores consists of a mixture of a hydrocarbon and water, the fluid parameters are given by:

$$\begin{aligned} \kappa_f &= S_w \kappa_w + (1 - S_w) \kappa_{hc}, \\ \rho_f &= S_w \rho_w + (1 - S_w) \rho_{hc}, \end{aligned} \quad (6-27)$$

where S_w is the water saturation, i.e. the fraction of the pore volume that is filled with water. The subscripts w and hc respectively denote the water and hydrocarbon fractions. Relations (6-27) are given for the sake of completeness. In the inversion, discrete lithotypes are used that merely distinguish between water filled ($S_w=1$) and gas or oil filled ($S_w=0$).

As proposed in Crans and Berkhout (1980), some extra (semi-)empirical relations are employed. The Poisson's ratio of the bulk is assumed to decrease linearly with depth:

$$\sigma_b = \sigma_0 - \sigma'(z - z_0) \quad (6-28)$$

For the frame-strength factor ζ , the semi-empirical equation of Geertsma (1961) and van der Knaap (1959) is used:

$$\frac{1}{\zeta} - 1 = \zeta_1 \phi \left\{ (\zeta_2 \kappa_s)^{\zeta_3} S_{eff} + 1 \right\}^{-1/\zeta_3}. \quad (6-29)$$

This equation interrelates some of the lithologic parameters that occur in the Biot Gassmann equations. The effective stress S_{eff} , the difference between lithostatic and hydrostatic stress, is assumed to have a linear depth dependence:

Table 6-1 *Seismic-lithological parameters with typical values for the lithologies sandstone and shale.*

| Parameter | | Description | Unit | Sand | Shale |
|-----------|------------|---|------------------------|------------------------|------------------------|
| Rock | κ_s | Compressibility of the solid | m^2/N | 2.71×10^{-11} | 2.53×10^{-11} |
| | ρ_s | Density of the solid | kg/m^3 | 2.65×10^3 | 2.70×10^3 |
| | ζ_1 | Frame strength parameter #1 | | 50 | 55 |
| | ζ_2 | Frame strength parameter #2 | | 1.46×10^6 | 1.30×10^6 |
| | ζ_3 | Frame strength parameter #3 | | 1.70 | 1.50 |
| | σ_0 | Poisson's ratio of bulk at reference depth | | 0.20 | 0.15 |
| | σ' | Gradient of σ_b | m^{-1} | 1.26×10^{-5} | 0.33×10^{-5} |
| Other | z_0 | Reference depth | m | 2×10^3 | 2×10^3 |
| | S_0 | Effective stress S_{eff} at reference depth | N/m^2 | 2.52×10^7 | 2.23×10^7 |

Table 6-2 *Fluid parameters for water, gas and oil at a reference depth of 2km.*

| Parameter | | Description | Unit | Water | Oil | Gas |
|-----------|------------|-----------------|------------------------|-----------------------|-----------------------|-----------------------|
| Fluid | κ_f | Compressibility | m^2/N | 4.2×10^{-10} | 6.3×10^{-10} | 360×10^{-10} |
| | ρ_f | Density | kg/m^3 | 1.09×10^3 | 0.85×10^3 | 0.13×10^3 |

$$S_{eff} = S_0 + S'(z - z_0). \quad (6-30)$$

The three parameters ζ_1 , ζ_2 and ζ_3 depend on the packing, the dominant grain size and the sorting and cementation of the grains.

An overview of the seismic-lithological parameters that are used to model the elastic parameters is given in Table 6-1. Typical values are given for sandstone and shale at a depth of about 2km. At that same depth, typical values for the three types of fluids that are most likely to be encountered are given in Table 6-2.

The resulting values for the elastic parameters as a function of the porosity are plotted in Fig. 6-6 for four lithotypes; a water-filled shale, and a sand with water, oil and gas fill. Note that the variation of the S-wave velocity with respect to the type of pore fluid is negligible. Combined with the strong fluid dependence of the P-wave velocity, this leads to the strong dependence of Poisson's ratio on the pore fluid.

6.5.3 Time average equation

The Biot-Gassmann equations offer a physical description of the dependence of the P- and S-wave velocity on the porosity. The often used time-average equation also

describes the velocity as a function of the porosity. For the P-wave velocity α and the S-wave velocity β , the time average equations are given by:

$$\alpha = 1/(c_{\alpha,0} + c_{\alpha,1}\phi),$$

$$\beta = 1/(c_{\beta,0} + c_{\beta,1}\phi).$$
(6-31)

In order to investigate whether such simple relations can accurately describe the velocity, as predicted by the Biot-Gassmann equations, a least-squares curve fit of relation (6-31) is performed. Doing the fit for porosities between 3% and 30%, the

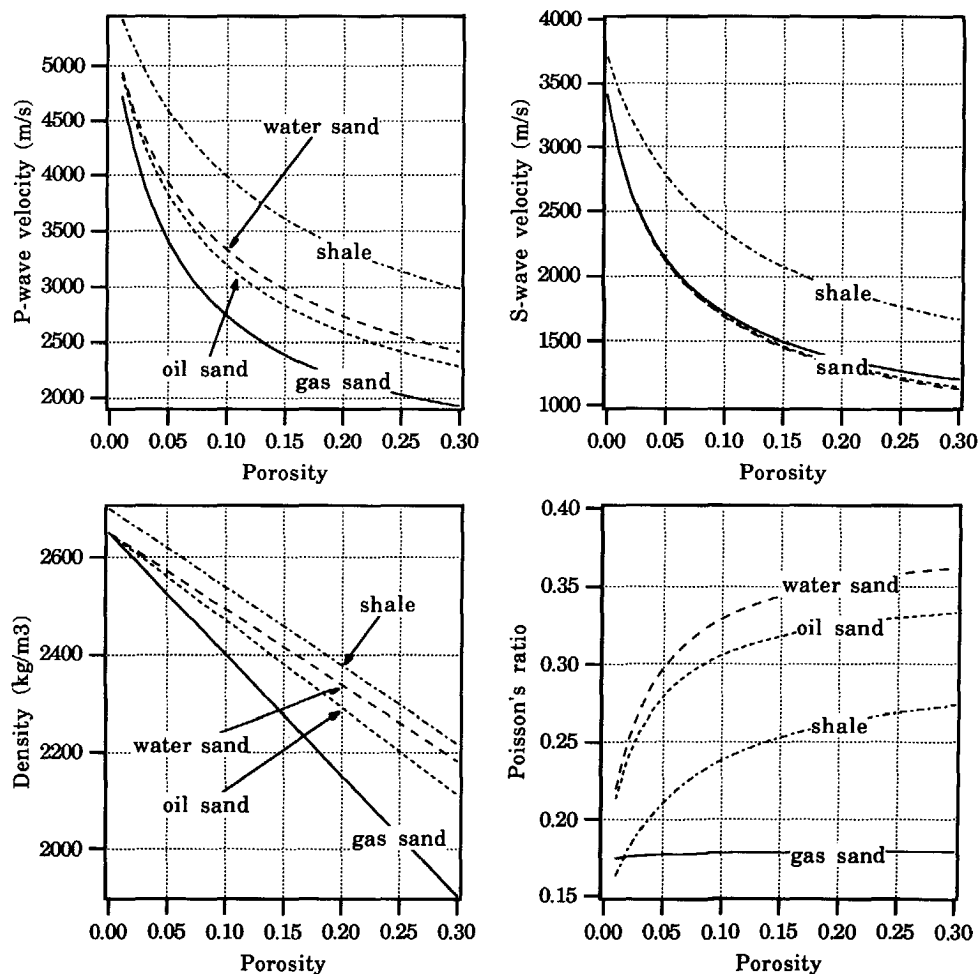


Fig. 6-6 The elastic parameters as a function of the porosity for four different lithotypes. Note again that the Poisson's ratio is an excellent discriminator between water- and gas fill, particularly at high porosity.

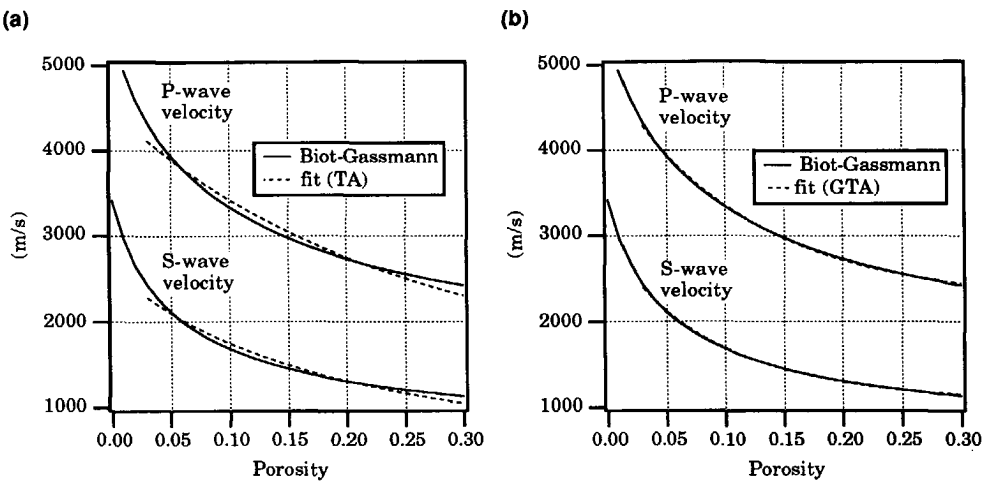


Fig. 6-7 (a) Best fit of the time average (TA) equation (6-31) to the Gassmann predicted velocities (P and S) of a water sand at 2000m. (a) Same, but now using the generalized time average (GTA) equation (6-32).

results for the P- and S-wave velocity of the water sand are shown in Fig. 6-7(a). The mismatch is rather small, and in many cases, the time-average equation will indeed be sufficient to describe the porosity dependence of the velocities. Note that the fitting process generally yields TA coefficients that may not have a direct physical meaning,

A better fit can be obtained by extending the time average equation with a ϕ^2 term. The resulting generalized time-average (GTA) relations are given by:

$$\alpha = 1 / (c_{\alpha,0} + c_{\alpha,1}\phi + c_{\alpha,2}\phi^2),$$
$$\beta = 1 / (c_{\beta,0} + c_{\beta,1}\phi + c_{\beta,2}\phi^2).$$

(6-32)

Again for the water sand, the best fit results of these relations are shown in Fig. 6-7b. As can be seen, the mismatch is very small now. The coefficients of the GTA relations for four important lithotypes (obtained by fitting) are given in Table 6-3.

Table 6-3 Generalized time-average coefficients for the four lithotypes of Fig. 6-6.

| Lithotype | $c_{\alpha,0}$ | $c_{\alpha,1}$ | $c_{\alpha,2}$ | $c_{\beta,0}$ | $c_{\beta,1}$ | $c_{\beta,2}$ |
|------------|-----------------------|-----------------------|------------------------|-----------------------|-----------------------|------------------------|
| water sand | 2.01×10^{-4} | 1.12×10^{-3} | -1.42×10^{-3} | 3.30×10^{-4} | 3.02×10^{-3} | -4.02×10^{-3} |
| gas sand | 2.08×10^{-4} | 1.82×10^{-3} | -2.72×10^{-3} | 3.31×10^{-4} | 2.92×10^{-3} | -4.37×10^{-3} |
| oil sand | 2.01×10^{-4} | 1.27×10^{-3} | -1.67×10^{-3} | 3.30×10^{-4} | 2.99×10^{-3} | -4.10×10^{-3} |
| shale | 1.81×10^{-4} | 7.82×10^{-4} | -9.22×10^{-4} | 2.83×10^{-4} | 1.63×10^{-3} | -1.97×10^{-3} |

In this chapter, three examples will be presented that illustrate the potential of the proposed inversion technique. In these examples, synthetic data is used. Unlike field data, synthetic data offers the valuable ability to rigorously check the accuracy of the obtained inversion results. The author acknowledges, however, that a successful inversion of field data is the ultimate proof of the practical applicability of the proposed inversion method.

In the synthetic examples, care is taken that realistic data is used. This means a.o. that the data is generated with elastic finite difference modeling rather than using the same reflectivity algorithm that is used in the forward modeling part of the inversion. After the redatuming step (for two of the three experiments, target data is directly modeled), the shot gathers at the target level are processed into target CMP p - τ gathers. Due to the limited aperture of the x - t data, artifacts will appear in the p - τ data, as would be the case with field data.

The three examples that will be given, each illustrate a different aspect of the elastic inversion:

- 1) A 2D overburden and a 1D target zone. Multicomponent surface data are modeled and subsequently, the full suite of DELPHI processing modules is applied. For the elastic inversion, only macro parameters are supplied as prior information.
- 2) A target zone with moderate conflicting dips (up to 10°) and laterally varying elastic parameters. Target data is directly modeled. The elastic inversion makes use of more prior information than in the previous example: The macro parameters, and the empirical Gardner and Mudrock relations.
- 3) Litho-elastic inversion of a reservoir sand where the porosity and fluid fill change laterally. Here, the maximal amount of prior information is used.

All examples in this chapter are the result of a team effort. For the first example, the whole DELPHI team was involved. Especially Greg Haimé (finite-difference modeling) and Cees de Bruin (redatuming, p - τ generation) contributed to the other examples.

7.1 Elastic inversion for a 1D target under a 2D overburden.

7.1.1 Elastic model

The experiment that will be discussed in this section is based on the elastic model of Fig. 7-1. In the overburden, an anticline is present (macro layer #4). Macro layer #3 is discontinuous because of this anticline. As can be seen in the accompanying Table 7-1, the contrasts in the macro parameters are quite strong. The target zone is the sequence of relatively thin layers at a depth of 550m.

7.1.2 Modeling and pre-processing

Using an elastic finite difference algorithm, four data sets are generated, corresponding to horizontal (τ_{xz}) and vertical stress (τ_{zz}) sources and horizontal (v_x) and vertical (v_z) receivers on a free surface. The source signature is a 30Hz central frequency Ricker wavelet, see Fig. 7-4c. A total of 128 shot locations with a spacing of

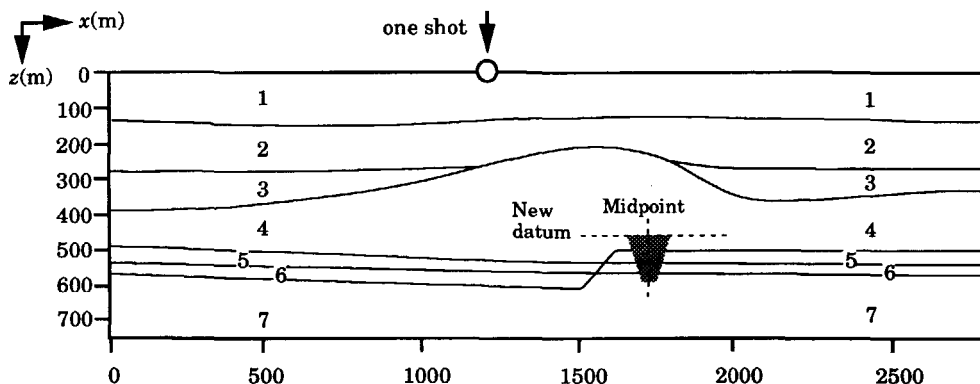


Fig. 7-1 The elastic model that is used for the inversion experiment.

Table 7-1 Elastic layer parameters of the model of Fig. 7-1.

| Layer | P-wave velocity (m/s) | S-wave velocity (m/s) | Density (10^{-3}kg/m^3) | Poisson's ratio |
|-------|-----------------------|-----------------------|------------------------------------|-----------------|
| 1 | 2400 | 1400 | 1.0 | 0.243 |
| 2 | 3000 | 2000 | 1.6 | 0.100 |
| 3 | 3000 | 2000 | 2.1 | 0.100 |
| 4 | 4100 | 2200 | 2.2 | 0.297 |
| 5 | 3700 | 2000 | 2.3 | 0.293 |
| 6 | 4200 | 2400 | 2.0 | 0.258 |
| 7 | 3500 | 2100 | 1.8 | 0.219 |

16m are used. The receiver spacing is 8m. As an example, the $v_z\tau_{zz}$, $v_z\tau_{xz}$, $v_x\tau_{zz}$ and $v_x\tau_{xz}$ shot gathers (the first symbol indicates the receiver type, the second indicates the source type) for the shot position indicated in Fig. 7-1 are shown in Fig. 7-2a. The surface waves (ground roll) are very strong and are removed by a conventional k_x - ω filtering technique. The resulting shot gathers are shown in Fig. 7-2b.

The data are now further processed according to the DELPHI scheme, see Fig. 2-1 on page 12. As described in Chapter 7 of Wapenaar and Berkhout (1989), all processing modules operate on monochromatic data sets that represent the complete multi-shot experiment for a single frequency component. First, the data is decomposed into up- and downgoing P- and S-waves, see Wapenaar et al. (1990). The decomposition at the receiver side operates on common shot gathers and transforms the total velocity $v=(v_x, v_z)^t$ into upgoing P- and S-waves. Next, the data is reordered into common receiver gathers and the stress $\tau_z=(\tau_{xz}, \tau_{zz})^t$ at the source side is decomposed into downgoing P- and S-waves. The resulting shot gathers of pure P-wave and S-wave responses are shown in Fig. 7-2c.

Next, the surface-related multiples are eliminated with the adaptive procedure of Verschuur (1991), using the elastic reflectivity of the free surface. An important by-product of this procedure is the source wavelet of the different data sets on an *absolute* amplitude scale. In the elimination procedure, no extra information about the subsurface is needed, since the data itself is used in the "elimination operator". The data after the surface related multiple elimination are shown in Fig. 7-2d. Comparing Fig. 7-2a and Fig. 7-2d demonstrates the tremendous clean-up of the

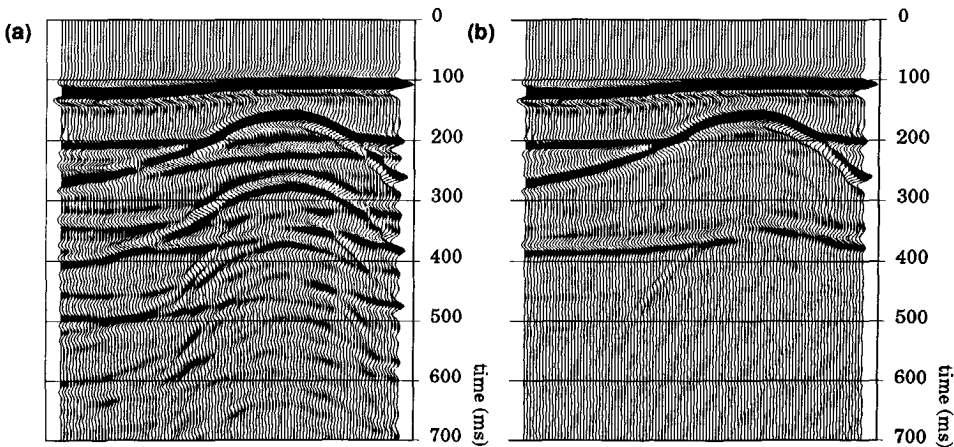


Fig. 7-3 PP zero-offset section. (a) With surface-related multiples. (b) After the removal of the surface related multiples. The internal multiples are much lower in amplitude than the surface-related multiples.

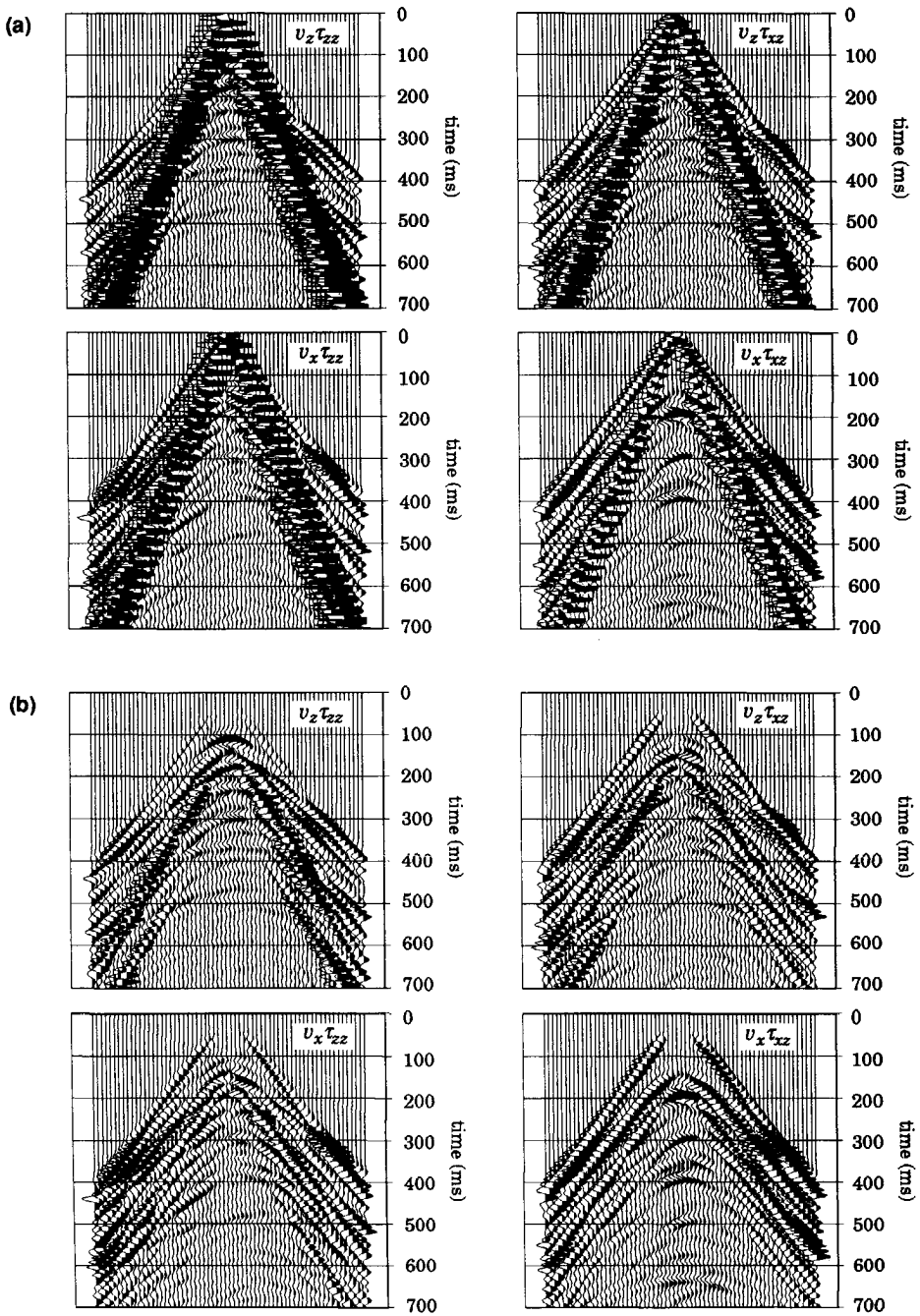


Fig. 7-2 Multi-component shot gathers at $x=1264\text{m}$. (a) Raw shot gathers, including strong ground roll. (b) After ground-roll removal through a $k_x\text{-}\omega$ filtering.

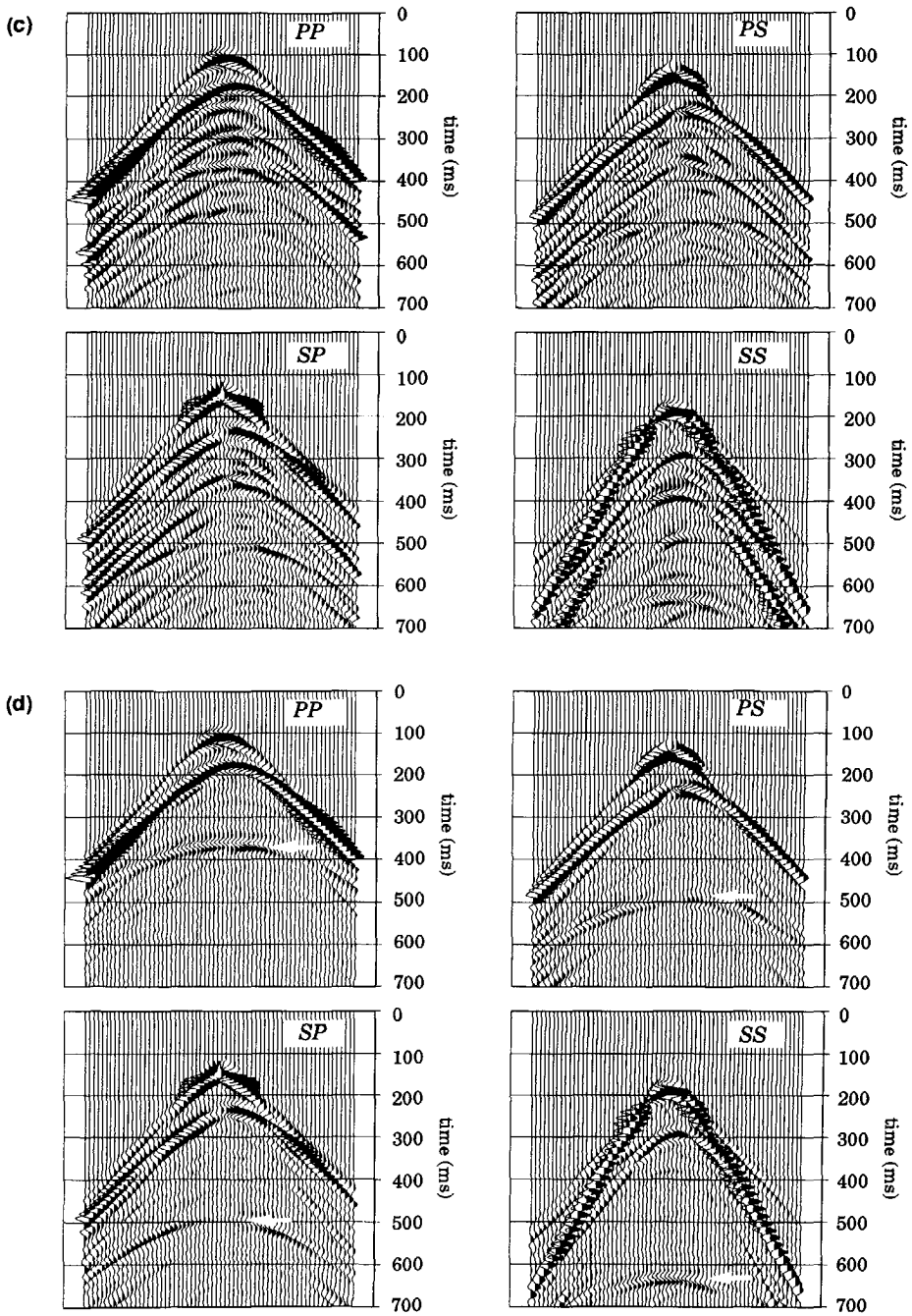


Fig. 7-2 Continued (c) After decomposition into P- and S-waves. (d) After surface-related multiple elimination. The target reflections in the PP and SS gathers are indicated by arrows.

data. The target reflections, indicated by the arrows in Fig. 7-2d, are quite weak with respect to the reflections of the macro boundaries. Using the same elastic model, Verschuur (1991) compares the results from an elastic modeling using pure P- and S-wave sources/receivers at a non-reflecting surface with the results after the three DELPHI pre-processing steps, i.e. ground-roll removal, decomposition and surface related multiple elimination. The differences are insignificant. A zero-offset section of the PP data before and after the multiple elimination is shown in Fig. 7-3. Note that the remaining internal multiples have a much lower amplitude than the surface-related multiples.

The next module of the DELPHI scheme, macro-model estimation, was performed for this data set, see Cox (1991), but the results are not shown here. For the redatuming procedure, the new datum is chosen 50m above the horizontal top reflector of the target at the right-hand side of the model. In this example, the elastic inversion will be performed at a single lateral position. As indicated in Fig. 7-1, it is chosen near the middle of the model so as to have a large offset range available.

7.1.3 Data at the target level

The target model is depicted in Fig. 7-4. The first layer is actually part of macro layer #4 and has a thickness of 50m, as defined by the choice of redatuming level. The target's elastic parameters are chosen rather arbitrarily, so that the empirical

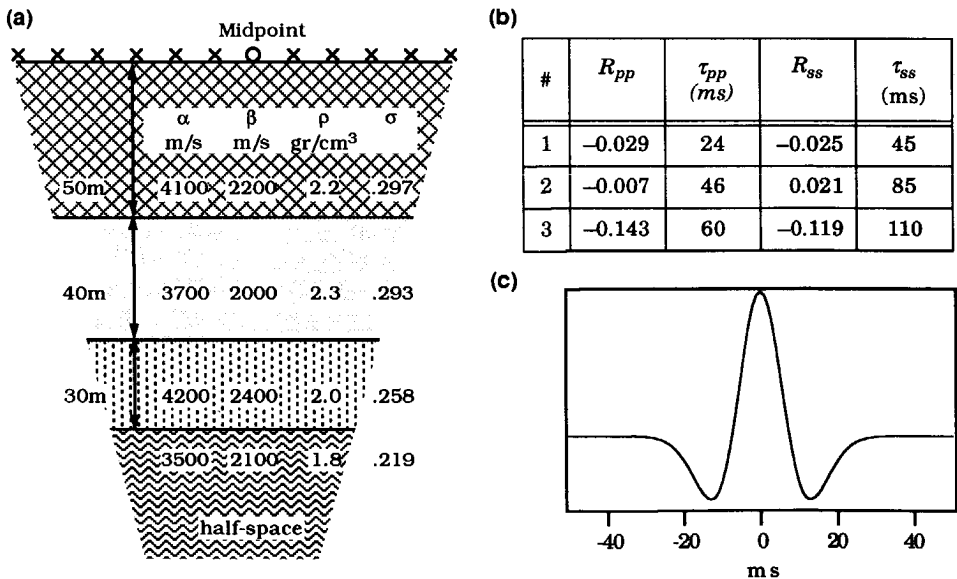


Fig. 7-4 (a) The local elastic model with four layers and three reflectors. (b) Normal incidence reflection coefficients of the target boundaries and the corresponding two-way traveltimes for both PP and SS data. (c) 30Hz central frequency Ricker wavelet, used for the modeling.

relations that were discussed in Section 6.3.2 cannot be used. Another obstacle for a successful inversion of this target is the very small reflectivity of the first two boundaries, as can be seen from the table of Fig. 7-4. This will make the inversion for the associated layer parameters quite difficult. To still obtain a meaningful result, the inversion is only done for a combination of PP and SS data, which can be expected to perform best.

The redatumed PP and SS CMP gathers in the p - τ domain are shown in Fig. 7-5. Besides the strong negative event that corresponds to the third boundary of the target, it is difficult to distinguish the other two reflections. Therefore, a p - τ modeling of the 1D target model using a high frequency wavelet (150Hz Ricker) is performed and the resulting p - τ gathers are shown in Fig. 7-6. It is indeed apparent that the first two reflectors have low amplitudes. Only the amplitude of the SS

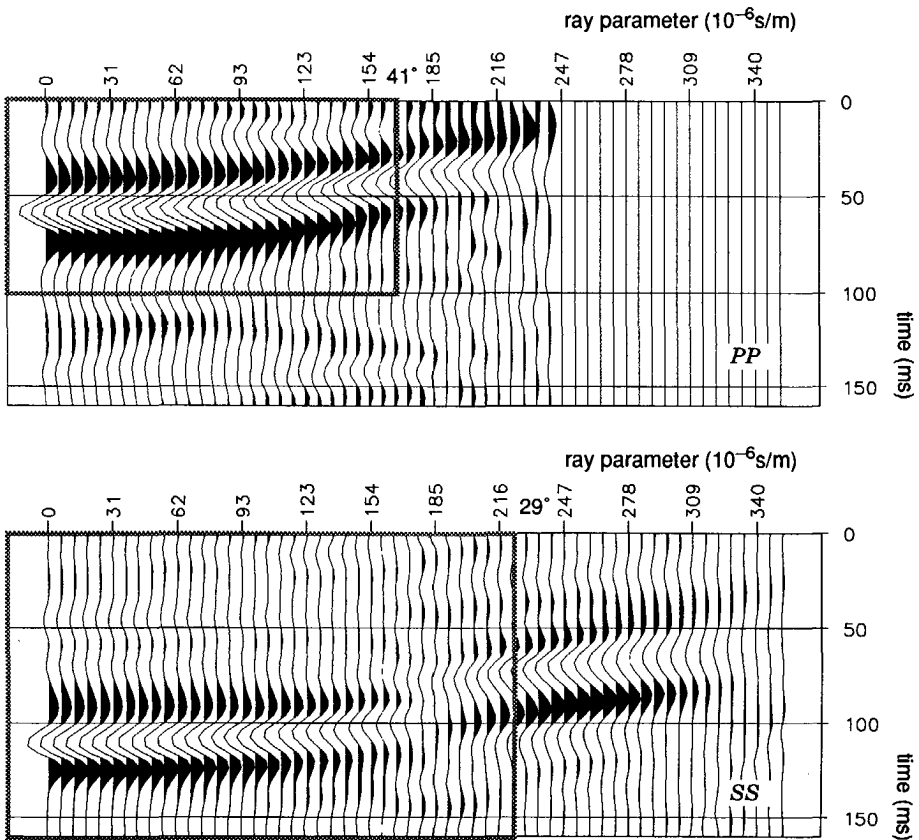


Fig. 7-5 p - τ gathers obtained by a redatuming of the pre-processed finite difference data. The ray parameter interval is $\Delta p = 6.17 \times 10^{-6}$ s/m.

reflection of the second boundary becomes strong after the polarity reversal at $p \approx 120 \times 10^{-6} \text{ s/m}$. This strong negative reflection can also be observed in the redatumed SS gather of Fig. 7-5.

The noisy looking traces in the SS gather for ray parameters between 240×10^{-6} and $270 \times 10^{-6} \text{ s/m}$ ($=1/\alpha_2$) are caused by converted internal P-wave multiples. For the P-waves in the second target layer, this interval corresponds to angles between 60 and 90 degrees. As was discussed in Section 4.4, for p approaching $1/\alpha_2$, the magnitudes of the reflection coefficients that cause the multiples become close to unity, which explains the strong multiple trains. Because of the limited time window, wrap-around occurs. The phenomenon stops abruptly after $270 \times 10^{-6} \text{ s/m}$ where the P-waves in the second layer have become evanescent. Note that the P-waves in the third layer are already evanescent at $p = 238 \times 10^{-6} \text{ s/m}$.

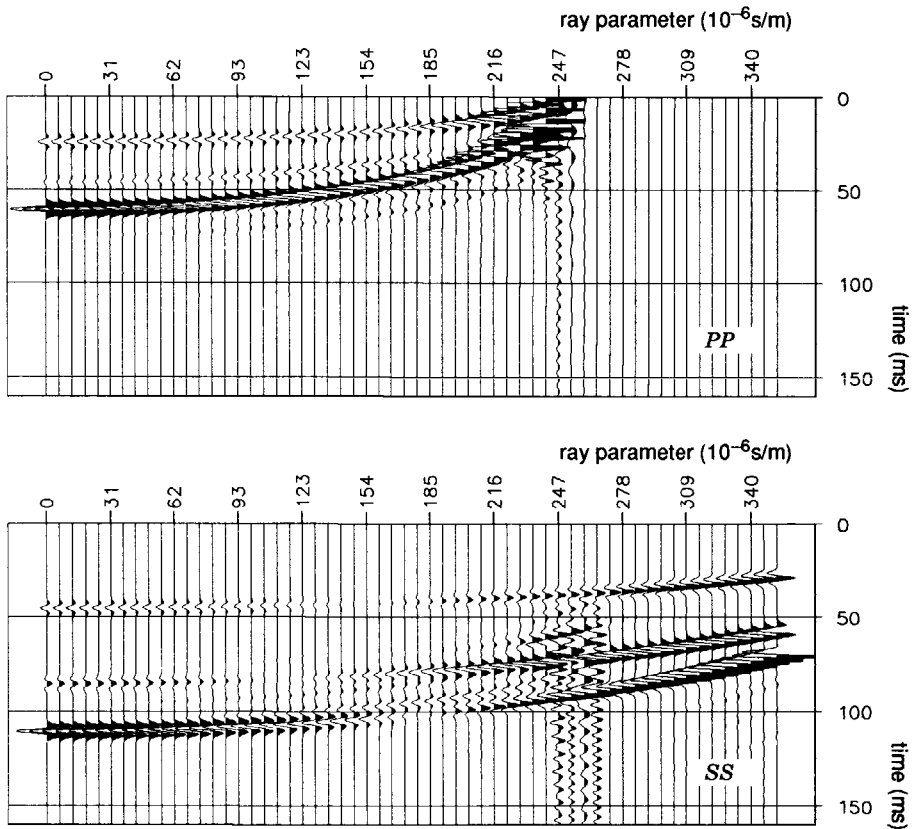


Fig. 7-6 Using the recursive reflectivity algorithm, p - τ gathers are modeled with a 150 Hz central frequency Ricker wavelet.

On the redatumed gathers of Fig. 7-5, the ranges of ray parameters and travel-times that will be used in the inversion are indicated by the gray boxes. This corresponds to a maximum incident angle in the first target layer of 41 degrees for the PP data and 29 degrees for the SS data. As can best be seen from the p - τ modeled data of Fig. 7-6, the SS data shows much more "AVO" than the PP data. It can therefore be expected that the inclusion of the SS data in the inversion will greatly improve the resolution of the inverse problem.

7.1.4 Robustness, Initial and Prior models

Before discussing the actual inversion results, a number of issues have to be clarified:

- *Robustness parameters*

The reflectors in the overburden are so strong that, due to elastic transmission losses, the observed reflection amplitudes in the p - τ gathers are on average 30% lower than they should be. For the amplitude correction, a constant value for all ray parameters is used, i.e. only the coefficient $s_{type,0}$ from equation (6-19). The a priori value for $s_{type,0}$ is therefore set to 1.3. The corresponding standard deviation is set to 0.05. Using a larger standard deviation resulted in unacceptable values for the estimated scaling factors. For this model and the used range of ray parameters, the scaling factors are apparently ill-resolved parameters. As was already mentioned in Section 6.4.2, in practice, a ball-park value for the scaling factor will be supplied by the adaptive multiple elimination method. At the target level, the obtained value may be refined by matching the data to a well-log based reflectivity.

For the time shifts, the 0th and 2nd order coefficients are used. The prior value for all four coefficients is zero. The standard deviation on $\tau_{pp,0}$ and $\tau_{ss,0}$ is set to 5ms. The standard deviations on the 2nd order coefficients $\tau_{pp,2}$ and $\tau_{ss,2}$ are chosen such that one standard deviation will cause a time shift of 5ms at the maximum ray parameter.

- *Prior information*

Prior information is used on the targetzone *averages* of the P-wave velocity, Poisson's ratio and density, see Section 6.3.1. Table 7-2 shows the true and prior values with the corresponding standard deviations. The prior values for $\langle\alpha\rangle$ and $\langle\sigma\rangle$ are chosen close to the ones of the corresponding macro layer, i.e. layer #4 from the global model of Fig. 7-1. As was shown in Section 3.6.1, the density *ratios* determine the reflectivity behavior. Therefore, the average density $\langle\rho\rangle$ is a completely unresolved parameter. Its true value is used as prior information to allow an easy evaluation of the estimated results. The empirical relations are not used as prior information.

Because the amplitudes of the first two reflectors are so low, also prior information on the PP normal-incidence traveltimes is used, with a standard deviation of 5ms.

In practice, this information will be supplied by a preceding poststack inversion, see Section 6.1.2. The resulting “penalty term” in the objective function prevents that the traveltimes wander away too much from their initial values. They are likely to do so at the start of the inversion, since the initial reflectivity for the associated boundaries is zero.

- *Initial model*

As was already mentioned in Section 6.1.2, it is important that the initial travel-times are within one peak-to-trough distance from the actual ones. In this experiment, the errors in the initial traveltimes are less than 10ms. In Fig. 7-7, the initial model is shown together with the true and estimated values as a function of depth. As can be seen, both the initial Poisson’s ratios and densities of all layers are initially without contrast and equal to the prior targetzone averages. The initial P-wave velocity is without contrast for the first three layers. The large negative reflection is accommodated for in the initial model by a drop in the P-wave velocity of the fourth layer. Note that when a poststack inversion would have been used to obtain an initial model (see Section 6.1.2), a similar initial model would have been obtained. The initial traveltimes would be more accurate, however. The stacked data would resemble the zero-offset section of Fig. 7-3b.

7.1.5 Results

In Fig. 7-7, the initial, true and estimated models for P-wave velocity, S-wave velocity, density and Poisson’s ratio are shown. The parameters of the first two layers, that are associated with the low-amplitude reflectors are indeed estimated worst. The density result is remarkably accurate for all layers. The same is true for the layer thicknesses and, consequently, the depths of the boundaries. For the first two layers, the errors in the P-wave and S-wave velocities are anti-correlated, resulting in the relatively large errors for the Poisson’s ratios in these layers.

The results for the robustness parameters are represented in Table 7-3. For the traveltime corrections, not the—quite meaningless—values for $\tau_{type,2}$ are shown but rather the resulting time shift at the highest ray parameter that is used (per reflectivity type). The shifts are considerable. Performing the inversion without

Table 7-2 True and prior values with the corresponding standard deviations for the targetzone averaged P-wave velocity, Poisson’s ratio and density.

| Prior item | unit | True value | Prior value | StdDev |
|------------------------|-----------------------------|------------|-------------|--------|
| $\langle\alpha\rangle$ | m/s | 3875 | 4000 | 300 |
| $\langle\sigma\rangle$ | — | 0.276 | 0.300 | 0.10 |
| $\langle\rho\rangle$ | 10^{-3} kg/m ³ | 2.07 | 2.07 | 0.10 |

the time shift parameters gave indeed a significant increase in the overall estimation error.

In Fig. 7-8, the residuals after the inversion are shown, plotted on the same amplitude scale as the original data. Laterally coherent events have remained. One reason for this is that the wavelet has changed due to grid dispersion of the modeling

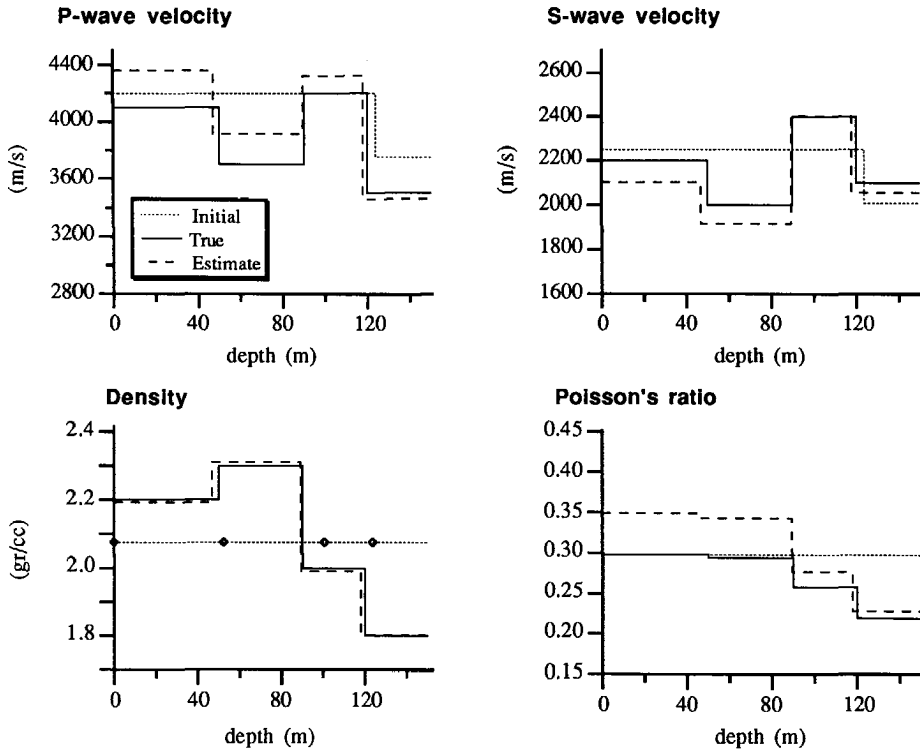


Fig. 7-7 Initial, true and estimated models for P-wave velocity, density and Poisson's ratio. The initial depths are indicated by the diamond-shaped markers in the density plot.

Table 7-3 Results for the scaling and time shifts at the start trace ($p=0$) and the final trace (PP: $p=160 \times 10^{-6}$ s/m; SS: $p=222 \times 10^{-6}$ s/m). For the scaling, a constant value for the whole p - τ gather is estimated (the 0^{th} order term).

| Prior item | PP | | SS | |
|------------|------------|---------|------------|---------|
| | Time shift | Scaling | Time shift | Scaling |
| Start | -2.4ms | 1.18 | 1.9ms | 1.32 |
| Final | -2.6ms | 1.18 | 4.7ms | 1.32 |

scheme. Besides, coherent events that are not target reflections can already be observed in the redatumed gathers of Fig. 7-5. These events, which can be diffractions, internal multiples (from macro boundaries) or modeling/processing artifacts will of course also appear in the residuals.

In order to illustrate that the inversion is relatively insensitive to purely random noise, the same target-related CMP gathers are directly modeled in the p - τ domain with the forward algorithm that is used in the inversion. Bandlimited noise ($f_{max}=70\text{Hz}$) with a standard deviation of $\sigma_n=0.03$ is added and the resulting noisy gathers are shown in Fig. 7-9. Using the same initial model and prior information, the inversion is performed once more. The results, only for P-wave and S-wave velocity are shown in Fig. 7-10. Compared to Fig. 7-7, the results have improved considerably. Only the estimated parameters of the fourth layer, which is not bounded by a lower interface, have become less accurate.

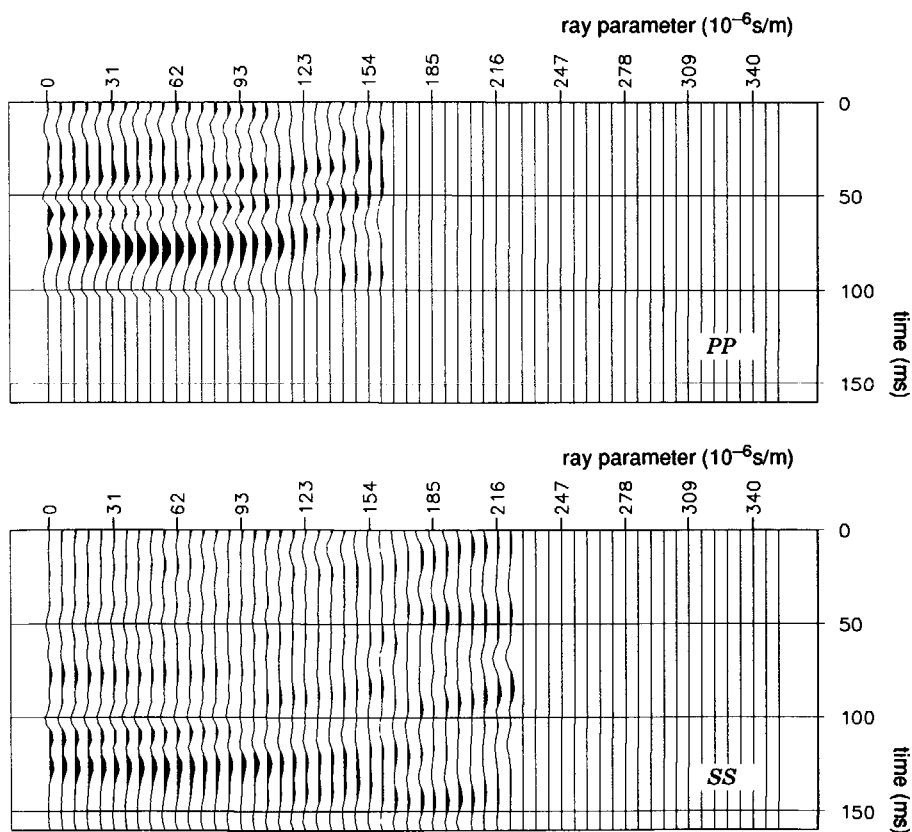


Fig. 7-8 Residuals after inverting the redatumed p - τ gathers of Fig. 7-5.

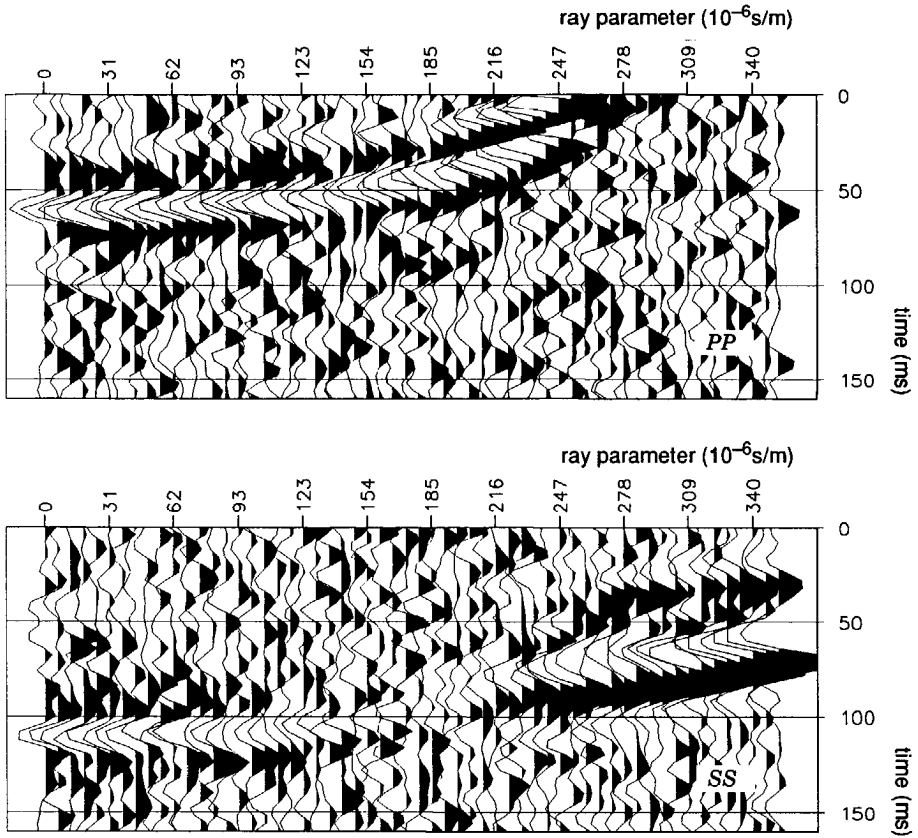


Fig. 7-9 p - τ CMP gathers that are modeled with the reflectivity method. Bandlimited noise (laterally uncorrelated) has been added.

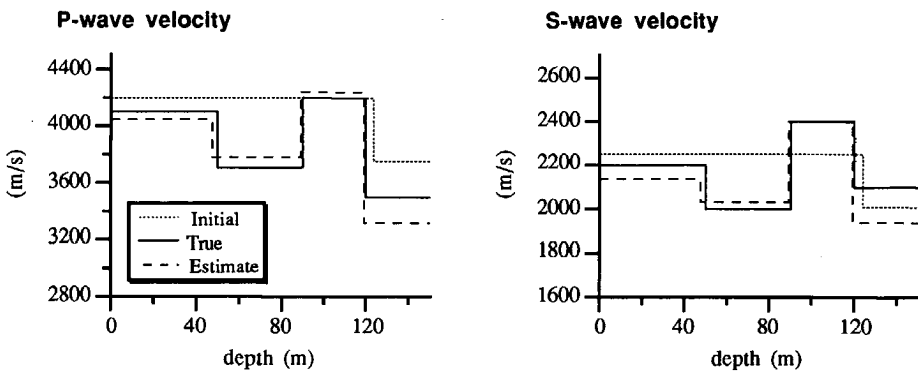


Fig. 7-10 Inversion results for P-wave and S-wave velocity using data with random noise only.

The average errors in the P- and S-wave velocity are 50 and 36 m/s respectively. With a numerical evaluation of the a posteriori covariance matrix, see Section 5.2.3, the predicted standard deviations for P- and S-wave velocity (averaged over the four layers) are 69 and 48m/s respectively, which agrees well with the inversion result.

7.1.6 Conclusions

Considering once more Fig. 7-5 (the redatumed p - τ gathers), it can be stated that the inversion has done a good job, regarding the very low amplitudes of the first two reflectors. However, in order to arrive at this result a combination of PP and SS data was required. Constraining of the traveltime thicknesses as well as a strong constraining of the scaling factor were necessary.

7.2 Inversion for a laterally varying targetzone

In this experiment, it is investigated whether the inversion is robust with respect to the assumption of a locally 1D medium. The elastic model that is used in the experiment is shown in Fig. 7-11 and consists of five target layers. Only the parameters of the fourth target layer vary laterally. The non-horizontal sections of the second and third boundaries have dips of 10 and 5 degrees respectively. The elastic parameters of the layers are shown in Table 7-4. Contrary to the model of Section 7.1, they agree well with the empirical Gardner and Mudrock equations, as can be seen from a comparison with Fig. 6-4. The laterally varying parameters of the fourth layer are shown in Fig. 7-12.

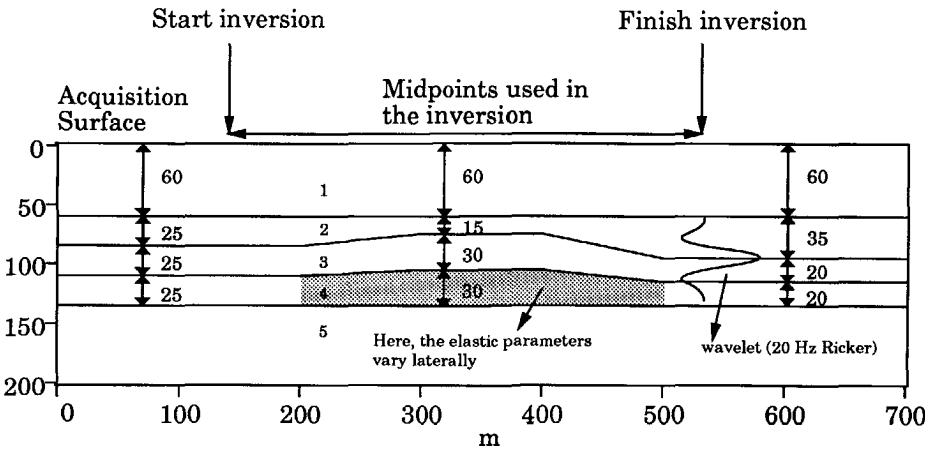


Fig. 7-11 The 2D targetzone model for the inversion experiment. Only the parameters of the fourth layer vary laterally.

Table 7-4 Elastic layer parameters of the model of Fig. 7-11. For layer 4, the parameters vary laterally. The tabulated value is valid for $x \leq 200\text{m}$ and $x \geq 500\text{m}$.

| Layer | P-wave velocity (m/s) | S-wave velocity (m/s) | Density (10^{-3}kg/m^3) | Poisson's ratio |
|-------|-----------------------|-----------------------|------------------------------------|-----------------|
| 1 | 2700 | 1270 | 2.26 | 0.36 |
| 2 | 3500 | 1660 | 2.36 | 0.35 |
| 3 | 2700 | 1200 | 2.28 | 0.38 |
| 4* | 3300 | 1760 | 2.37 | 0.30 |
| 5 | 4000 | 2160 | 2.42 | 0.29 |

7.2.1 Modeling and processing

At the surface, shot gathers are modeled with pure P-wave and S-wave sources and receivers that are effectively located in an upper half-space. The resulting gathers are therefore free of surface-related multiples. The specifics of the modeling procedure are as follows:

- The model is extended at all four sides, to allow for a smoothing of the model that is needed for the absorbing boundary conditions. The resulting model grid measures 550 by 300 points with a spatial sampling interval ($\Delta x = \Delta z$) of 2m.
- The registration duration is 850ms with a time step of 0.4ms. In the resulting shot gathers, every tenth sample is selected, resulting in a sample interval of 4ms.
- 71 shot gathers are modeled with a shot spacing of 10m. The receiver spacing is also 10m. A fixed spread configuration with a total length of 640m is used.
- Two finite difference runs, with P-wave and S-wave sources are executed. The sources have a dipole characteristic; the receivers have a monopole characteristic. The source function is a shifted (to make it causal) 20Hz central frequency Ricker wavelet.

In order to appreciate the level of interference that will be present, the wavelet is converted to depth using half the average P-wave velocity (≈ 1500 m/s), and plotted

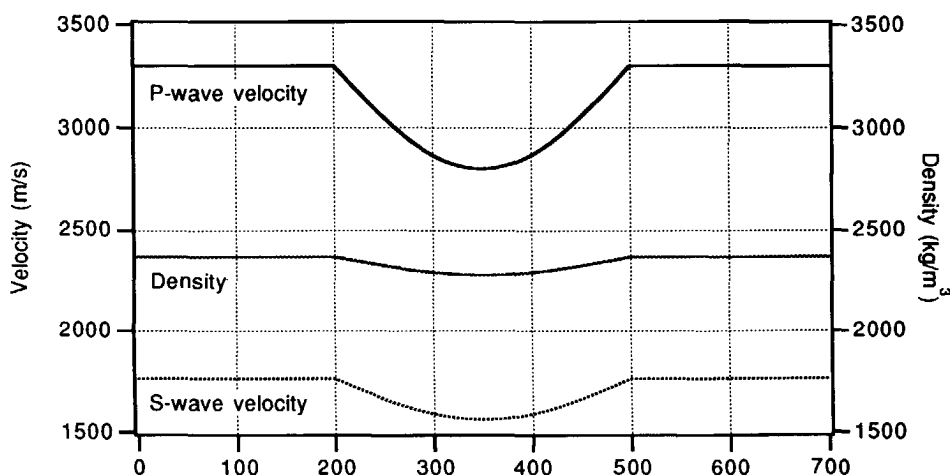


Fig. 7-12 The elastic parameters of the fourth layer as a function of the lateral position

on top of the model in Fig. 7-11. PP and SS shot gathers at shot locations of 150m and 350m (middle of the model) are shown in Fig. 7-13. Note the significant interference in the PP data. Zero-offsets sections for the PP and SS data are shown in Fig. 7-14.

Next, the data are reordered into CMP gathers and processed into the k_x - ω domain. With an interpolation in the k_x direction and, subsequently, an inverse Fourier transform, p - τ gathers with a ray parameter interval of 25.8×10^{-6} s/m are obtained. The final result consists of 41 CMP gathers (per reflectivity type) for mid-point positions ranging from 150 to 550m. These p - τ CMP gathers will be the input for the inversion scheme. For midpoint positions of 150 and 350m, the CMP gathers are shown in Fig. 7-15.

7.2.2 Inversion considerations

Each CMP gather is inverted for independently. For the PP data, a maximum ray parameter of 155×10^{-6} s/m is used, which corresponds to an angle of 25 degrees in the top layer. For the SS data, the same maximum ray parameter is used, which corresponds to an angle of 11 degrees in the top layer. The inversion starts at the left of the model ($x=150$ m) with a zero contrast initial model. The estimation result is used as the initial model for the next CMP, and so on, until the last midpoint at $x=550$ m is reached. The procedure is depicted in the flowchart of Fig. 7-16. Since the data are on the correct amplitude scale, no scaling parameters are included in the inversion. To possibly accommodate for the lateral velocity variations, 0th and 2nd order time shift parameters are incorporated with standard deviations of 5ms.

As in the previous example, average parameter values ($\langle \alpha \rangle$, $\langle \sigma \rangle$, $\langle \rho \rangle$) are supplied. The true and prior values (with corresponding standard deviations) of these

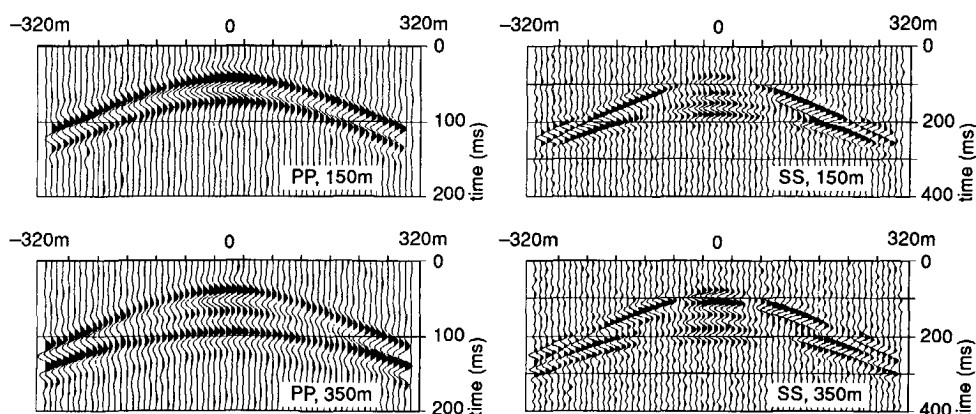


Fig. 7-13 PP and SS Shot gathers at two shot positions.

average quantities is given in Table 7-5. The prior information is laterally *invariant*, meaning that the lateral variations in the estimated model will *completely* be derived from the seismic data. Why the standard deviation of the average P-wave velocity is taken so small, will be addressed later.

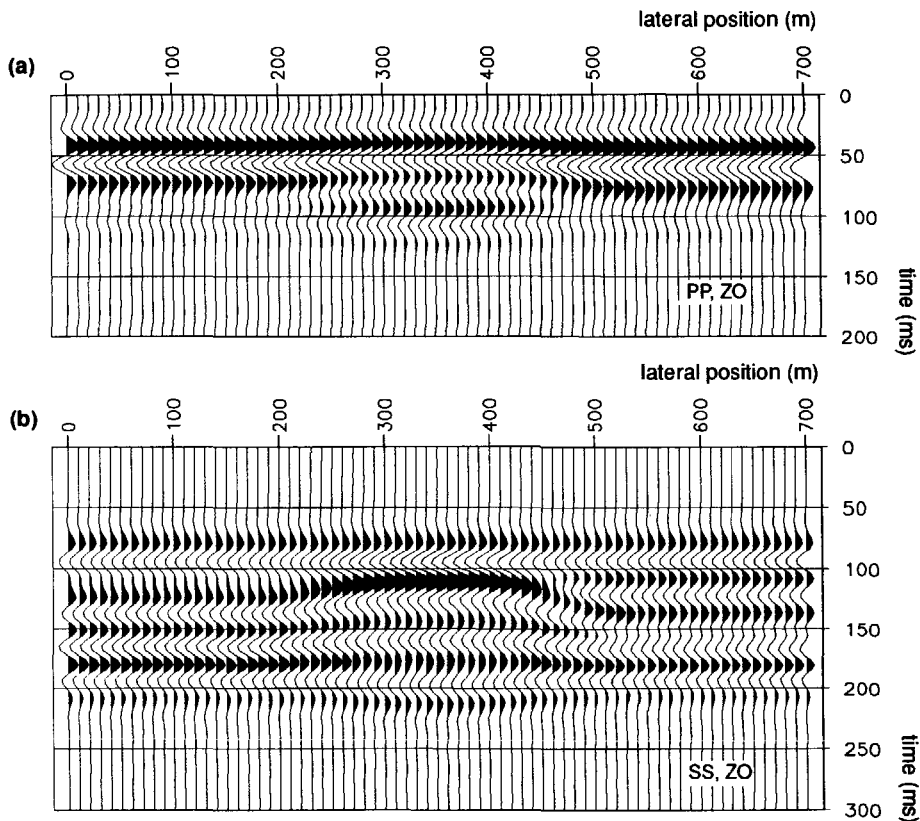


Fig. 7-14 Zero offset sections. (a) PP data. (b) SS data. Note the significant increase in resolution, as compared to the PP data.

Table 7-5 True and prior values with the corresponding standard deviations for the targetzone averaged elastic parameters. The true values for the averages vary laterally, but the prior values are kept constant.

| Prior item | unit | True value | Prior value | StdDev |
|--------------------------|--------------------------|------------|-------------|--------|
| $\langle \alpha \rangle$ | m/s | 3140-3240 | 3190 | 10 |
| $\langle \sigma \rangle$ | — | 0.33-0.34 | 0.34 | 0.05 |
| $\langle \rho \rangle$ | 10^{-3} kg/m^3 | 2.32-2.33 | 2.33 | 0.05 |

Since the model is reasonably consistent with the empirical relations (Gardner and Mudrock), both are used with a standard deviation of the error in the “predicted” P-wave velocity of 200m/s.

7.2.3 Inversion results for PP data only

The inversion is first performed on the PP data only, and results are shown in Fig. 7-17. The results are of reasonable quality. The estimated depth model of Fig. 7-17a is not very accurate, because the errors in the estimated P-wave velocities: The inversion “senses” the traveltimes quite accurately, but with wrong velocities the wrong depths will result. Overall, the results for the P-wave velocity and the density are the most accurate. The errors in the S-wave velocities are larger. It is

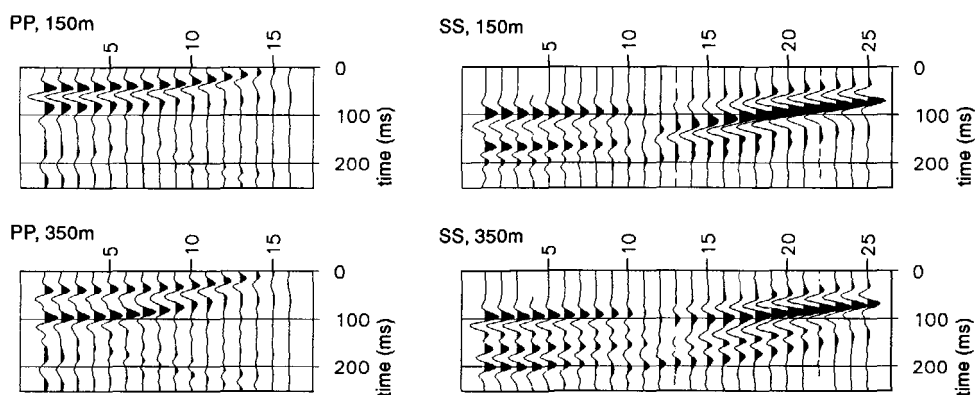


Fig. 7-15 CMP p - τ gathers (single-sided) at midpoint positions of 150 and 350m. The ray parameter increment is $\Delta p = 25.8 \times 10^{-6}$.

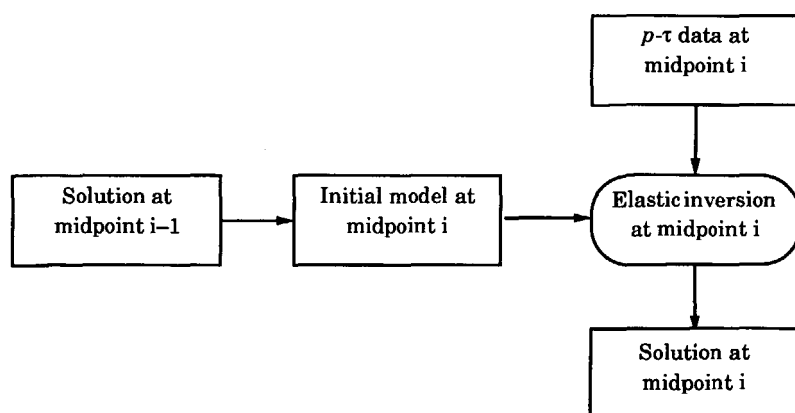


Fig. 7-16 Iterative elastic inversion per CMP.

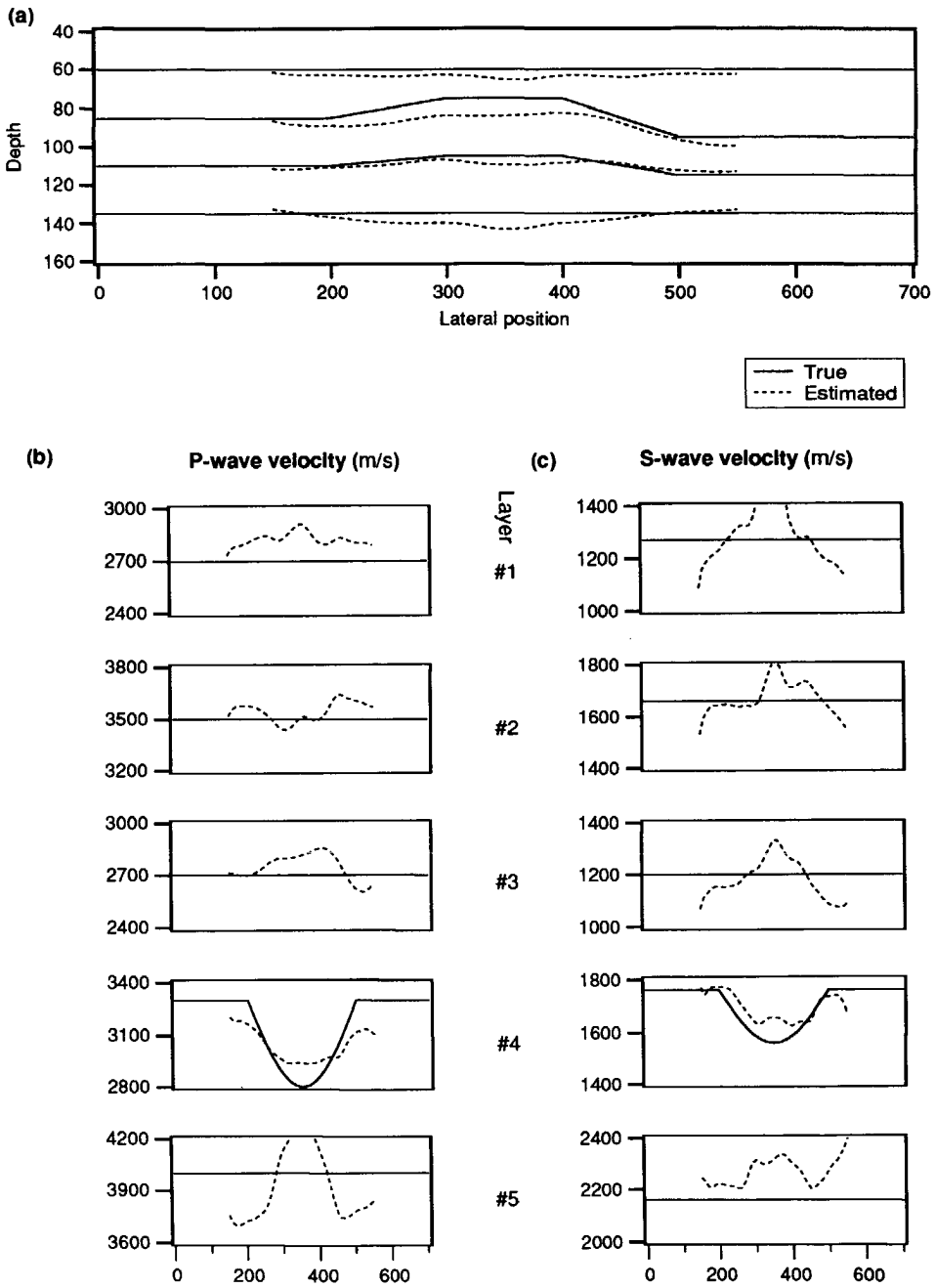


Fig. 7-17 Comparison of true and estimated parameters for PP-only inversion. **(a)** Depth model. **(b)** P-wave velocity. **(c)** S-wave velocity.

apparent that the large errors in the P-wave velocity and density of the fifth layer are correlated with the lateral variation of the structure of the model and/or the lateral parameter variation in the fourth layer.

This effect is probably due to the velocity variations in the model. Consider e.g. the reflections from the bottom interface belonging at midpoint $x=350\text{m}$ (the middle of the model). The normal incidence rays travel through a medium with a P-wave velocity in the fourth layer of 2800m/s . The oblique rays travel through a medium with a higher P-wave velocity. This is sensed by the inversion, and consequently,

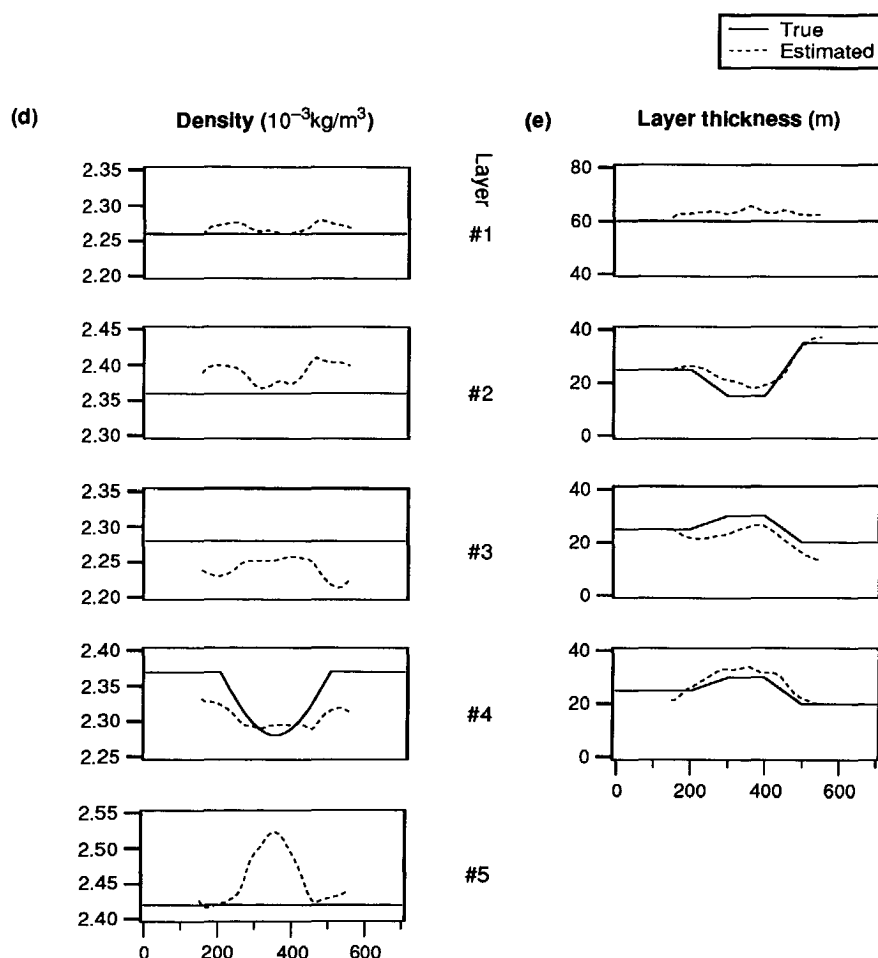


Fig. 7-17 (Continued) Comparison of true and estimated parameters for PP-only inversion. **(d)** density. **(e)** Layer thickness.

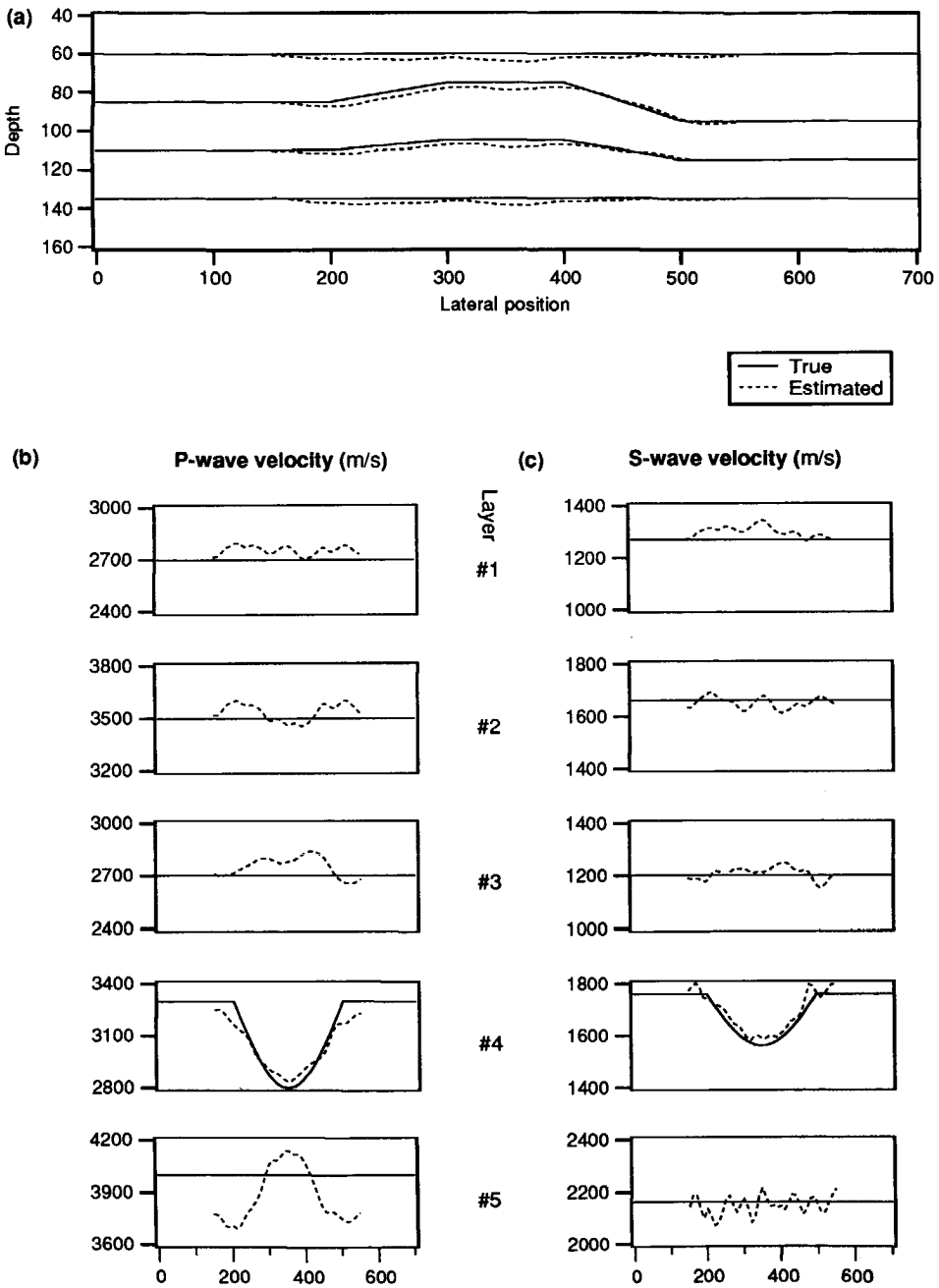


Fig. 7-18 Comparison of true and estimated parameters for PP&SS inversion. **(a)** Depth model. **(b)** P-wave velocity. **(c)** S-wave velocity.

the velocities are estimated to high. At the edges of the “dome” this effect works in the opposite direction. When performing the inversion with a larger standard deviation of $\langle\alpha\rangle$, e.g. 100m/s instead of 10m/s, all velocities show the same bias as the one of layer #5 in this example. Forcing the velocities down by the small standard deviation has apparently succeeded for all layers but the fifth one. As will appear later, when the PP&SS results are shown, the S-velocities are not affected so much. This is because a) a smaller range of angles is used and b) the drop in the S-wave velocities is only half the drop in the P-wave velocities.

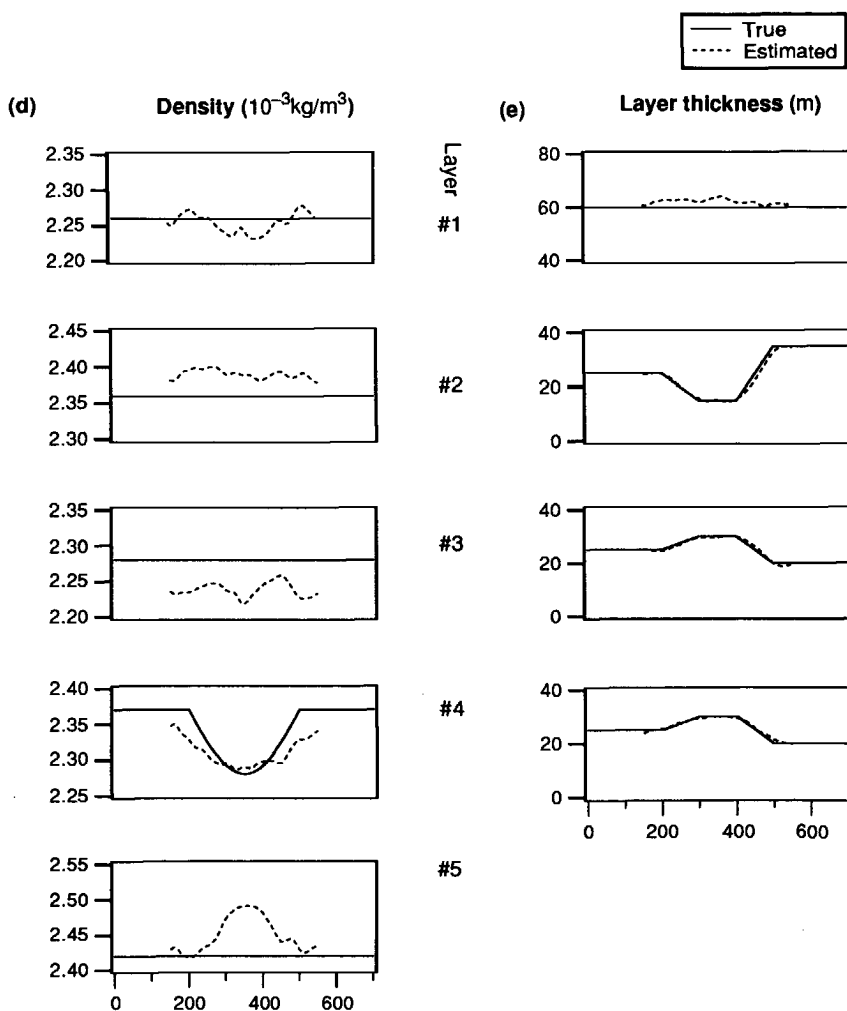


Fig. 7-18 (Continued) Comparison of true and estimated parameters for PP&SS inversion. (d) density. (e) Layer thickness.

7.2.4 Inversion results for a combination of PP and SS data

Next, the inversion is attempted with a combination of PP and SS data. The corresponding results are shown in Fig. 7-18a-e. The overall inversion results have improved significantly. As expected, the results for the S-wave velocities have improved dramatically. There are still some minor errors in the estimated depth model, but the errors are correlated, as appears from the very accurate results for the layer thicknesses as shown in Fig. 7-18e.

7.2.5 Conclusions

In conclusion, it can be stated that the *unstabilized* inversion (i.e. with a large standard deviation on the average P-wave velocity) has shown a considerable sensitivity to lateral changes in the layer velocities and the structure. Some force had to be applied to bring the inversion results back on the correct track. But since this force (a very small standard deviation for the targetzone averaged P-wave velocity) was applied in a laterally uniform manner, the inversion results, even for PP only, are still satisfactory.

A better way to stabilize the results is to tie the elastic parameters (per layer) to the lithology via the economically important porosity parameter. An example of this technique will be shown in the next section.

7.3 Litho-elastic inversion example

In this section an example will be discussed that uses the lithology based prior information. The model that is chosen consists of a sandstone reservoir, embedded in shale, see Fig. 7-19. On the left side of the model the reservoir is water filled, whereas on the right side it is gas filled. The porosity, however, is significantly lower in the gas-filled part of the reservoir. As will appear later, this difference in porosity results in practically *equal* acoustic impedances for the water- and gas filled parts of the reservoir. Hence, discrimination will be completely based on the AVO behavior.

The reservoir is assumed to be located at a depth of about 2km. The elastic parameters of the three lithotypes are chosen close to the values that are predicted by the lithologic relations of Section 6.5.2 (maximum deviation $\approx 5\%$). The values of the required lithologic and fluid parameters are given in Tables 6-1 and 6-2 and the resulting dependence of the elastic parameters on the porosity is shown in Fig. 6-6.

To facilitate the elastic modeling and the subsequent processing, the target zone is rotated so that its lower boundary becomes horizontal, see Fig. 7-20. The acquisition surface is chosen 75m above the first target boundary, which has a little "bump" in the middle. The transition from water to gas in the reservoir sand is modeled as a stepfunction in the elastic parameters at $x=350\text{m}$. As can be seen, the small decrease of the P-wave velocity is accompanied by a small increase of the density, thus causing a practically constant acoustic impedance over the transition.

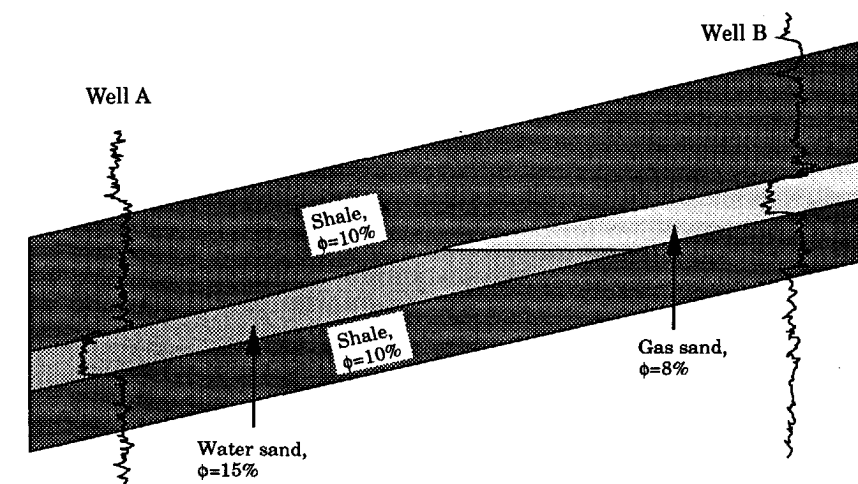


Fig. 7-19 Sandstone reservoir embedded in shale. On the left side, the reservoir is water filled; on the right side, it is gas filled.

Laterally coherent parameter fluctuations are superimposed on the elastic model by adding a properly scaled noise realization, which is shown in Fig. 7-21. The noise realization is multiplied by a factor 200 and added to the gridded P-wave velocity model. Since the amplitudes in the original noise realization are clipped to the interval $[-1, 1]$, the P-wave velocity fluctuations lie between -200 and 200m/s . The same is done for the S-wave velocity and the density, but now using a factor

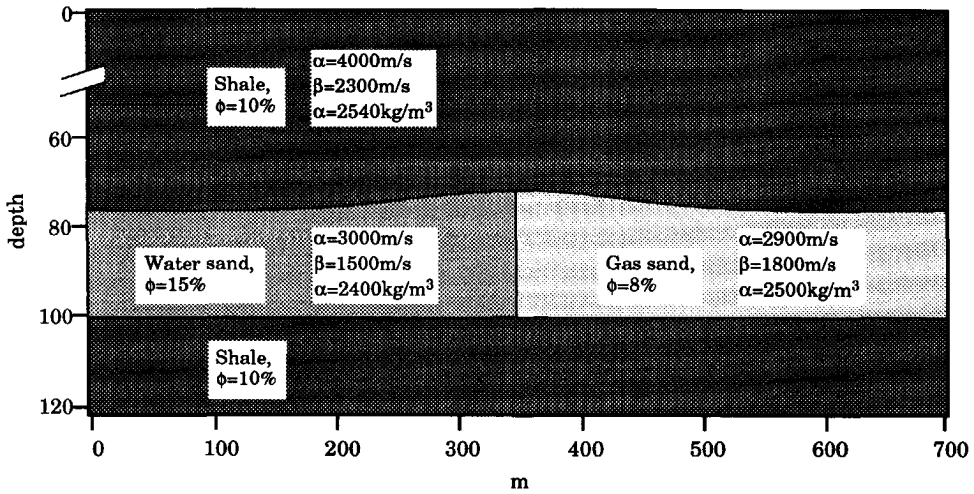


Fig. 7-20 The elastic model that is used for the finite difference modeling.

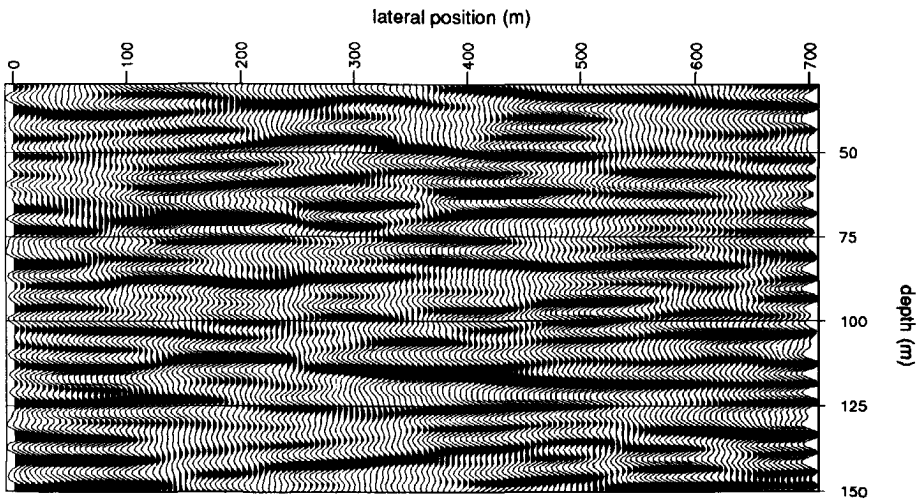


Fig. 7-21 Laterally coherent noise realization that is used for the elastic parameter perturbations.

100. The resulting elastic parameter logs at $x=100\text{m}$ are shown in Fig. 7-22. No parameter fluctuations are superimposed on the first 30m of model, so that the sources are located in a homogeneous medium. This allows for an easy subtraction of the direct wave, which is discussed in Section 7.3.2. Although it is not expected that these fluctuations will have a large influence on the modeled seismic data, they do bring the elastic model closer to reality.

7.3.1 Modelling

The elastic modeling procedure is similar to the one described in the previous section. At the surface, shot gathers are modeled with pure P-wave sources and pure P- and S-wave receivers that are effectively located in an upper half-space. Therefore, the resulting shot gathers are free of surface-related multiples. The specifics of the modeling procedure are as follows:

- The model is extended at all four sides to allow for a smoothing of the edges which is needed for the implementation of the absorbing boundary conditions. The resulting model grid measures 1100 by 600 points with a spatial sampling interval of ($\Delta x = \Delta z$) 1m.

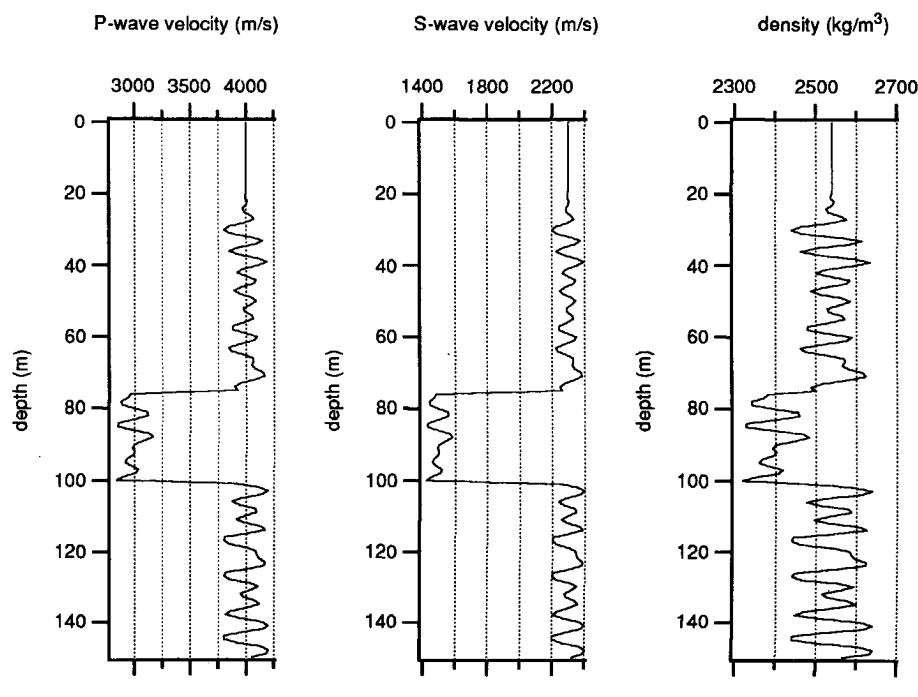


Fig. 7-22 The elastic parameters at $x=100\text{m}$. The same noise realization (with a different scaling) is used for the three parameter types.

- The registration duration is 180ms with a time step of 0.2 ms. For the registration, every twentieth sample is selected, resulting in a sample interval of 4ms.
- 66 shot gathers (for each reflectivity type, PP and SP) are modeled, with a shot spacing of 16m and a receiver spacing of 8m. A fixed-spread configuration with a length of 512m is used.
- The P-wave sources that are used have a dipole characteristic; the receivers (both for P and S) have a monopole characteristic. The source function is a 30Hz central frequency Ricker wavelet, see Fig. 7-23.

7.3.2 Processing

Since the receivers are located on the same level as the P-wave dipole sources, in theory there should be no direct wave recorded. In the PP gathers the direct wave has indeed a negligible amplitude. The PP zero-offset section is shown in Fig. 7-24. Note that there is indeed no visible difference in normal incidence reflectivity between the water sand at the left and the gas sand at the right. In the converted SP gathers (P-wave sources, S-wave receivers), the direct wave is very strong in a few traces around the source. This modeling artifact is removed by subtracting the corresponding traces from a shot gather resulting from an identical modeling experiment using a homogeneous medium with the elastic parameters of the first layer.

The so-obtained shot gathers are reordered into CMP gathers with a midpoint spacing of 16m. The CMP gathers contain 64 traces with a receiver spacing of 8m so that the maximum source-receiver offset is 256m. CMP gathers at midpoint locations of 150m (water sand) and 550m (gas sand) are shown in Fig. 7-25.

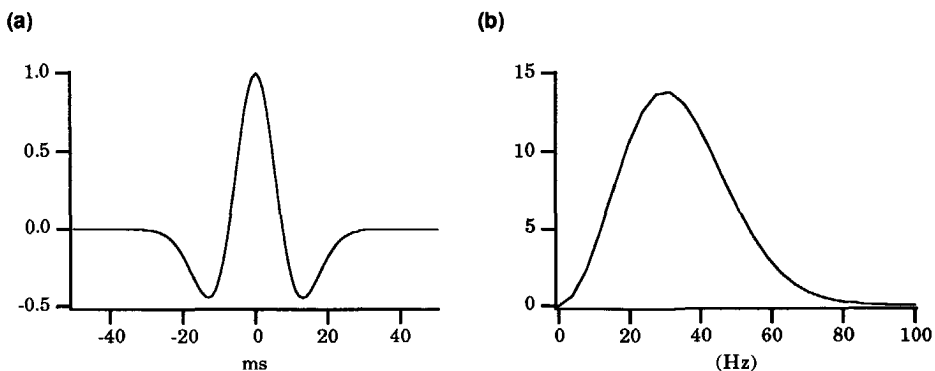


Fig. 7-23 30Hz central frequency Ricker wavelet that is used for the modeling. (a) Time domain (for the elastic modeling, the wavelet is actually shifted to make it causal). (b) Amplitude spectrum.

In order to get a sufficiently small ray parameter sampling interval, the CMP gathers are augmented with zero traces to a total of 256 traces. Next, they are transformed into the k_x - ω domain. With an interpolation in the k_x direction and, subsequently, an inverse temporal Fourier transform, p - τ gathers with a ray parameter sampling interval of 5.68×10^{-6} s/m are obtained. The final result consists of 42 CMP gathers (for both reflectivity types) with midpoint locations

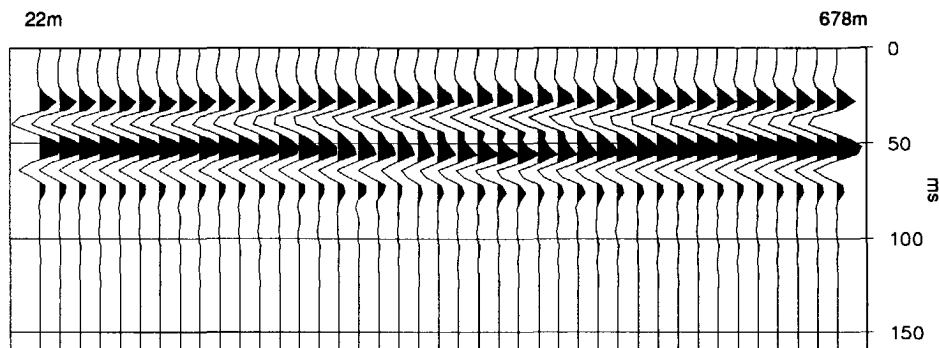


Fig. 7-24 Zero offset section of the PP data. There is little lateral variation in the reflectivity behavior.

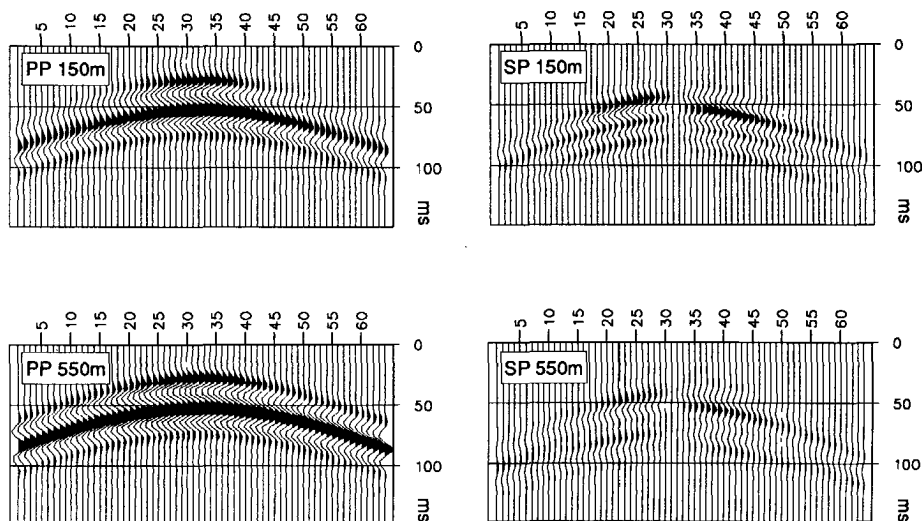


Fig. 7-25 CMP gathers at some midpoint locations, plotted on the same amplitude scale. The receiver spacing is 8m. Note that the amplitudes in the SP gather at 550m are significantly lower as compared to those at 150m, because of the smaller S-wave velocity contrast.

between 22 and 678 m and a midpoint spacing of 16m. For midpoint locations at 150 and 550m, the p - τ CMP gathers are shown in Fig. 7-26

7.3.3 Inversion considerations

The inversion is first attempted using only PP data. The maximum ray parameter that is used is $136 \times 10^{-6} \text{ s/m}$ (trace #25 in Fig. 7-26), which corresponds to an incident angle in the upper layer of 33° . The elastic inversion is performed per lateral position and starts at the left of the model (well A) with a zero-contrast initial model. As pictured in Fig. 7-16, the estimated model of the previous inversion is used as the initial model for the current inversion. The inversion proceeds in this fashion until the right-hand side of the model is reached (well B).

As mentioned, the porosity relations are used in this example as prior information. It is assumed to be known from well data, that the reservoir is embedded in shale at the starting position. Regarding the lithotype of the reservoir, the inversion is attempted twice, once assuming a water sand and once assuming a gas sand. It is expected that the residuals will indicate which assumption is the right one, depending on the lateral position. The standard deviation for the P-wave velocity relation is set to 100m/s. For the S-wave velocity and the density, it is set to respectively 50m/s and 50 kg/m^3 . These values agree well with the actual deviations of the elastic parameters with respect to these relations.

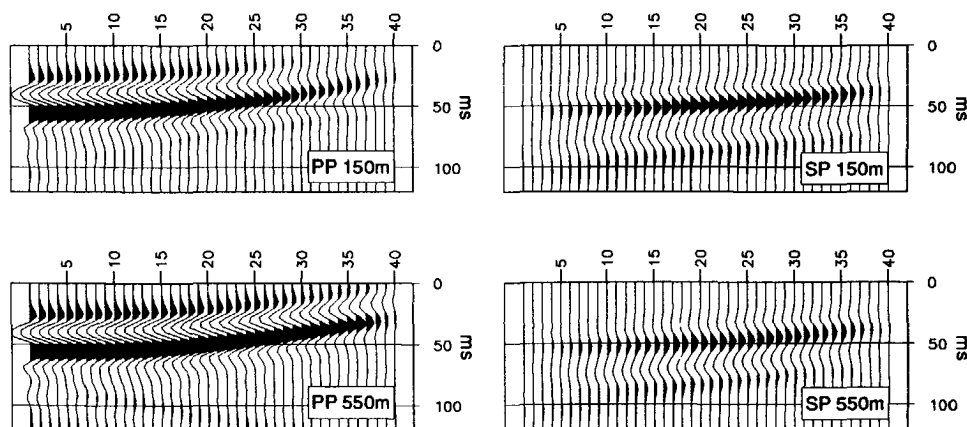


Fig. 7-26 p - τ CMP gathers at some midpoint locations, plotted on the same amplitude scale. The trace spacing (ray parameter increment) is $\Delta p = 5.68 \times 10^{-6} \text{ s/m}$.

Besides the lithological prior information, the targetzone averages of the P-wave velocity, Poisson's ratio and density are still used as prior information. The resulting three mismatch terms are part of the second element of the total residual vector of equation (6-22). Table 7-6 gives an overview of the related parameters. As described in Section 6.5.1, the lithological relations are incorporated *per layer*, and the resulting mismatch terms (nine in this example) constitute the third element of the total residual vector of equation (6-22).

The incorporation of the time-shift robustness parameters (see Section 6.4.1) proved to be essential for this experiment, since the traveltimes in the p - τ gathers that are used as input for the inversion appeared to be 2-5ms in error, when compared to p - τ modeled gathers. Why these errors are present is not known yet, but fortunately, it can be demonstrated now, that the inversion is able to cope with such deviations.

Table 7-6 True and prior values with the corresponding standard deviations for the targetzone averaged elastic parameters. The true values for the averages change at the water to gas transition, but the prior values are kept laterally invariant.

| Prior item | unit | True (left) | True (right) | Prior value | StdDev |
|------------------------|-------------------|-------------|--------------|-------------|--------|
| $\langle\alpha\rangle$ | m/s | 3667 | 3633 | 3600 | 50 |
| $\langle\sigma\rangle$ | — | 0.28 | 0.23 | 0.25 | 0.05 |
| $\langle\rho\rangle$ | kg/m ³ | 2490 | 2530 | 2500 | 100 |

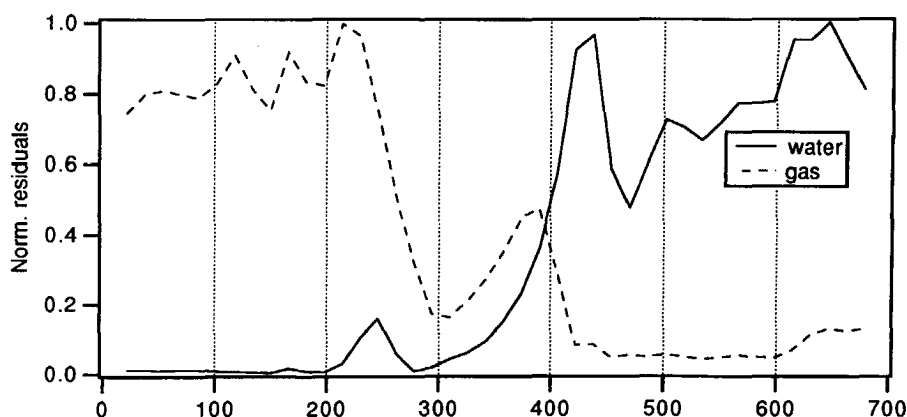


Fig. 7-27 Energy in the lithology-relations mismatch, for the lithotypes water sand and gas sand. The transition from water sand to gas sand is located at 350m.

As mentioned, the inversion is attempted once assuming a water sand, and once assuming a gas sand for the reservoir layer. As shown in equation (6-22), the residual vector consists of three parts: data mismatch, "standard" prior relations mismatch and lithology mismatch. In general, the total energy in the residuals consists mainly of the data mismatch. Unless the lithology relations are *very* strictly imposed (by using very small standard deviations), the total energy will be

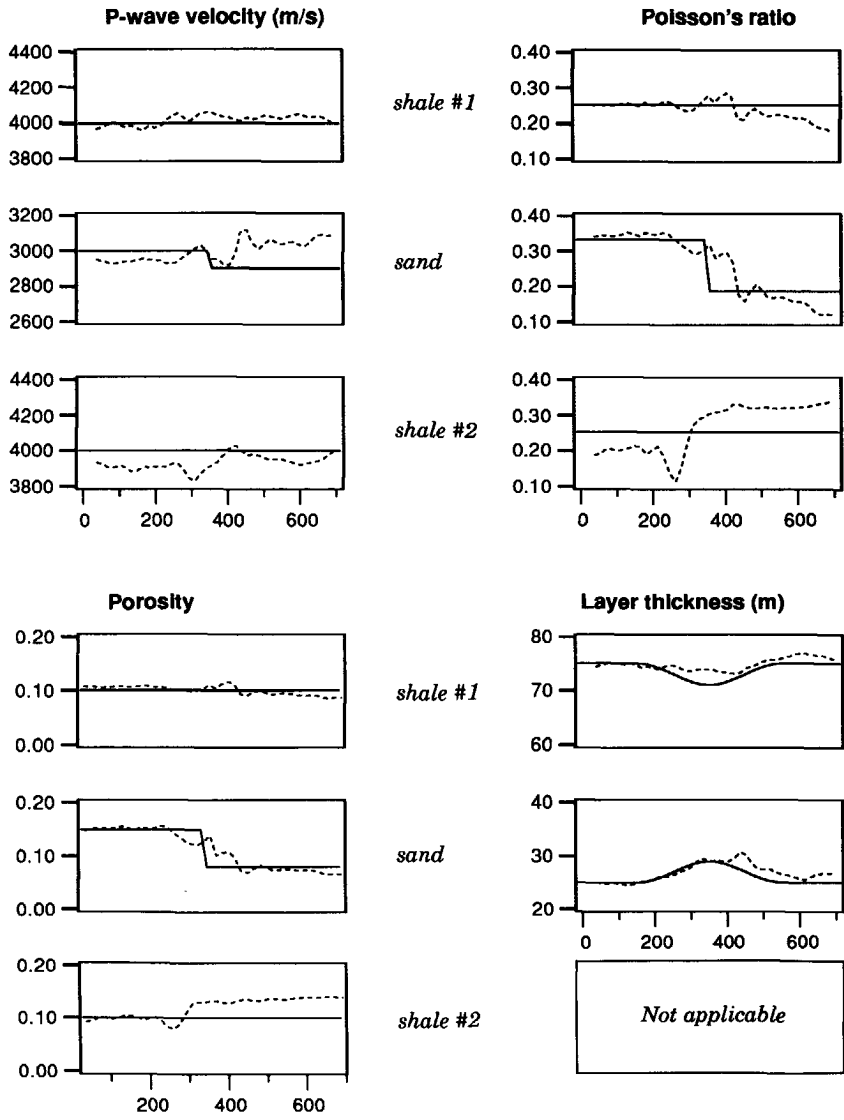


Fig. 7-28 The estimation results using PP reflectivity only.

quite insensitive to changes in lithotype. Therefore, in order to achieve an optimal discrimination between the lithotypes (water sand and gas sand, in this example), the energy in the *lithology mismatch* is used as a measure for the likelihood of a particular lithotype assumption.

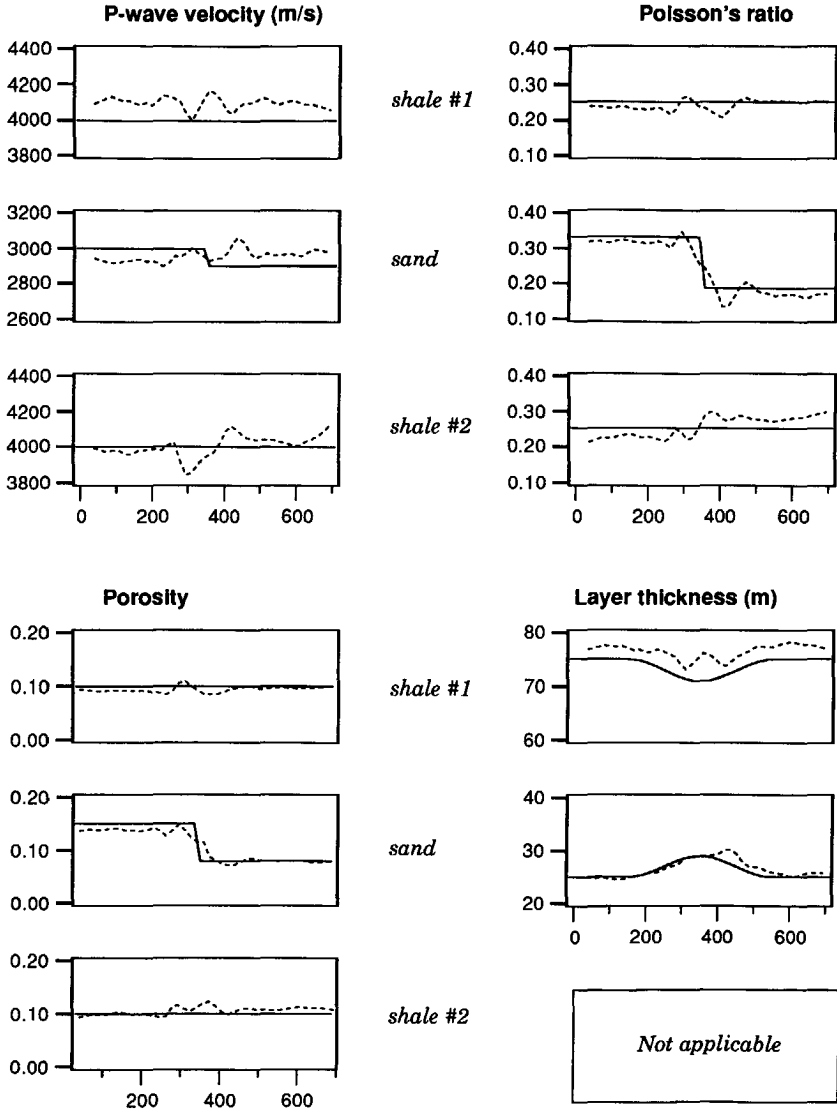


Fig. 7-29 The estimation results using a combination of PP and SP reflectivity.

7.3.4 Inversion results for PP data only

The results for the energy in the lithology mismatch are shown in Fig. 7-27. The discrimination between the two lithotypes can clearly be observed. When using the porosity relations for the water sand, the energy is lowest at the left, while at the right, the energy for the gas sand is lowest. The exact transition from water to gas occurs at 350m, which agrees well with the observed behavior of the residual curves.

Having established the fact that the water sand is present at the left and the gas sand is present at the right, with a transition at about 350m, the estimated model can be obtained: Up to 350m, the results from the water sand inversion run are selected, while after 350m, the results from the gas sand run are selected. The estimated and true values for the P-wave velocity, Poisson's ratio, porosity and layer thickness are shown in Fig. 7-28. As can be seen, the results are quite accurate. The transition from water sand to gas sand is nicely represented by the drop in the estimated Poisson's ratio of the reservoir sand. Also the porosities are well retrieved. The aforementioned moveout errors, that are partly accounted for by the robustness parameters are probably the major cause of some of the inaccuracies in the results.

7.3.5 Inversion results for a combination of PP and SP data

The inversion is also performed using a combination of PP and SP data. The maximum ray parameter for the SP data that is used is also 136×10^{-6} s/m. The same procedure as for the PP-only case is followed. Making use of a display like the one of Fig. 7-27 (not shown here), the discrimination between the two lithotypes improves somewhat. The results for the estimated parameters are shown in Fig. 7-29. Especially, the results for the Poisson's ratios have improved. The porosity of the third layer (shale#2) is also correctly estimated now. The results for the layer thickness of the first layer are slightly biased. This is again attributed to the moveout errors. Note that the small step in the P-wave velocity is still not retrieved.

7.3.6 Conclusions

The incorporation of the seismic-lithology relations has made it possible to obtain not only the elastic parameters, but also the lithology from PP-only multi-offset data. An excellent discrimination between a gas sand and a water sand lithology was achieved. Since the *normal incidence* PP reflectivity is practically invariant for this model, this discrimination has to be based on the offset dependent behavior of the reflectivity. Using a combination of PP reflectivity and converted SP reflectivity (P sources, S receivers), a worthwhile improvement of the results was obtained.

In this thesis, a inversion strategy for multi-offset seismic data is described. Rather than using the shot gathers at the surface in an inversion for the whole subsurface, a target oriented approach is proposed. The necessary pre-processing of the possibly multi-component shot gathers is handled by the pre-processing / redatuming modules of the DELPHI scheme, see Fig. 2-1 on page 12: Decomposition into P- and S-waves, surface related multiple elimination, macro model estimation and multi-offset downward extrapolation.

The DELPHI redatuming method is designed to handle laterally inhomogeneous macro models. The new datums are chosen close to, and parallel to the local layering of the target zone. After reordering into Common Midpoint (CMP) gathers, the data in one CMP can be considered to correspond to a locally one-dimensional medium. In the case that multi-component data is available, the decomposition yields PP, SP, PS and SS shot gathers. The multi-shot redatuming is executed per reflectivity type, to yield again, after redatuming, four target related CMP gathers per midpoint.

For the inversion, the targetzone is locally parameterized with a stack of homogeneous elastic layers. The layer thicknesses are part of the parametrization. Any combination of the four reflectivity types can *simultaneously* be inverted. This includes a single reflectivity type, e.g. PP-only. For an efficient and accurate inversion, the data are processed into the plane wave (p - τ) domain. The inversion makes use of iterative forward modeling to match modeled data to the observed data. The forward modeling is done by a recursive elastic reflectivity algorithm.

For the elastic inversion described here, the mismatch function is a sum of squares and is minimized by a corrected Gauss-Newton method. Since the forward model is nonlinear in the parameters, local minima can exist. As was shown in Section 3.6.2, the behavior of the reflectivity as a function of the model parameters is reasonably linear and is not likely to cause local minima. The full-waveform mismatch function is, however, a strongly nonlinear function of the velocities. Changing the velocities will change the traveltimes in the multi-offset data. This will cause local extremes in the energy of the mismatch between modeled and actual data when

peaks and troughs “shift through each other”. Starting with an initial travelttime model that is close enough to the actual minimum is the best solution to prevent ending up in a local minimum. Such a model can be obtained from a preceding poststack inversion, see Section 6.1.2.

The second problem which geophysical inverse problems usually suffer from, is that the mismatch function is essentially flat in one or more directions around its minimum. These ill-resolved directions introduce uncertainties in the associated parameters. This problem is addressed by using prior information to stabilize the inversion.

8.1 Elastic prior information

The Bayesian inversion technique is applied, to effectively stabilize the inversion through the use of prior information. Uncertainties in prior information and data (noise) are treated in a statistically consistent manner.

First of all, targetzone averaged parameters (from the macro model) are used as prior information, to establish the absolute “level” of the parameters. In addition, generally applicable empirical relations between the elastic parameters (Gardner, Mudrock) could be used. However, we prefer the specification of lithologic relations per lithotype (“litho-stratigraphic inversion”).

Based on results employing solely elastic prior information, the following can be concluded:

- When using PP-only data, the P-wave velocities and densities are estimated best. The S-wave velocity is less accurately estimated. Important though, is that anomalously low Poisson’s ratios, which are assumed to be an indication of gas fill, are usually well retrieved.
- Using a combination of PP and SS data, the estimation results for all parameters improve considerably. Now, the S-wave velocity is the best resolved parameter.
- The parametrization in terms of layers makes it possible to retrieve the layer parameters, even in the case of thin layers and strong interference. When using a gridded medium representation, this would not be possible.

Still, experience of the author with many types of models indicates that problems can be expected when inverting field data with merely *elastic* stabilization. Amplitude errors, errors in the wavelet and small contrasts are amongst the factors that will hamper a successful inversion of field data. Therefore, a stronger stabilization by specifying lithologic relations *per* layer is proposed.

8.2 Lithologic prior information

In mature exploration areas, lithologic information about the target layers is generally available. In such a case, a better way to stabilize the inversion is by making use of lithology-based prior information; the more so, because the lithology is what one is ultimately interested in. Because the elastic parameters are sensitive to the porosity, it is a logical step to include the porosity in the parametrization. The prior information, which makes the results for both the elastic parameters *and* the porosity well defined, consists of empirical or theoretical relations between the porosity and the elastic parameters.

For different lithologies, different porosity relations are used. This makes it possible, under certain conditions, to determine the most likely lithotype of a certain target layer, together with its porosity. Here, a lithotype denotes not only the lithology, but also the type of fluid fill. Even in the cases of PP-only data, where stabilization is most needed, this procedure is expected to provide the information one is most interested in: The pore fill (fluid or gas) and the porosity.

8.3 Discussion and recommendations

The following aspects are of importance when developing a target oriented elastic inversion method:

- Choice of parametrization.
- Choice of stabilization.
- Choice of data and associated forward model.

Regarding the parametrization, the author feels that it is a necessary choice to indeed parametrize the targetzone in terms of homogeneous *layers*, rather than using a gridded representation. When using the geology-based layered parametrization, not only thin layers can be resolved, but it is also possible to specify different prior information *per layer*, both of which are not possible with gridded inversion. It is true that gridded inversion imposes no constraints on the model, but we know that the subsurface is predominantly layered, which should be made use of to constrain the solutions.

Regarding the stabilization, the inclusion of the porosity in the parametrization, together with relations between the elastic parameters and the porosity, can be seen as the optimal way to link the AVO information in the multi-offset data directly to the economically important lithology parameters, pore fill and porosity. Since the porosity relations (theoretical or empirical) are implemented with an associated uncertainty (Bayesian inversion) the answers are not forced to exactly obey them.

Regarding the third item, choice of data and forward model, the preference for performing the inversion in the p - τ domain was largely based on grounds of computational efficiency.

However, there are two problems associated with p - τ data, that do not occur in an inversion of x - t data. Like the original shot gathers at the surface, the target related CMP gathers have a limited aperture. First of all, this limited aperture causes truncation artifacts in the p - τ data, that, due to their coherent character, can be quite harmful to the inversion result. Dobbs et al. (1990) devoted a paper to this subject.

Secondly, there is a problem because of the fact that the data in a certain offset range does not correspond to data in a certain ray parameter range. The problem is illustrated for a two-layer model in Fig. 8-1. For the maximum source-receiver offset of 200m, the incident angle at the first reflector is 45° (point A, $p = 0.71 \times 10^{-3}$ s/m), which is beyond the critical angle at 30° (point C, $p = 0.50 \times 10^{-3}$ s/m). At the maximum incident angle on the second reflector, the corresponding ray parameter is smaller, namely $p = 0.29 \times 10^{-3}$ s/m (point B).

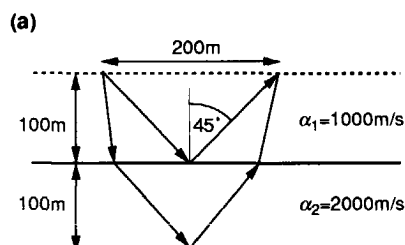
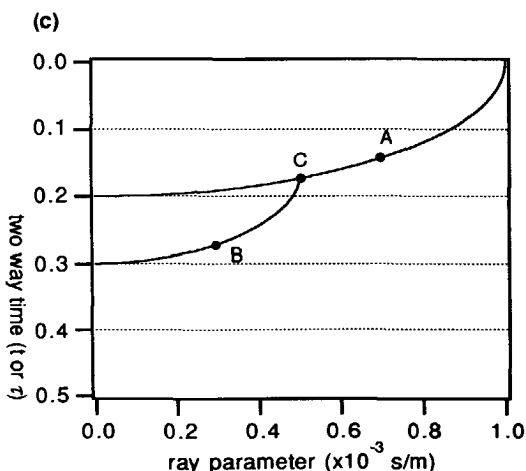
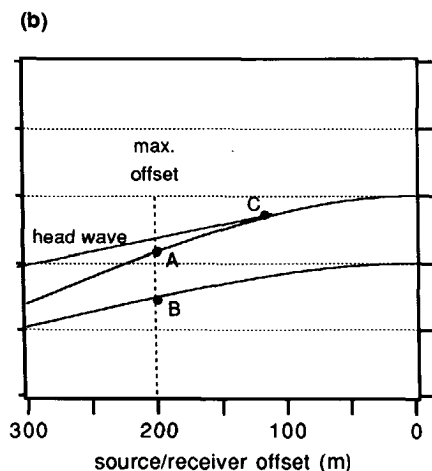


Fig. 8-1 For the two reflectors, a certain offset range (200m) corresponds to different ranges of ray parameters. **(a)** Model with two reflectors. **(b)** x - t traveltimes. The maximum offset is 200m. The head wave starts in point C. **(c)** p - τ travel times. The part between B and C of the lower reflector is not present in the x - t data.



The inversion assumes a certain range of ray parameters that is necessary equal for all events. Going beyond $p = 0.29 \times 10^{-3} \text{ s/m}$ is therefore not possible, because the second reflector is simply missing in the p - τ data. Due to the effects of the limited aperture, the full-waveform p - τ data will already be inaccurate for even smaller ray parameters. In any case, the valuable postcritical information of the first reflector has to be discarded.

This discrepancy between "p-range" and "x-range" causes also problems for the strong twice-converted events that are generally present in the SS data. In this case, for a ray parameter close to the reciprocal of the P-wave velocity of a layer, the primary SS reflections will correspond to medium large offsets, whereas the twice-converted waves correspond to very large offsets, and are therefore not registered.

A solution to this problem might be to include a limited aperture filter in the forward modeling, see Dobbs et al. (1990). However, an accurate implementation requires the modeling of many ray parameter traces, which nullifies part of the advantages of p - τ inversion.

Doing the inversion in the x - t domain would eliminate these problems. The modeling becomes more complex now, because of the fact that the wavenumber integral of equation (4-2) requires special attention to prevent wrap-around of events in the lateral direction. Since the x - t modeling will typically take much more time, it becomes important to develop a method to calculate the derivatives of the objective function with respect to the layer parameters directly, rather than using a finite difference procedure, which takes many modelling steps.

Appendix A Scattering in terms of particle displacements and Lamé potentials

Many authors, e.g. Bortfeld (1961), Cervený and Ravindra (1971) and Aki and Richards (1980), define the scattering coefficients of plane waves at a horizontal interface between two homogeneous isotropic elastic media in terms of *particle displacements*. This is in accordance with the original work of Zoeppritz (1919). In this appendix, the relation between the particle-displacement coefficients and the potential coefficients, which are used in this thesis, will be derived.

In the definition of the scattering coefficients in terms of particle displacements, there is an arbitrariness in the choice of the positive direction. All references mentioned above, fortunately adhere to the same definition which is pictured in Fig. A-1.

A1 Particle motion for homogeneous and inhomogeneous waves

The velocity v is the time derivative of the particle displacement u , so with transform pair (3-40) it follows:

$$U(p, z, \omega) = \frac{1}{i\omega} V(p, z, \omega). \quad (\text{A1})$$

Considering only a downgoing or upgoing P-wave, it follows from the composition relations (3-37) and (3-38) that the corresponding particle displacement is given by:

$$U_{\Phi}^{\pm} = \frac{\Phi^{\pm}}{i\omega\rho} \begin{pmatrix} p \\ \pm q_p \end{pmatrix}. \quad (\text{A2})$$

Likewise is the particle displacement from a downgoing or upgoing S-wave given by:

$$U_{\psi}^{\pm} = \frac{\psi^{\pm}}{i\omega\rho} \begin{pmatrix} \mp q_s \\ p \end{pmatrix}. \quad (\text{A3})$$

According to equation (3-26), a downgoing or upgoing P-wave is represented in the horizontal slowness - frequency domain by:

$$\Phi^{\pm}(p, z, \omega) = A_{\Phi}^{\pm} e^{\mp i\omega q_p z}. \quad (\text{A4})$$

For homogeneous waves, see Section 3.3.3, the vertical slowness is a positive real constant. Consequently, (A4) reads in the space - time domain:

$$\begin{aligned} \phi^{\pm}(x, z, t) &= A_{\phi}^{\pm} \exp[i\omega(t - px \mp q_p z)], \\ q_p &= \sqrt{1/\alpha^2 - p^2} \text{ and } p^2 \leq 1/\alpha^2. \end{aligned} \quad (\text{A5})$$

and the wavefronts (planes of constant phase) propagate in the direction of the slowness vector:

$$\mathbf{s}_{\Phi}^{\pm} = \begin{pmatrix} p \\ \pm q_p \end{pmatrix}. \quad (\text{A6})$$

For inhomogeneous P-waves, however, the vertical slowness is purely imaginary, leading to:

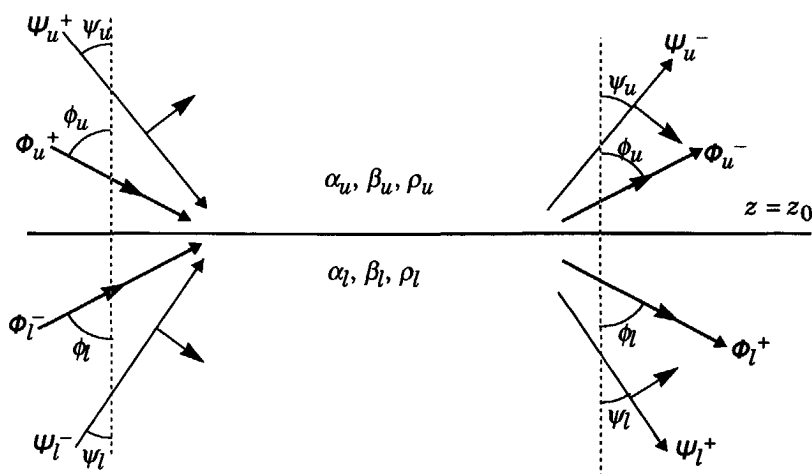


Fig. A-1 Scattering of plane waves at a horizontal interface between two elastic media. The direction of positive particle displacements is indicated with arrow type \rightarrow . The direction in which the wave propagates is indicated with arrow type \longrightarrow . The pictured longitudinal or transverse particle motion is only valid for propagating (homogeneous) waves.

$$\phi^{\pm}(x, z, t) = A_{\phi}^{\pm} \exp[\mp \omega z |q_p| + i\omega(t - px)],$$

$$q_p = -i\sqrt{p^2 - 1/\alpha^2} \text{ and } p^2 > 1/\alpha^2. \quad (\text{A7})$$

and the wavefronts propagate horizontally in the direction of the real part of the slowness vector:

$$\text{Re}\{\mathbf{s}_{\phi}^{\pm}\} = \text{Re}\left\{\begin{pmatrix} p \\ \pm q_p \end{pmatrix}\right\} = \begin{pmatrix} p \\ 0 \end{pmatrix}. \quad (\text{A8})$$

Comparing (A2) and (A6), it is clear that the particle motion for homogeneous P-waves is indeed in the direction of propagation. For an inhomogeneous P-wave, however, the nonzero q_p term in (A2) signifies particle motion in the z -direction, hence the wave is not purely longitudinal. Because q_p is imaginary, the motion in the z -direction is 90° out of phase with the motion in the x -direction, leading to an elliptical particle motion.

Mutatis mutandis, a similar reasoning applies for S-waves. A homogeneous S-wave propagates in the direction of the slowness vector

$$\mathbf{s}_{\psi}^{\pm} = \begin{pmatrix} p \\ \pm q_s \end{pmatrix},$$

$$q_s = \sqrt{1/\beta^2 - p^2} \text{ and } p^2 \leq 1/\beta^2. \quad (\text{A9})$$

and an inhomogeneous S-wave propagates horizontally in the direction of the real part of the slowness vector:

$$\text{Re}\{\mathbf{s}_{\psi}^{\pm}\} = \text{Re}\left\{\begin{pmatrix} p \\ \pm q_s \end{pmatrix}\right\} = \begin{pmatrix} p \\ 0 \end{pmatrix},$$

$$q_s = -i\sqrt{p^2 - 1/\beta^2} \text{ and } p^2 > 1/\beta^2. \quad (\text{A10})$$

The slowness of the homogeneous S-wave is indeed perpendicular to the direction of particle motion given by (A3). For an inhomogeneous S-wave, the nonzero q_s term in (A3) signifies particle motion in the x -direction, hence the wave is not purely transverse. Also for the inhomogeneous S-wave, the particle motion is elliptical.

A2 Potentials and particle-displacements

To arrive at a general relation between the two types of scattering coefficients, the coefficient T_{21}^+ from equation (3-30), that describes the transmission from an incident P-wave in the upper half-space to an S-wave in the lower half-space, will be

used as an example. In the following derivation, only *homogeneous* waves will be considered. The results, though, will be valid for both homogeneous and inhomogeneous waves.

Using (A2), the particle displacement of the incident P-wave in the upper half-space is given by:

$$U_{\phi_u^+} = \frac{\phi_u^+}{i\omega\rho_u} \begin{pmatrix} p \\ q_{p,u} \end{pmatrix}. \quad (\text{A11})$$

Using (A3), the particle displacement of the transmitted S-wave in the lower half-space is given by:

$$U_{\psi_l^+} = \frac{\psi_l^+}{i\omega\rho_l} \begin{pmatrix} -q_{s,l} \\ p \end{pmatrix}. \quad (\text{A12})$$

A representation of the incident P-wave in the slowness domain is given in Fig. A-1a. As can be seen there, the direction of positive particle displacement for the P-wave, as defined in Fig. A-1, is *coincident* with the direction $(p, q_{p,u})^t$ from (A11). However, for the transmitted S-wave, pictured in Fig. A-1b, the direction of positive particle displacement is *opposite* to direction $(-q_{s,l}, p)^t$ from (A12).

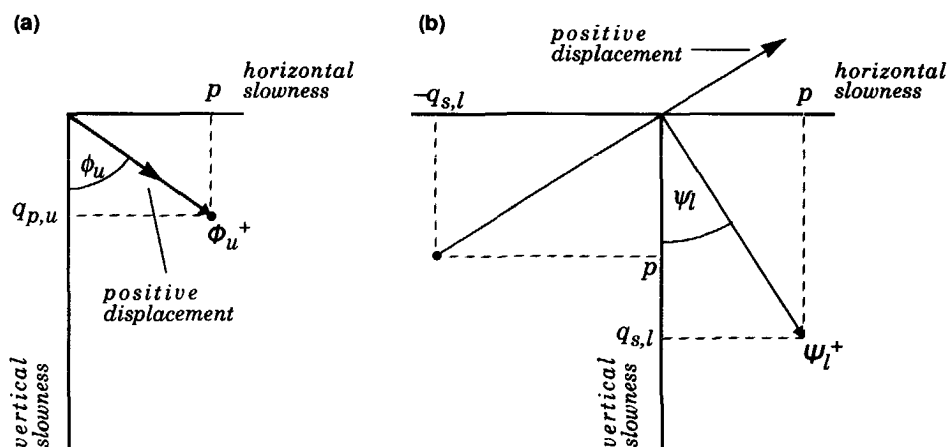


Fig. A-2 Wave representation in the slowness domain. The direction in which the wave propagates is indicated with arrow type \rightarrow . The direction of positive particle displacements is indicated with arrow type \rightarrow . (a) For the downgoing P-wave, the direction $(p, q_{p,u})^t$ in (A11), indicated by the dot (\bullet), coincides with the direction of positive particle displacement. (b) For the downgoing S-wave, the direction $(-q_{s,l}, p)^t$ in (A12), indicated by the dot (\bullet), is opposite to the direction of positive particle displacement.

Taking into account the sign of the particle displacement, the transmission coefficient T_{21}^+ in terms of particle displacements is given by:

$$T_{21,disp}^+ = \frac{\|U_{\psi_l^+}\| \text{sign}(U_{\psi_l^+})}{\|U_{\phi_u^+}\| \text{sign}(U_{\phi_u^+})} \quad (\text{A13})$$

Using (A11), (A12) and (3-30), it follows:

$$\begin{aligned} T_{21,disp}^+ &= \frac{\rho_u \alpha_u}{\rho_l \beta_l} \frac{\psi_l^+}{\phi_u^+} \frac{-1}{1} \\ &= -\frac{\rho_u \alpha_u}{\rho_l \beta_l} T_{21}^+. \end{aligned} \quad (\text{A14})$$

So, a simple multiplicative factor relates the two types of transmission coefficients. This is true for all sixteen scattering coefficients. Based on this example it can be easily seen that the general relation for the scattering coefficients is the following:

$$S_{si,disp} = \frac{\text{density}(i) \times \text{velocity}(i) \times \text{sign}(i)}{\text{density}(s) \times \text{velocity}(s) \times \text{sign}(s)} S_{si,pot} \quad (\text{A15})$$

where S_{si} is one of the sixteen elements of the scattering matrix and s and i denote scattered and incident respectively. Using equations (A2), (A3) and the sign convention of Fig. A-1, it can be seen that the only negative sign factors are the ones for the downgoing S-waves ψ_l^+ and ψ_u^+ .

Substituting (3-32) in (3-33), the scattering matrix in terms of potentials is given by:

$$\begin{pmatrix} \phi_u^- \\ \psi_u^- \\ \phi_l^+ \\ \psi_l^+ \end{pmatrix} = \mathbf{S}_{pot} \begin{pmatrix} \phi_u^+ \\ \psi_u^+ \\ \phi_l^- \\ \psi_l^- \end{pmatrix}, \quad \mathbf{S}_{pot} = \begin{pmatrix} \mathbf{R}^+ & \mathbf{T}^- \\ \mathbf{T}^+ & \mathbf{R}^- \end{pmatrix}. \quad (\text{A16})$$

Using relation (A15), the scattering matrix in terms of particle displacements is then given by:

$$\mathbf{S}_{disp} = \begin{pmatrix} 1/\rho_u \alpha_u & 0 & 0 & 0 \\ 0 & 1/\rho_u \beta_u & 0 & 0 \\ 0 & 0 & 1/\rho_l \alpha_l & 0 \\ 0 & 0 & 0 & -1/\rho_l \beta_l \end{pmatrix} \mathbf{S}_{pot} \begin{pmatrix} \rho_u \alpha_u & 0 & 0 & 0 \\ 0 & -\rho_u \beta_u & 0 & 0 \\ 0 & 0 & \rho_l \alpha_l & 0 \\ 0 & 0 & 0 & \rho_l \beta_l \end{pmatrix}. \quad (\text{A17})$$

When using the more conventional definition for the Lamé potentials, i.e. (3-11) without the $-(i\omega\rho)^{-1}$ factor, the density terms drop out of relations (A15) and (A17).

Appendix B Explicit expressions for the scattering coefficients

Making use of (A15), the explicit expressions for the scattering coefficients that are given on pp. 150-151 of Aki and Richards (1980) can be modified to yield the corresponding expressions for the Lamé potentials. Repeated use is made of the following variables:

$$\begin{aligned} a &= \rho_l(1 - 2\beta_l^2 p^2) - \rho_u(1 - 2\beta_u^2 p^2), & b &= \rho_l(1 - 2\beta_l^2 p^2) + 2\rho_u\beta_u^2 p^2 \\ c &= \rho_u(1 - 2\beta_u^2 p^2) + 2\rho_l\beta_l^2 p^2, & d &= 2(\rho_l\beta_l^2 - \rho_u\beta_u^2) \end{aligned} \quad (B1)$$

The same is true for the following terms that depend on the vertical slownesses:

$$\begin{aligned} E &= bq_{p,u} + cq_{p,l}, & F &= bq_{s,u} + cq_{s,l} \\ G &= a - dq_{p,u}q_{s,l}, & H &= a - dq_{p,l}q_{s,u} \\ D &= EF + GHp^2 \end{aligned} \quad (B2)$$

The vertical slownesses q for the homogeneous and inhomogeneous waves are defined by (3-28) and (3-29) respectively. With the above definitions, the expressions for scattering coefficients in terms of Lamé potentials are given in Table B-1. Note that all sixteen scattering coefficients become complex if one or more of the four vertical slownesses becomes imaginary.

Table B-1 Explicit expressions for the scattering coefficients in terms of Lamé potentials, based on Aki and Richards (1980). See also equations (B1), (B2) for some definitions.

| Incident wave | Scattering coefficient |
|--|--|
| Φ_u^+ downgoing P-wave upper half-space | $R_{11}^+ = [(bq_{p,u} - cq_{p,l})F - (a + dq_{p,u}q_{s,l})Hp^2]/D$ $R_{21}^+ = -2q_{p,u}(ab + cdq_{p,l}q_{s,l})p/D$ $T_{11}^+ = 2\rho_l q_{p,u} F/D$ $T_{21}^+ = -2\rho_l q_{p,u} Hp/D$ |
| Ψ_u^+ downgoing S-wave upper half-space | $R_{12}^+ = 2q_{s,u}(ab + cdq_{p,l}q_{s,l})p/D$ $R_{22}^+ = [(bq_{s,u} - cq_{s,l})E - (a + dq_{p,l}q_{s,u})Gp^2]/D$ $T_{12}^+ = 2\rho_l q_{s,u} Gp/D$ $T_{22}^+ = 2\rho_l q_{s,u} E/D$ |
| Φ_l^- upgoing P-wave lower half-space | $T_{11}^- = 2\rho_u q_{p,l} F/D$ $T_{21}^- = -2\rho_u q_{p,l} Gp/D$ $R_{11}^- = -[(bq_{p,u} - cq_{p,l})F + (a + dq_{p,l}q_{s,u})Gp^2]/D$ $R_{21}^- = -2q_{p,l}(ac + bdq_{p,u}q_{s,u})p/D$ |
| Ψ_l^- upgoing S-wave lower half-space | $T_{12}^- = 2\rho_u q_{s,l} Hp/D$ $T_{22}^- = 2\rho_u q_{s,l} E/D$ $R_{12}^- = 2q_{s,l}(ac + bdq_{p,u}q_{s,u})p/D$ $R_{22}^- = -[(bq_{s,u} - cq_{s,l})E + (a + dq_{p,u}q_{s,l})Hp^2]/D$ |

References

- Aki, K., and Richards, P. G., 1980, *Quantitative Seismology*, Freeman.
- Amundsen, L., and Ursin, B., 1988, Frequency-wavenumber inversion of acoustic data: 58th Ann. Internat. Mtg., Soc. Expl. Geophys., Expanded Abstracts, 845-848.
- Assous, F., Chalindar, B., and Collino, F., 1989, Nonlinear elastic inversion of prestack marine seismic data: *Proc. IEEE*, 77, 877-890.
- Ball, V., 1988, Thin bed tuning analysis using AVO stratigraphy methods: 58th Ann. Internat. Mtg., Soc. Expl. Geophys., Expanded Abstracts, 1213-1216.
- Ball, V. L., 1987, Depth inversion of impedance and Poisson's ratio using the Insight™ interactive modeling system: 57th Ann. Internat. Mtg., Soc. Expl. Geophys., Expanded Abstracts, 624-626.
- Balogh, D., Snyder, G., and Barney, W., 1986, Examples of a new approach to offset amplitude analysis: 56th Ann. Internat. Mtg., Soc. Expl. Geophys., Expanded Abstracts, 350-351.
- Bamberger, A., Chavent, G., Hemon, C., and Lailly, P., 1982, Inversion of normal incidence seismograms: *Geophysics*, 47, 757-770.
- Berkhout, A. J., 1982, *Seismic migration*, Elsevier.
- Berkhout, A. J., 1988, *Applied seismic wave theory*, Elsevier.
- Berkhout, A. J., and Wapenaar, C. P. A., 1990, Delphi: Delft philosophy on acoustic and elastic inversion, part 1: *The Leading Edge*, 9, no. 2, 20-33.
- Castagna, J. P., Batzle, M. L., and Eastwood, R. L., 1985, Relationships between compressional-wave and shear-wave velocities in clastic silicate rocks: *Geophysics*, 50, 571-581.
- Cerveny, V., and Ravindra, R., 1971, *Theory of seismic head waves*, University of Toronto Press.

- Chapel, F., Kolb, P., and Canadas, G., 1989, CMP nonlinear inversion in (t-p) domain: 59th Ann. Internat. Mtg., Soc. Expl. Geophys., Expanded Abstracts, 935-937.
- Cox, H. L. H., 1991, Estimation of macro velocity models by wave field extrapolation, Ph.D. thesis, Delft University of Technology.
- Crans, W., and Berkhout, A. J., 1980, Assessment of seismic amplitude anomalies: Oil and Gas Journal, no. 11, 156-168.
- de Bruin, C. G. M., Wapenaar, C. P. A., and Berkhout, A. J., 1990, Angle dependent reflectivity by means of prestack migration: Geophysics, 55, 1223-1234.
- Dobbs, S. L., Wilson, C. R., and Backus, M. M., 1990, Accounting for limited spatial aperture in the waveform inversion of p-tau seismograms: Geophysics, 55, 452-457.
- Duijndam, A. J. W., 1987, Detailed Bayesian inversion of seismic data, Ph.D thesis, Delft University of Technology.
- Duijndam, A. J. W., 1988, Bayesian estimation in seismic inversion. Part I: Principles: Geophys. Prosp., 36, 878-898.
- Duijndam, A. J. W., 1988, Bayesian estimation in seismic inversion. Part II: Uncertainty analysis: Geophys. Prosp., 36, 899-918.
- Dunkin, J. W., 1965, Computation of modal solutions in layered elastic media at high frequencies: Bull. Seis. Soc. Am., 55, 335-358.
- Fuchs, K., 1968, The reflection of spherical waves from transition zones with arbitrary depth-dependent elastic moduli and density: J. Phys. Earth, 16, Special Issue, 27-41.
- Geertsma, J., 1961, Velocity-log interpretation: The effect of rock bulk compressibility: J. Soc. Petr. Eng., 1, 235-248.
- Gilbert, F., and Backus, G., 1966, Propagator matrices in elastic wave and vibration problems: Geophysics, 31, 326-332.
- Gill, P. E., Murray, W., and Wright, M. H., 1981, Practical Optimization, Academic Press.
- Haskell, N. A., 1953, The dispersion of surface waves on multilayered media: Bull. Seis. Soc. Am., 43, 17-34.

- Helgesen, J., 1991, Prestack inversion of group-filtered seismic data: *Geophys. Prosp.*, 39, 313-336.
- Hilterman, F. J., 1983, *Seismic Lithology*, SEG Continuing Education Course, SEG, Tulsa.
- Kennett, B. L. N., 1974, Reflections, rays and reverberations: *Bull. Seis. Soc. Am.*, 64, 1685-1696.
- Kolb, P., and Canadas, G., 1986, Least-squares inversion of prstack data: Simultaneous identification of density and velocity of stratified media: 56th Ann. Internat. Mtg., Soc. Expl. Geophys., Expanded Abstracts, 604-607.
- Kolb, P., Chapel, F., and Picart, I., 1989, Lithologic inversion: A reflectivity versus angle (RVA) approach: 59th Ann. Internat. Mtg., Soc. Expl. Geophys., Expanded Abstracts, 695-699.
- Kolb, P., Collino, F., and Lailly, P., 1986, Pre-stack inversion of a 1-D medium: *Proc. IEEE*, 74, 498-508.
- Lailly, P., 1983, The seismic inverse problem as a sequence of before stack migrations, in Bednar, J. B., Redner, R., Robinson, E. A. and Weglein, A. B., Eds, *Conference on inverse scattering: theory and application*: SIAM, 206-220.
- Lörtzer, G. J. M., 1990, An integrated approach to lithological inversion, Ph.D. thesis, Delft University of Technology.
- Lörtzer, G. J. M., and Berkhout, A. J., 1990, Linear AVO inversion of multi-component seismic data: 59th Ann. Internat. Mtg., Soc. Expl. Geophys., Expanded Abstracts, 967-972.
- Lörtzer, G. J. M., and Berkhout, A. J., 1992, An integrated approach to lithological inversion-part I: Theory: *Geophysics*, 57, No.2.
- Mazzotti, A., and Mirri, S., 1991, An experience in seismic amplitude processing: *First Break*, 9, no. 2, 65-73.
- McGillivray, P. R., and Oldenburg, D. W., 1990, Methods for calculating Fréchet derivatives and sensitivities for the non-linear inverse problem: a comparative study: *Geophys. Prosp.*, 38, 499-524.
- Mora, P., 1987, Nonlinear two-dimensional elastic inversion of multioffset seismic data.: *Geophysics*, 52, 1211-1228.
- Müller, G., 1985, The reflectivity method: a tutorial: *J. Geophys.*, 58, 153-174.

- Ostrander, W. J., 1982, Plane wave reflection coefficients for gas sands at non-normal angles of incidence: 52th Ann. Internat. Mtg., Soc. Expl. Geophys., Expanded Abstracts, 216-218.
- Ostrander, W. J., 1984, Plane-wave reflection coefficients for gas sands at non-normal angles of incidence: *Geophysics*, 49, 1637-1648.
- Pan, G. S., and Phinney, R. A., 1989, Full-waveform inversion of plane-wave seismograms in stratified acoustic media: Applicability and limitations: *Geophysics*, 54, 368-380.
- Pan, G. S., Phinney, R. A., and Odom, R. I., 1988, Full-waveform inversion of plane-wave seismograms in stratified acoustic media: Theory and feasibility: *Geophysics*, 53, 21-31.
- Pan, G. S., Young, C. Y., and Castagna, J. P., 1990, Sensitivity and resolution of an integrated target-oriented prestack elastic inversion.: 60th Ann. Internat. Mtg., Soc. Expl. Geophys., Expanded Abstracts, 1173-1176.
- Phinney, R. A., Odom, R. I., and Fryer, G. J., 1987, Rapid generation of synthetic seismograms in layered media by vectorization of the algorithm: *Bull. Seis. Soc. Am.*, 77, 2218-2226.
- Pica, A., Diet, J. P., and Tarantola, A., 1990, Nonlinear inversion of seismic reflection data in a laterally invariant medium: *Geophysics*, 55, 284-292.
- Rutherford, S. R., and Williams, R. H., 1990, Amplitude-versus-offset variations in gas sands: *Geophysics*, 54, 680-688.
- Sheriff, R. E., and Geldart, L. P., 1983, *Exploration seismology*, Vol.2: Data-processing and interpretation, Cambridge University Press.
- Shuey, R. T., 1985, A simplification of the Zoeppritz equations: *Geophysics*, 50, 609-614.
- Smith, G. C., and Gidlow, P. M., 1987, Weighted stacking for rock property estimation and detection of gas: *Geophys. Prosp.*, 35, 993-1014.
- Spratt, S., 1987, Effect of normal moveout errors on amplitude versus offset-derived shear reflectivity: 57th Ann. Internat. Mtg., Soc. Expl. Geophys., Expanded Abstracts, 634-637.
- Swan, H. W., 1990, Noise Sensitivity of linear seismic inversion: 60th Ann. Internat. Mtg., Soc. Expl. Geophys., Expanded Abstracts, 1177-1180.
- Tarantola, A., 1984, Inversion of seismic reflection data in the acoustic approximation: *Geophysics*, 49, 1259-1266.

- Tarantola, A., 1984, The seismic reflection inverse problem, in Santosa, F., Pao, Y.-H., Symes, W. W. and Holland, C., Eds, *Inverse problems of acoustic and elastic waves*: SIAM, 104-181.
- Tarantola, A., Crase, E., Jervis, M., Koren, Z., Lindgren, J., Mosegaard, K., and Noble, M., 1990, Nonlinear inversion of seismograms: State of the art: 60th Ann. Internat. Mtg., Soc. Expl. Geophys., Expanded Abstracts, 1193-1198.
- Treadgold, G. E., Dey-Sarkar, S. K., Smith, S. W., and Swan, H. W., 1990, Amplitude versus offset and thin beds: 60th Ann. Internat. Mtg., Soc. Expl. Geophys., Expanded Abstracts, 1463-1466.
- Treadgold, G. E., Ritchie, K., and Dey-Sarkar, S. K., 1990, AVO: An example of processing pitfalls: 60th Ann. Internat. Mtg., Soc. Expl. Geophys., Expanded Abstracts, 1487-1490.
- Ursin, B., and Dahl, T., 1990, Least-squares estimation of reflectivity polynomials: 60th Ann. Internat. Mtg., Soc. Expl. Geophys., Expanded Abstracts, 1069-1071.
- Vail, P. J., Strauss, P. J., Levitt, P. R., Smith, G. C., and Gidlow, P. M., 1990, Extraction of P- and S-wave velocities from a 3-D reflection data set and its application to direct hydrocarbon detection: 60th Ann. Internat. Mtg., Soc. Expl. Geophys., Expanded Abstracts, 1181-1184.
- van der Knaap, W., 1959, Nonlinear behavior of elastic porous media: *Petroleum Transactions*, 216, 179-187.
- Verschuur, D. J., 1991, Surface-related multiple elimination, an inversion approach, Ph.D. thesis, Delft University of Technology.
- Wapenaar, C. P. A., and Berkhout, A. J., 1989, *Elastic wave field extrapolation*, Elsevier.
- Wapenaar, C. P. A., Herrmann, P., Verschuur, D. J., and Berkhout, A. J., 1990, Decomposition of multicomponent seismic data into primary P- and S-wave responses: *Geophys. Prosp.*, 38, 633-661.
- Young, G. B., and Braille, L. W., 1976, A computer program for the application of Zoeppritz's amplitude equations and Knott's energy equations: *Bull. Seis. Soc. Am.*, 66, 1881-1885.
- Yu, G., 1985, Offset-amplitude variation and controlled-amplitude processing: *Geophysics*, 50, 2697-2708.

- Zoeppritz, K., 1919, Erdbebenwellen VIIIB, Über Reflexion und Durchgang seismischer Wellen durch Unstetigkeitsflächen: Göttinger Nachrichten, 1, 66-84.

Summary

In exploration seismology, the subsurface response due to elastic sources at the surface is recorded, processed and interpreted in order to obtain an image of the earth's interior. The ultimate goal is to locate and evaluate hydrocarbon reservoirs. The variation of the reflection amplitude with the incident angle of the illuminating wave field contains information about the elastic properties of the subsurface layers, which can be linked to the rock and pore parameters.

In this thesis, an inversion strategy for multi-offset seismic data is discussed. Such an inversion implicitly employs the angle dependent reflectivity information in the seismic data. The inversion procedure is target oriented, i.e. only those sections of the subsurface that one is specifically interested in are inverted for.

In Chapter 1, the distinction between direct inversion and inversion by data fitting is introduced. Some current elastic inversion techniques of the data fitting type are discussed: Weighted stacking and nonlinear elastic inversion of multi-shot data sets. In contrast to the parametric and target oriented approach that is followed in this thesis, the majority of the current methods makes use of a gridded representation of the total subsurface. Pros and cons are discussed.

Chapter 2 introduces the DELPHI scheme for elastic processing and inversion. Rather than using one grand inversion scheme, the inversion is subdivided into a number of separate processes. Each of these processes is chosen optimally suited for its particular task. The next process is only started if the previous processing result is found to be acceptable. The last modules, target oriented elastic and lithologic inversion are preceded by a redatuming step. When choosing the new datums closely above and parallel to the local layering of the targetzone, the target medium can *locally* be considered a 1D model, particularly if CMP data is used. This enables one to use a 1D elastic inversion per lateral position along the target.

In Chapter 3 the theory of reflection and transmission of plane waves at a boundary between two homogeneous isotropic elastic media is discussed. The scattering is described in terms of P- and S-wave potentials for which composition and decomposition matrices are derived. At the end of the chapter, approximation formulas

for the reflection coefficients are given, which provide an insight in the behavior of the reflectivity as a function of the elastic contrasts.

Chapter 4 discusses the reflectivity method, which is used for the forward modeling of the iterative elastic inversion. The method is implemented in the horizontal slowness - frequency domain. Pure P- and S-wave sources and receivers are used.

In Chapter 5 the principles of Bayesian inversion are discussed. Assuming Gaussian noise on the data and the prior relations, it is demonstrated that the minimum of the weighted sum of the squared residuals yields a suitable estimator for the model parameters. Numerical methods for nonlinear optimization are discussed.

Chapter 6 deals with the specifics of the proposed elastic inversion method. Non-uniqueness aspects are analyzed a.o. by making use of the approximated expressions for the reflection coefficients. Furthermore, the implementation of robustness parameters for amplitude and travelttime errors is discussed. Finally, the incorporation of seismic-lithology relations is introduced as a means to optimally stabilize the inversion. This procedure enables one to obtain the lithotype and the porosity of the target layers directly.

Chapter 7 is devoted to three examples that illustrate the potential of the proposed inversion technique.

Finally, Chapter 8 gives a comprehensive overview of the inversion method and concludes with some critical remarks about p - τ inversion in general.

Samenvatting

In exploratie seismologie, wordt de responsie van de ondergrond ten gevolge van elastische bronnen aan het oppervlak opgenomen, verwerkt en geïnterpreteerd. Het uiteindelijke doel is het localiseren en evalueren van olie- en gasreservoirs. De variatie van de reflectieamplitude met de hoek van inval van het belichtende golfveld bevat informatie over de elastische eigenschappen van de ondergrond, welke gerelateerd kunnen worden aan de gesteente en porieparameters.

In dit proefschrift wordt een inversiestrategie voor multi-kanaals seismische gegevens behandeld. Een dergelijke inversie gebruikt impliciet de hoekafhankelijke informatie in de seismische gegevens. De inversieprocedure is doelgericht (*target oriented*), hetgeen betekent dat slechts voor die gedeeltes van de ondergrond waarin men specifiek geïnteresseerd is, geïnverteerd wordt.

In hoofdstuk 1 wordt het verschil tussen directe inversie en inversie d.m.v. data aanpassing geïntroduceerd. Enkele actuele inversietechnieken van het laatstgenoemde type worden behandeld: *Weighted Stacking* en nonlineaire inversie van *multi-shot data sets*. In tegenstelling tot de parametrische en doelgerichte aanpak die in dit proefschrift wordt gevolgd, maken laatstgenoemde methodes gebruik van een regelmatige bemonstering van de totale ondergrond. Voor- en nadelen worden besproken.

In hoofdstuk 2 wordt het DELPHI schema voor elastische gegevensverwerking en inversie geïntroduceerd. In plaats van één groot inversieschema te gebruiken, wordt de inversie opgedeeld in een aantal aparte processen. Elk van deze processen wordt optimaal voor de betreffende taak gekozen. Het volgende proces wordt slechts gestart wanneer het voorafgaande proces een acceptabel resultaat opgeleverd heeft. De laatste modules, elastische en lithologische inversie worden voorafgegaan door een *redatuming* stap. Wanneer de reductievlakken dicht boven, en parallel aan de lokale gelaagdheid van het doelgebied worden gekozen, kan dit laatste lokaal als eendimensionaal beschouwd worden, met name als CMP gegevens worden gebruikt. Hierdoor is het mogelijk gebruik te maken van een eendimensionale inversie per laterale positie van het doelgebied.

In hoofdstuk 3 wordt de theorie van reflectie en transmissie van vlakke golven aan een vlakke overgang van twee homogene isotrope elastische media behandeld. Deze verstrooiing wordt beschreven in termen van P- en S-golf potentialen, waarvoor compositie en decompositie matrices worden afgeleid, Benaderingen voor de reflectiecoëfficiënten worden gegeven, welke een inzicht verschaffen in het gedrag van de reflectiviteit als een functie van de elastische contrasten.

In hoofdstuk 4 wordt de *reflectivity method* behandeld, welke gebruikt wordt voor de voorwaartse modellering tijdens de iteratieve elastische inversie. De methode is geïmplementeerd in het *horizontal slowness* - frequentie domein. Pure P- en S-golfbronnen worden gebruikt.

In hoofdstuk 5 worden de principes van Bayesiaanse inversie behandeld. Onder de aanname van Gaussische ruis op de metingen en de *a priori* relaties, wordt aangetoond dat het minimum van de gewogen som van de gekwadrateerde residuen een geschikte schatter is voor de modelparameters. Numerieke methoden voor nonlineaire optimalisatie worden behandeld.

Hoofdstuk 6 behandelt de kenmerken van de voorgestelde elastische inversiemethode. *Non-uniqueness* aspecten worden onder andere geanalyseerd door gebruik te maken van benaderde uitdrukkingen voor de reflectiecoëfficiënten. Verder wordt de implementatie van robuustheidparameters voor amplitude- en looptijdfouten behandeld. Tenslotte wordt de incorporatie van seismische-lithologie relaties geïntroduceerd zodat de inversie optimaal gestabiliseerd kan worden. Door deze procedure wordt men in staat gesteld het lithotype alswel de porositeit van de lagen van het doelgebied te bepalen.

Hoofdstuk 7 is gewijd aan drie voorbeelden die het potentiaal van de voorgestelde inversiemethode illustreren.

Tenslotte geeft hoofdstuk 8 een uitgebreide samenvatting van de inversiemethode en wordt afgesloten met enige kritische kanttekeningen bij inversie in het p - τ domein.

Curriculum Vitae

Naam Johan Cornelis de Haas

Geboortedatum 18 februari 1959

Geboorteplaats Leeuwarden

Opleiding

1965-1971 Basisonderwijs te Franeker.

1971-1977 Atheneum B aan de RSG te Harlingen.

1977-1985 Technische Natuurkunde aan de Technische Hogeschool te Delft. Afgestudeerd (met lof) binnen de groep *Computational Physics* van prof.ir. B.Th. Veltman op het onderwerp "Moleculaire dynamica van het klassieke tweedimensionale elektronengas met behulp van de P3M methode".

Werk

1986-1991 Wetenschappelijk medewerker bij de groep *Seismics and Acoustics* van prof.dr.ir. A.J. Berkhout, eerst als lid van het PRINCEPS project, later als lid van het DELPHI project.

1992-heden Adviseur voor informatie technologie als oprichter/directeur van PowerHouse Consultants te Caracas, Venezuela.